

*Sister Rod Destructive Examinations (FY23)*

# ***Appendix I: SNF Aerosols Released During Rod Fracture***

## **Spent Fuel and Waste Disposition**

*Prepared for  
US Department of Energy  
Spent Fuel and Waste Science  
and Technology*

*Oak Ridge National Laboratory  
Rose Montgomery, Yadu Sasikumar,  
Tamara J. Keever, Vineet Kumar,  
Ricardo Muse*

***January 31, 2024***

**M2SF-24OR010201024**

**ORNL/SPR-2023/3171**

This report was prepared as an account of work sponsored by an agency of the United States Government. Neither the United States Government nor any agency thereof, nor any of their employees, makes any warranty, express or implied, or assumes any legal liability or responsibility for the accuracy, completeness, or usefulness of any information, apparatus, product, or process disclosed, or represents that its use would not infringe privately owned rights. Reference herein to any specific commercial product, process, or service by trade name, trademark, manufacturer, or otherwise, does not necessarily constitute or imply its endorsement, recommendation, or favoring by the United States Government or any agency thereof. The views and opinions of authors expressed herein do not necessarily state or reflect those of the United States Government or any agency thereof.

## SUMMARY

This report documents work performed under the Spent Fuel and Waste Disposition's Spent Fuel and Waste Science and Technology program for the US Department of Energy (DOE) Office of Nuclear Energy (NE). This work was performed to fulfill Level 2 Milestone M2SF-24OR010201024, "FY23 ORNL Testing on Sibling Pins," within work package SF-24OR01020102 and is an update to the work reported in M2SF-23OR010201024, M2SF-22OR010201047, M2SF-21OR010201032, M2SF-19OR010201026, and M2SF-19OR010201028.

As a part of the DOE NE High Burnup Spent Fuel Data Project, Oak Ridge National Laboratory (ORNL) is performing destructive examinations (DEs) of high burnup (HBU) (>45 GWd/MTU) spent nuclear fuel (SNF) rods from the North Anna Nuclear Power Station operated by Dominion Energy. The SNF rods, called *sister rods* or *sibling rods*, are all HBU and include four different kinds of fuel rod cladding: standard Zircaloy-4 (Zirc-4), low-tin Zirc-4, ZIRLO, and M5. The DEs are being conducted to obtain a baseline of the HBU rods' condition before dry storage and are focused on understanding overall SNF rod strength and durability. Fuel rods and defueled cladding will be tested to derive material properties. Although the data generated can be used for multiple purposes, one primary goal for obtaining the post-irradiation examination data and the associated measured mechanical properties is to support SNF dry storage licensing and relicensing activities by (1) addressing identified knowledge gaps and (2) enhancing the technical basis for post-storage transportation, handling, and subsequent disposition.

This report documents the status of the ORNL Phase 1 DE activities related to the collection of SNF aerosol particles released during fuel rod fracture in 4-point bending in Phase 1 of the sister rod test program.

Table IS-1 summarizes the status of the work.

**Table IS-1. DE status.**

Planned DE		Status	Comments
AERO	Collect aerosol particles released during selected tests	In progress	<p>(FY21) An aerosol collection system with fixturing and sampling devices was designed to characterize and quantify the respirable fraction of UO<sub>2</sub> particles released during rod fracture. The fixture is used in conjunction with 4-point bend (4PB) tests.</p> <p>The aerosol collection system is currently being revised, tested, and verified out of cell. Modified collection stages were designed and added to allow for a larger range of particle collection using the commercially available Sioutas cascade. Testing and computational fluid dynamics (CFD) simulations indicate adequate system performance. A different commercially available cascade (Marple) may provide better sampling capability for UO<sub>2</sub> and is being considered. The enclosure used may be changed to a different material to avoid any static attraction.</p> <p>One test was completed in cell with a ZIRLO-clad segment, and initial results are available. Further chemical processing is needed to more precisely define the mass of aerosols collected, but the preliminary order of magnitude result is that 4,615.85 µg of dust-type particulate was collected in the test.</p>

Planned DE		Status	Comments
			<p>(FY22) Additional analysis of the material collected in the first experiment was completed, and Section I-6.2.2 was modified to incorporate the new data. The collection efficiency of the system was evaluated and is discussed in Section I-4.3. The airborne release fractions and respirable fraction were calculated for the first test and are provided in Section I-6.3. The Marple cascade was evaluated for use with the collection apparatus, but because of the modified intake required to connect with the remainder of the system, it was decided that it would not be used: this evaluation is provided in Section I-7.1. Dual sampling is being considered to protect against loss of aerosols during SEM imaging; progress on this technique is discussed in Section I-7.2.</p> <p>(FY23) One test was performed using the MiniMight load frame. Material was collected during the test, and isotopic analyses will be completed early in FY24. Isotopic- and size-related release fractions were calculated for the results from the first test.</p>



## ACKNOWLEDGMENTS

Many thanks to our US Department of Energy Office of Nuclear Energy sponsor, Ned Larson, along with the Spent Fuel and Waste Science and Technology storage and transportation program leadership for their continued support. The sister rod project would not have been possible without the vision and support of the Electric Power Research Institute, Westinghouse, Framatome, and Dominion Energy.

This work would not have been possible without the support and expertise provided by the leadership and staff members of ORNL's Irradiated Fuel Examination Laboratory (IFEL) and Radioactive Materials Analytical Laboratory (RMAL). Special thanks go to Caleb Dryman, Benjamin Roberts, Jerid Metcalf, John Hinds, and Brian Woody for their assistance with in-cell testing activities. Many thanks to Haley Wightman, Marc Chattin, and Ben Roach for their support in processing and analyzing the specimens at RMAL. We are indebted to Radiological Control Technicians Andrew Greenwood, Scott Gentry, Mark Walls, and Lisa Duncan, and Facilities Manager Steve Vrooman for their support, oversight, and flexibility in the handling and surveillance of the aerosol specimens. Special thanks go to Maintenance Supervisor Mark Neal and his team for their support on all of our projects, and especially for getting the scanning electron microscopy (SEM) room enclosure modified quickly for this experiment. Finally, many thanks are due Mark Delph for his vital support of the deployment of new equipment to the cell, and we appreciate his continued support.

This page is intentionally left blank.

## CONTENTS

SUMMARY .....	iii
ACKNOWLEDGMENTS .....	v
CONTENTS.....	vii
LIST OF FIGURES .....	ix
LIST OF TABLES .....	xiii
REVISION HISTORY.....	xv
ACRONYMS.....	xvii
I-1 Introduction .....	1
I-2 Theory .....	3
I-3 Test setup.....	7
I-3.1 Development notes.....	7
I-3.2 SNF Aerosol Collection Test Protocol.....	10
I-3.3 Sampling card design and calibration .....	11
I-3.3.1 Commercially available Sioutas cascade impactor .....	11
I-3.3.2 Added sampler stages and collection substrate selection.....	13
I-3.3.3 Flow rate selection and evaluated nominal cascade cut points .....	14
I-3.3.4 Pump performance when battery powered.....	14
I-4 Results of SNF Tests .....	17
I-4.1 AERO-1 .....	17
I-4.1.1 General Observations.....	17
I-4.1.2 Analysis of the Collected Material.....	20
I-4.1.2.1 Initial ICP-MS Analysis (FY21) .....	20
I-4.1.2.2 Follow-On ICP-MS Analysis (FY22) .....	24
I-4.2 AERO-2 .....	26
I-5 Airborne Release Fraction and Respirable Fraction.....	29
I-5.1 AERO-1 .....	29
I-6 Cascade verification testing and sample processing testing .....	35
I-6.1 Verification using physical testing.....	35
I-6.1.1 Pressure drop tests.....	37
I-6.1.2 Verification Testing Using ISO Dust Mixtures .....	38
I-6.1.3 SEM image processing.....	39
I-6.2 Verification using computational fluid dynamics tools .....	43
I-6.2.1 Steady state simulations.....	47
I-6.2.2 Particle Deposition Simulations.....	55
I-6.2.3 Collection Enclosure Simulations.....	61
I-6.3 Collection efficiency calculations.....	62
I-6.3.1 ISO dust test evaluated stage collection efficiency.....	62
I-6.3.2 CFD evaluated stage collection efficiency.....	64
I-7 Ongoing and Future Work.....	67

---

I-7.1	Potential use of Marple cascade.....	67
I-7.2	Optional dual sampling .....	68
References.....		73

## LIST OF FIGURES

Figure I-1. Schematic showing the principle of inertial impactation as seen in a typical cascade impactor.....	3
Figure I-2. Illustration of Particle Collection Efficiency in Inertial Impactation Samplers (Adapted from Aerosol Technology, William C. Hinds [G11]).....	4
Figure I-3. Illustration of a load frame with aerosol collection enclosure and one sampling card .....	8
Figure I-4. Sampling card with multistage cascade impactor and dedicated pump (a) set up for verification testing and (b) fit up on the load frame in the hot cell. ....	9
Figure I-5. In-cell 4PB aerosol sampling setup.....	10
Figure I-6. Impactor, exploded view (adapted from Sioutas impactor brochure).....	12
Figure I-7. The orifice plates and stages of the modified Sioutas cascade impactor. ....	13
Figure I-8. Example of the change in dual-head pump output as a function of elapsed time. ....	15
Figure I-9. Post-test fractured aerosol test specimen 3D8E14-2810-2963. Note the cladding oxide spalling in the maximum bending stress location that resulted from the 4PB test. ....	17
Figure I-10. 3D8E14-2810-2963 outer surfaces following the aerosol collection 4PB test. The fracture occurred in the body of a pellet, producing coarse debris consistent with past 4PB test results seen at ORNL. ....	18
Figure I-11. SEM tabs with cascade stage markings on the background showing the aerosol collected from 3D8E14-2810-2963. Thin lines on the tabs show the collected aerosol particles from SNF. ....	19
Figure I-12. Graphical representation of chromatographic separation real-time analysis. Times are approximate because real-time shifts can result from chemical matrices. ....	21
Figure I-13. Total mass collected on the filters, 3D8E14-2810-2963.....	22
Figure I-14. $^{238}\text{U}$ distribution in the cascade stages, 3D8E14-2810-2963. ....	23
Figure I-15. Total mass of SNF material recovered from ashing the adhesive tabs used to collect aerosols in the modified Sioutas Cascade Impactor, 3D8E14-2810-2963. ....	24
Figure I-16. Additional material recovered by ashing: (A) total $^{238}\text{U}$ from each stage, (B) total $^{239}\text{Pu}$ , 3D8E14-2810-2963. ....	25
Figure I-17. Pre-test appearance of 3A1F05-2402-2555, showing (a) the 360° waterside surface of the rod, (b) and (c) the exposed pellet surfaces at the ends of the test segment, and (d) a general view of the rod prior to testing.....	26
Figure I-18. Image captured during the test showing the trajectory of the segment just after fracture. The test segment fractured at the upper left loading point and part of the specimen was ejected from the enclosure. The enclosure lid was forced upward but resettled after the initial impact. ....	27
Figure I-19. AERO-2 Segment 3A1F05-2204-2555, post-test. ....	28
Figure I-20. AERO-1, histogram of total measured mass of isotope / predicted total mass of isotope in a 6 in. test segment. ....	29
Figure I-21. $^{140}\text{Ce}$ distribution in the cascade stages.....	30

Figure I-22. $^{139}\text{La}$ distribution in the cascade stages.....	30
Figure I-23. $^{146}\text{Nd}$ particle distribution in the cascade stages. ....	30
Figure I-24. $^{137}\text{Cs}$ particle distribution in the cascade stages.....	31
Figure I-25. Actinide particle distribution in the cascade stages. ....	31
Figure I-26. Epsilon particle distribution in the cascade stages, presented along with $^{91}\text{Zr}$ for comparison. ....	31
Figure I-27. AERO-1, individual isotope respirable fraction plotted with concentration of the isotope available in the source pellets. ....	34
Figure I-28. Experimental setup for dust-collection validation tests with the modified cascade and a prototype of the small enclosure.....	36
Figure I-29. Experimental test setup of the 7-stage modified Sioutas cascade impactor with flowmeter and the pressure transducer. ....	37
Figure I-30. Silver filters imaged after validation experiments with ISO dust. ....	38
Figure I-31. Silver filters imaged after weighing. The filter MB material deposit was lost during the weighing process. ....	38
Figure I-32. A black carbon tab used to collect ISO particle samples. In the hot cell, a beige-colored tab will be used to allow for visual identification of $\text{UO}_2$ deposits. ....	38
Figure I-33. The out-of-order placement of MA below MB and MC produced no deposits on MA, as expected, because the larger particles were already removed in the stages above it (quartz filters). ....	39
Figure I-34. Typical ISO dust deposit on the orifice plate's surface. ....	39
Figure I-35. SEM image of MA filter with ISO dust and the particle count outcome from the MATLAB script showing overestimation of particles caused by poor thresholding. ....	41
Figure I-36. High magnification SEM image of MA filter with ISO dust and the particle count outcome from the MATLAB script showing separate particles being identified in a large particle with minor contrast variations within the region. ....	41
Figure I-37. High magnification SEM image of MC filter with ISO dust and the binary image generated by the MATLAB script showing small particles with low pixel intensity variations merged into one large blob. ....	42
Figure I-38. (a) SEM image of PC filter with ISO dust, (b) binary image output of (a) from the MATLAB script without preprocessing, and (c) trainable Weka segmented image after binarization showing a very effective approach for identifying and isolating particles. ....	42
Figure I-39. (a) Isometric view of the Cascade impactor showing the 4 purchased stages, including inlet and outlet plates; (b) a cross sectional view of the impactor with the solid domain shown in red and the fluid domain shown in gray.....	44
Figure I-40. Microscope measurement of Test 1 Stage PD orifice width taken at various locations. The average Stage PD orifice width is $0.265 \pm 0.015$ mm.....	45
Figure I-41. (a) Slice through the computational grid on the symmetry ( $x = 0$ ) plane; (b) close-up of the finely meshed orifice region for the 4 stages.....	46

Figure I-42. (a) Contours of velocity magnitude (9 LPM) on $x = 0$ plane and $x = -8$ mm plane, (b) velocity magnitude contour ( $y=0$ ) at a midplane on the orifice stage PA, (c) Velocity magnitude contour ( $y=0$ ) at a midplane on the orifice stage PB. ....	48
Figure I-43. Streamline plot of the flow distribution through the 4-stage cascade impactor colored according to velocity magnitude (9 LPM).....	49
Figure I-44. Pressure contours (9 LPM) on (a) $x = 0$ plane and (b) $x = -8$ mm plane. ....	49
Figure I-45. Slice through the computational grid on the symmetry ( $x = 0$ ) plane for the 7-stage cascade impactor model. ....	50
Figure I-46. Contours of velocity magnitude (7 LPM) for the 7-stage cascade impactor on (a) $x = 0$ plane and (b) $x = -8$ mm plane.....	51
Figure I-47. Orifice velocity magnitude contour ( $y=0$ ) at the midplane (half of the orifices are shown) for the 7-stage cascade impactor at 7 LPM.....	52
Figure I-48. Streamline plot of the flow distribution through the 7-stage cascade impactor, colored according to velocity magnitude (7 LPM).....	52
Figure I-49. Pressure contours (7 LPM) for the 7-stage cascade impactor on (a) $x = 0$ plane and (b) $x = -8$ mm plane.....	53
Figure I-50. Isometric view of the 7-stage cascade impactor with the (inlet) injection surface and collector surfaces highlighted.....	56
Figure I-51. Physical particle size distribution histogram in the flow domain using the log normal distribution for the injector with size range $\mathcal{E}$ [0.1, 10] $\mu\text{m}$ and mean of 3 $\mu\text{m}$ .....	57
Figure I-52. Isometric view of the 7-stage cascade impactor showing the particle distribution colored according to physical particle diameter $\sim 2.5$ s after injection (7 LPM). ....	58
Figure I-53. Particles collected on the 7 stages at $\sim 2.5$ s after injection of $5.4\text{e}5$ particles (7 LPM). ....	58
Figure I-54. (a) Physical particle size distribution histogram of particles collected (7 LPM) in (a) stage MA and (b) stage PD.....	59
Figure I-55. Preliminary results from collection enclosure simulation indicating that there is no expected loss of particles through enclosure openings.....	61
Figure I-56. CFD model of collection enclosure. ....	61
Figure I-57. Collection efficiency curves for the seven stages obtained by ISO dust experiments. The red line gives the 50% efficiency for each stage. ....	63
Figure I-58. CFD-predicted collection efficiency curves for the seven stages. ....	65
Figure I-59. Comparison of stage cut points (AED) obtained by CFD and the analytical correlation. ....	66
Figure I-60. Disassembled Marple impactor with respective cut-off values for each stage. ....	67
Figure I-61. CFD simulation of a Marple cascade with an inlet cap producing an asymmetric flow distribution in the top 3 stages.....	67
Figure I-62. Combined collection set up (a), and schematic of the combined collection setup (b).....	68
Figure I-63. Individual flow rate measurements for the dual sampling setup: (A) pump exit, and (B) enclosure exit. ....	69

Figure I-64. Details of the computational flow domain: (A) complete domain, including the stagnation pressure inlets (pink-colored surfaces), the box sticky surfaces, and the two outlets; and (B) part injector from where the particles are released at time  $t = 3$  seconds. .... 70

Figure I-65. Particle size (Physical) distribution which is injected into the domain from  $t = 3$  s to  $t = 5$  s. .... 71

Figure I-66. Particle size (physical) distribution which is injected into the domain from  $t = 3$  s to  $t = 5$  s. .... 72

Figure I-67. Particle size (physical) distribution which does not pass through the samplers and is stuck in the box and the pipe walls from  $t = 3$  s to  $t = 10$  s. .... 72



## LIST OF TABLES

Table IS-1. DE status. ....	iii
Table I-1. Manufacturer-specified parameters of the Sioutas cascade impactor at 9 LPM. ....	11
Table I-2. Measured dimensions of the Sioutas cascade impactor orifices using an optical microscope and subsequent new cut-point values calculated using Eq. (I-6). ....	12
Table I-3. Post-machined dimensions of the Test 1 custom cascade stages and subsequent cut-point values. ....	13
Table I-4. Modified impactor nominal AED and physical UO <sub>2</sub> cut-points evaluated at the selected 7 LPM flow rate. ....	14
Table I-5. Measured pump flow rates for the Parker Dual Head pump (rated at 9.5 LPM). ....	15
Table I-6. Dose rates from the ghost wipe smears of the impactor stages, 3D8E14-2810-2963. ....	19
Table I-7. Eluent profile for separation of Nd, Pu from isobaric interferences. ....	21
Table I-8. Collected aerosolized isotopic mass by digestion using ICP-MS, 3D8E14-2810-2963. ....	22
Table I-9. Total collected isotopic mass by ashing and digestion, 3D8E14-2810-2963. ....	25
Table I-10. Test 2, Orifice measurements and evaluated cut points for the cascade impactor used. ....	27
Table I-11. AERO-1, measured respirable fractions by AED. ....	33
Table I-12. AERO-1, measured respirable fractions by isotope. ....	33
Table I-13. Composition and particle size distribution of ultrafine ISO test dust. ....	36
Table I-14. Experimentally measured pressure drop values for the modified Sioutas cascade impactor at 6 and 7 LPM. ....	37
Table I-15. Percentage of ISO dust particles collected across various size groups for the 7 stages at 7 LPM, counted with the MATLAB script without preprocessing. ....	40
Table I-16. Percentage of ISO dust particles collected across various size groups of ISO dust powders for the 7 stages at 7 LPM, as counted using the MATLAB script after preprocessing the SEM images. ....	43
Table I-17. Measurements for the Test 1 four purchased stages using a microscope (CFD) compared to the manufacturer's specifications. ....	45
Table I-18. Mesh settings for the trimmer and surface remesher models. ....	46
Table I-19. Initial conditions for the steady-state 4-stage cascade impactor simulation. ....	47
Table I-20. Comparison of model predictions and manufacturer's specifications for the 4-stage cascade impactor at 9 LPM. ....	50
Table I-21. Geometric parameters modeled in the 7-stage cascade impactor. ....	50
Table I-22. Comparison of modeled vs. experimental pressure drop values and model flow parameters for the 7-stage cascade impactor for 7 LPM. ....	54
Table I-23. Comparison of model vs. experimental pressure drop values and model flow parameters for the 7-stage cascade impactor for 6 LPM. ....	54

Table I-24. Part injector parameters..... 56

Table I-25. Percentages of particles collected across various size groups for the 7 stages (7 LPM)..... 60

Table I-26. Particle collection statistics for the 7-stages (7 LPM)..... 60

Table I-27 ISO dust AED cut-points – experimental vs. analytical, Eq. (I-6). ..... 62

Table I-28. List of specimens tested in 4PB where aerosols are planned to be collected. .... 67

Table I-29. Respective flow rate values of cascades 1 and 2 under combined collection setup. .... 69

**REVISION HISTORY**

<b>Date</b>	<b>Changes</b>
10/29/2021	This is a new appendix reporting the details of SNF aerosol collection during fuel rod fracture in 4-point bending.
3/31/2022	The date and document ID were updated to reflect its M2 status.
10/28/2022	The results of FY22 work were added in the following sections: I-4.3, I-6.2.2, I-6.3, I-7.1, and I-7.2.
1/13/2023	Comments received from the team were incorporated throughout and the document ID number was revised to reflect its M2 status and the issue date was changed.
10/31/2023	While the content is largely unchanged, the organization of the appendix was revised to provide a better flow of information. Section I-4.2 was added to include the results from test AERO-2; further evaluation of the isotopic analysis of test AERO-1 was added in Section I-4.1. Minor clarifications were made throughout the text.
1/31/2024	Comments received from the team were incorporated throughout and the document ID number was revised to reflect its M2 status and the issue date was changed

This page is intentionally left blank.

## ACRONYMS

4PB	4-point bend
AED	aerodynamic equivalent diameter
AERO	aerosol collection capability
ASME	American Society of Mechanical Engineers
BC	boundary condition
CFD	computational fluid dynamics
CIRFT	cyclic integrated reversible-bending fatigue tester
DE	destructive examination
DOE	US Department of Energy
EDX	energy-dispersive x-ray
FHT	full-length fuel rod heat treatment
HBU	high burnup
HPC	high-performance computing
ICP-MS	Inductively coupled plasma mass spectrometry
IFEL	Irradiated Fuel Examination Laboratory
ISO	International Organization of Standardization
LPM	liters per minute
LT	low tin
NCBI	National Center for Biotechnology Information
NE	Office of Nuclear Energy
NEFCD	Nuclear Energy and Fuel Cycle Division
NQA-1	Nuclear Quality Assurance - 1
ORNL	Oak Ridge National Laboratory
PTFE	polytetrafluoroethylene
RANS	Reynolds-averaged Navier-Stokes
RMAL	Radioactive Materials Analytical Laboratory
RT	room temperature
SEM	scanning electron microscopy
SNF	spent nuclear fuel
SST	shear stress transport

This page is intentionally left blank.

## I-1 Introduction

As a part of the DOE NE High Burnup Spent Fuel Data Project [I-1], Oak Ridge National Laboratory (ORNL) is performing destructive examinations (DEs) of high burnup (HBU) (>45 GWd/MTU) spent nuclear fuel (SNF) rods from the North Anna Nuclear Power Station operated by Dominion Energy. The SNF rods, called *sister rods* or *sibling rods*, are all HBU and include four different kinds of fuel rod cladding: standard Zircaloy-4 (Zirc-4), low-tin (LT) Zirc-4, ZIRLO, and M5. The Phase 1 DEs [I-2, I-3] are being conducted to obtain a baseline of the HBU rod's condition before dry storage and are focused on understanding overall SNF rod strength and durability. Fuel rods and defueled cladding will be tested to derive material properties. Although the data generated can be used for multiple purposes, one primary goal for obtaining the post-irradiation examination data and the associated measured mechanical properties is to support SNF dry storage licensing and relicensing activities by (1) addressing identified knowledge gaps and (2) enhancing the technical basis for post-storage transportation, handling, and subsequent disposition.

To investigate the release of aerosolized radioactive material from a HBU fuel rod during fracture (10  $\mu\text{m}$  or less is generally considered to be the upper limit of human respirability [I-4]), an aerosol collection capability (AERO) is being developed for deployment on the cyclic integrated reversible-bending fatigue tester (CIRFT) equipment (DE.05) and Instron load frame, which is used for DE.07, DE.08, and DE.10. Two different collection configurations are being developed—one for CIRFT and one for the load frame—but the aerosol collection media and approach are expected to be the same.

This appendix details the work completed to develop a suitable aerosol collection method for the radioactive materials being examined and provides the results for the tests completed.

This page is intentionally left blank.



## I-2 Theory

*Inertial impaction* is the method selected to collect aerosol particulates released from the sister rod specimen as it is fractured during testing. Impactors are devices that separate the particulates based on size. In an impaction sampler, gas containing the particulates to be sampled is accelerated through an orifice towards a collection filter placed at a fixed distance below an orifice. The collection filter forces the air stream to change direction abruptly, and particles having enough inertia to escape the air stream are collected on the filter. Smaller particles follow the air stream and remain suspended in the gas flow, moving on to the next stage of the impactor (Figure I-1).

The *cut point* of an impaction sampler is the size of particles collected by the sampler with 50% efficiency. Ideally, all particles greater than a certain size are collected on the filter, and all smaller particles pass through. However, because impactors act on aerodynamic variables and do not perform like a mechanical barrier such as a sieve, the collection efficiency is not 100%. Based on the Stokes number (a function of the orifice diameter and flow rate used), the collection efficiency increases for particles larger than the cut point and decreases for smaller particles, as illustrated in Figure I-2. The particle diameter distribution is generally characterized by a log-normal distribution. For a 4  $\mu\text{m}$  cut point, 100% of 10  $\mu\text{m}$  particles and 50% of 4  $\mu\text{m}$  particles are collected from the air stream and deposited on the filter.

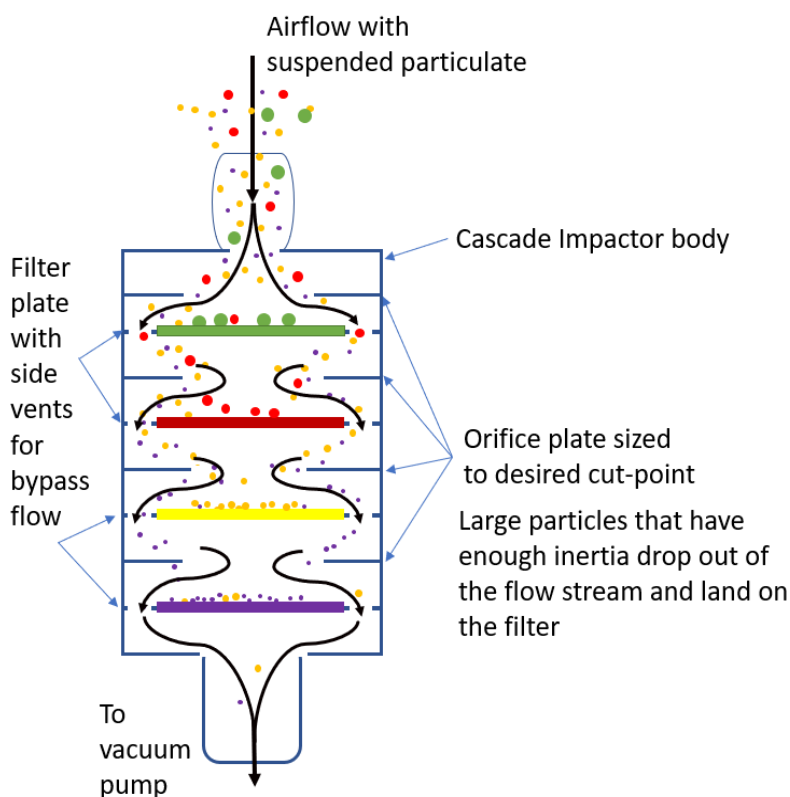


**Figure I-1. Schematic showing the principle of inertial impaction as seen in a typical cascade impactor.**

Cut points are typically evaluated empirically using monodisperse powders. The experimental method comprises rigorous sampling techniques involving multiple steps to analyze particulates and compare them with particles at a particular impactor stage, as in the case of cascade impaction cut-point

calculations [I-9]. The efficiency curves are sensitive to the dust-generating conditions, as shown by Moore et al. [I-10], so these must be carried out with great caution to avoid errors.

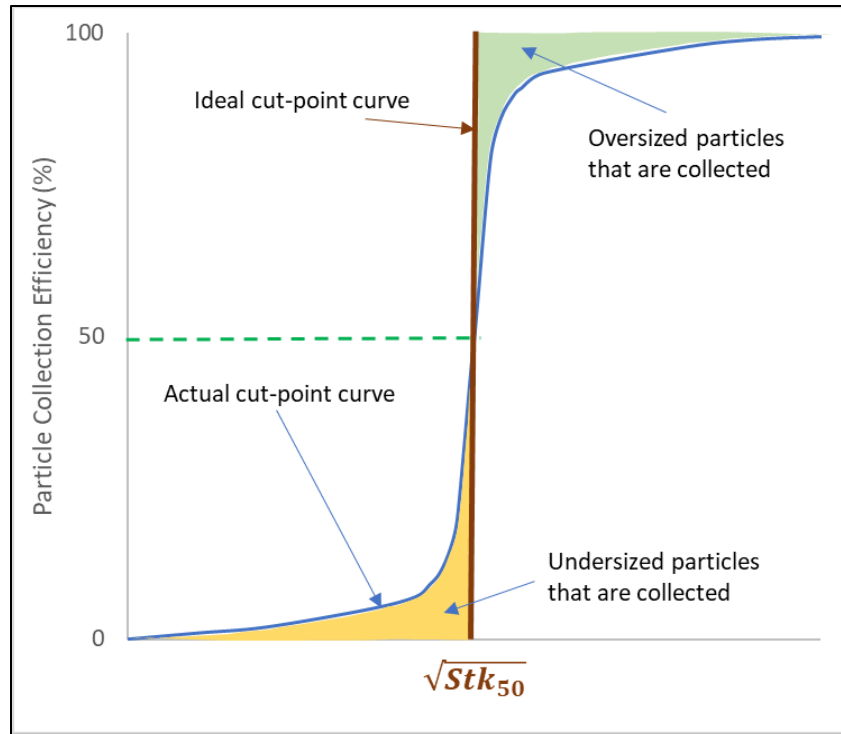


**Figure I-2. Illustration of Particle Collection Efficiency in Inertial Impaction Samplers**  
(Adapted from *Aerosol Technology*, William C. Hinds [G11])

Aerosols consist of two phases: solid/liquid particles and the gas in which they are suspended. The aerosol particles share the temperature, pressure, viscosity, and mean free path of the medium in which they are suspended, and the properties that affect the medium also indirectly affect the aerosol particle motion, an effect which is often Brownian (random) [I-11]. The Reynolds number is an important parameter (ratio of inertial force to frictional force) used to determine whether the flow of an aerosol is laminar or turbulent (i.e., in the Stokes region,  $Re < 1$ , or in Newton's region,  $Re > 1,000$ ). The region between, in which  $1 < Re < 1,000$ , is called the *transitional region*. Stokes' law is used for particles in the Stokes region. The law considers particle motion in a fluid in which the inertial forces are negligible compared with viscous forces. This is largely applied to aerosols, as most aerosol motion occurs at low Reynolds numbers (laminar regime) because of the low velocities and small particle sizes involved under settling. The law states that the total resisting force on a spherical particle moving with a velocity  $V$  through a fluid is equal to the integration of the normal and tangential forces acting over the surface of the particle:

$$F_D = F_n + F_t = \pi\eta Vd + 2\pi\eta Vd = 3\pi\eta Vd, \quad (I-1)$$

where:

- $F_D$  is the total resisting force acting on the particle,
- $F_n$  is the normal force acting on the particle,
- $F_t$  is the tangential force acting on the particle,

$\eta$  is the viscosity of the fluid, and  
 $d$  is the diameter of the particle.

A particle suspended in a medium (for example, air) which eventually settles has a terminal settling velocity where the drag force of the air around the aerosol particle is exactly equal and opposite to the force acting on the system (e.g., gravity or centrifugal force). Settling velocity is independent of density of gas and increases rapidly with particle size. In the real world, aerosol particles are composed of different geometries, most often irregular. Therefore, certain correction factors are applied when considering irregular aerosol particle motion, because the shape of the particle affects the drag force and settling velocity. A constant dynamic shape factor ( $\chi$ ) is used to account for the shape effects by multiplying the ratio of the actual resistance force of the non-spherical particle to an equivalent resistance force as experienced on a spherical particle of the same velocity and volume:

$$\chi = \frac{F_D}{3\pi\eta V d_e}. \quad (\text{I-2})$$

The settling velocity of such a spherical particle in terms of  $d_e$  for a particle in still air undergoing gravitational settling is given as

$$V_{TS} = \frac{\rho_p d_e^2 g}{18\eta\chi}. \quad (\text{I-3})$$

where  $d_e$  is the equivalent diameter of a sphere having the same volume as that of the irregular particle.

Aerodynamic diameter ( $d_a$ ) is an equivalent diameter of a water droplet (spherical particle with  $1\text{g/cm}^3$  density) that has the same settling velocity as the non-spherical particle:

$$V_{TS} = \frac{\rho_w d_a^2 g}{18\eta}. \quad (\text{I-4})$$

The relationship between the aerodynamic diameter and the equivalent diameter is obtained by comparing the settling velocities obtained for the same particle:

$$d_a = d_e \left( \frac{\rho_p}{\rho_o \chi} \right)^{1/2}. \quad (\text{I-5})$$

For a perfect sphere, the dynamic shape factor ( $\chi$ ) = 1, and the aerodynamic equivalent diameter (AED) is equal to the geometric diameter multiplied by the square root of the relative density of the particle. The dynamic shape factor ( $\chi$ ) is often assumed to be equal to 1 for ease of calculations.

Under inertial impaction, the cut point can be calculated at different flow rates for a rectangular jet impactor with jet width  $W$  and length  $L$ :

$$d_{50} \sqrt{C_c} = \sqrt{\frac{9\eta W^2 L (Stk_{50})}{\rho_p Q}}. \quad (\text{I-6})$$

where  $d_{50}$  is the particle's AED at 50% collection efficiency,  $Stk_{50}$  is the Stokes number for 50% collection efficiency for impactors,  $Q$  is the jet flow rate,  $W$  and  $L$  are the width and length of the impactor orifice,  $\rho_p$  is the density of water ( $1\text{ g/cc}$ ), and  $C_c$  is Cunningham's slip correction factor. Eq. (I-

6) is derived from the Stokes number definition of the ratio of the particle's stopping distance at an average nozzle exit velocity (U) to the impactor opening half width [I-12]:

$$Stk = \frac{\tau U}{W/2} = \frac{\rho_p d_{50}^2 U C_c}{9\eta W}, \quad (I-7)$$

Eq. (I-6) can also be written in terms of jet velocity:

$$d_{50} \sqrt{C_c} = \sqrt{\frac{9\eta W (Stk_{50})}{\rho_p U}}. \quad (I-8)$$

## I-3 Test setup

The basic test setup for remote fracture of a sister rod segment in four-point bending with aerosol collection includes the load frame with its four-point bend fixture that is used to fracture the specimen, and enclosure that limits broad dispersion of the particulate released during fracture, and the cascade impactor with its pump to collect respirable aerosols, as shown in Figure I-3 and Figure I-4. The test protocol is discussed in Section I-3.2; considerations addressed within the test design are discussed in Sections I-3.1, I-3.2, and I-3.3; and modifications to the commercially available cascade impactor are discussed in Sections I-3.3.1 and I-3.3.2.

### I-3.1 Development notes

The initial AERO design was configured for the Instron load frame. The initial conceptual collection enclosure was a relatively large aluminum box that provided for a large amount of vertical travel for the load frame and fixturing, with the sampling devices mounted on the interior of the box. Several experiments using surrogate materials were completed in FY20; in FY21, the enclosure was downsized to a more compact box with the sampling media mounted externally. The smaller enclosure that is used in the tests is 3D printed plastic that can be rinsed, dissolved, or imaged. An anti-static coating was added to the enclosure interior surfaces after test 1 with the goals of reducing any static capture of aerosol-sized particulate on the enclosure walls and facilitating removal of dust-type particulate from the enclosure for analysis without introducing significant contaminants to the ICP-MS analysis. Additionally, a transparent plastic window was added to the enclosure after test 1 to allow visual examination during testing. Illustrations of the collection enclosure are shown in Figure I-3 and Figure I-4. Sampling tubing is fixed in the bottom of the enclosure to allow direct access to the location where the material is expected to be expelled from the specimen during 4-point bend (4PB) testing. Each impactor has its own dedicated vacuum pump to maintain the appropriate sampling flow rate.

The initial AERO design included two versions of the aerosol collection cards. The first version had a 4-filter Sioutas cascade impactor [I-5] with particle collection cut points of 2.5, 1.0, 0.50, and 0.25  $\mu\text{m}$ , and the second had a cyclone with a 4  $\mu\text{m}$  cut point. Out-of-cell performance testing of the cyclone indicated that it was not well-suited for this application and its use was discontinued. The cascade impactor type of collection device worked well. In FY21, work focused on expanding the Sioutas cascade impactor to include higher cut point stages to encompass the range of respirable particles and one test was completed with an SNF segment. The Sioutas impactor includes a collection platform fitted with a substrate that can be removed for examination of collected material. Experiments were performed using silver substrates because silver can be accommodated in the chemical processing. However, the collected particles were easily dislodged from the silver substrate. To avoid loss of collected material, scanning electron microscopy (SEM) conductive tabs were used in the first test as the collection substrate. Testing indicated that the use of the conductive tabs does not change the collection cut point or capacity; however, chemical processing of the material deposited on the conductive tabs has proven difficult.

Evaluations supporting the cascade collection efficiency, stage size collection range, and collection substrate testing are provide in Section I-6.

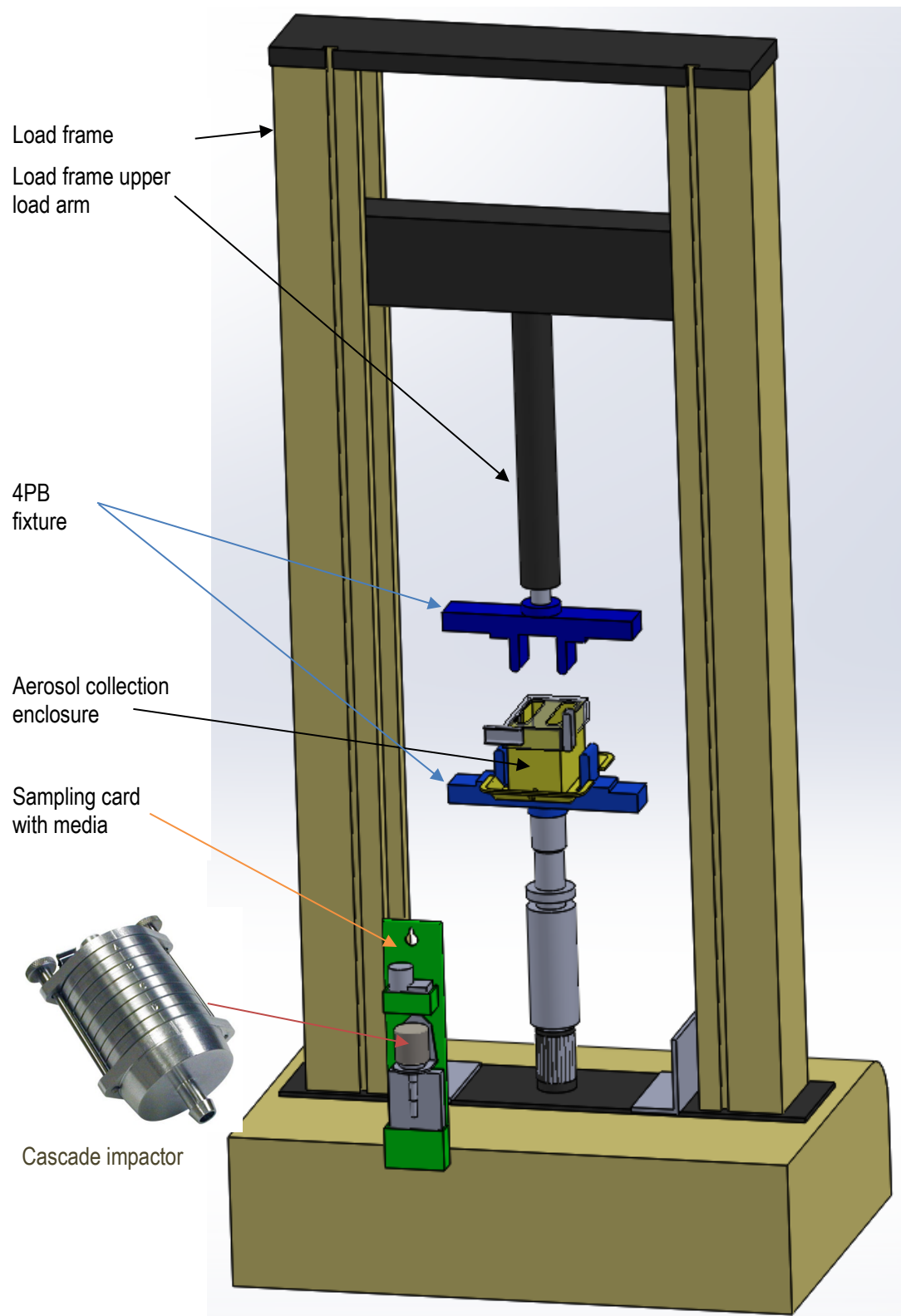


**Figure I-3. Illustration of a load frame with aerosol collection enclosure and one sampling card .**

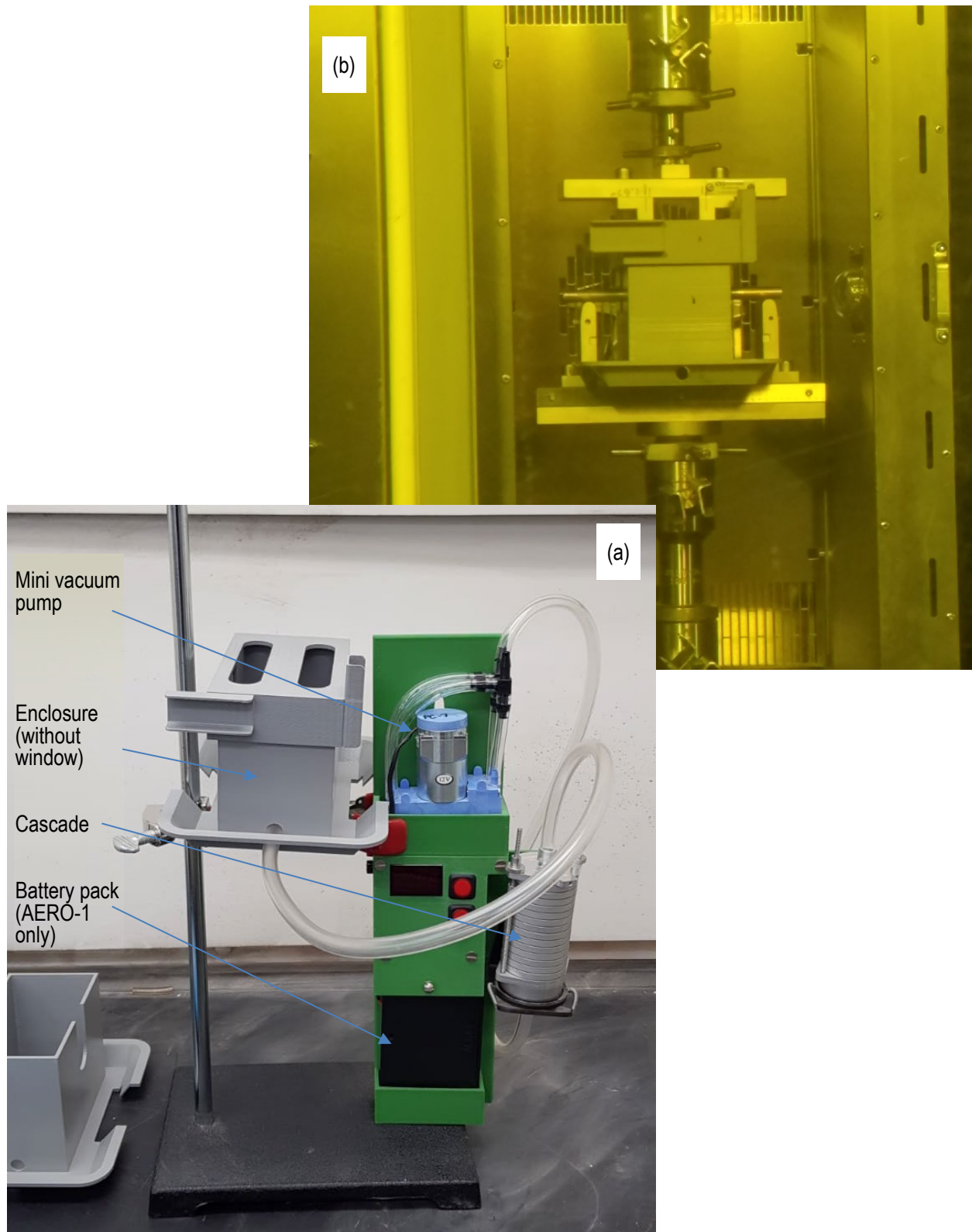


**Figure I-4. Sampling card with multistage cascade impactor and dedicated pump (a) set up for verification testing and (b) fit up on the load frame in the hot cell.**



### I-3.2 SNF Aerosol Collection Test Protocol

To collect a sample, the sampling card with connected enclosure is loaded into the hot cell as a unit. The cascade is preassembled with pre-weighed substrates mounted on each collection stage. The enclosure is mounted on the Instron 4PB fixture, with the rod segment placed on the lower fixture as for a normal 4PB test, and the enclosure lid placed onto the enclosure base, as shown in Figure I-5.

The sampler is energized by pushing the on/off switch just before performing the 4PB test. Test 1 used a battery pack to power the pump, and the test had to be completed within 15 minutes of energizing the pump to avoid lower-than-specified pump flow rates. The pump was run for 10 minutes following specimen fracture. To avoid this issue, the battery power source was replaced with DC power in later tests.

The upper fixture is disengaged from the enclosure, and the lid is removed. The specimens are weighed pre- and post-test to obtain a gross material loss measurement. Any large debris in the collection enclosure is collected and weighed. All inner surfaces of the enclosure are wiped, and the media are sent

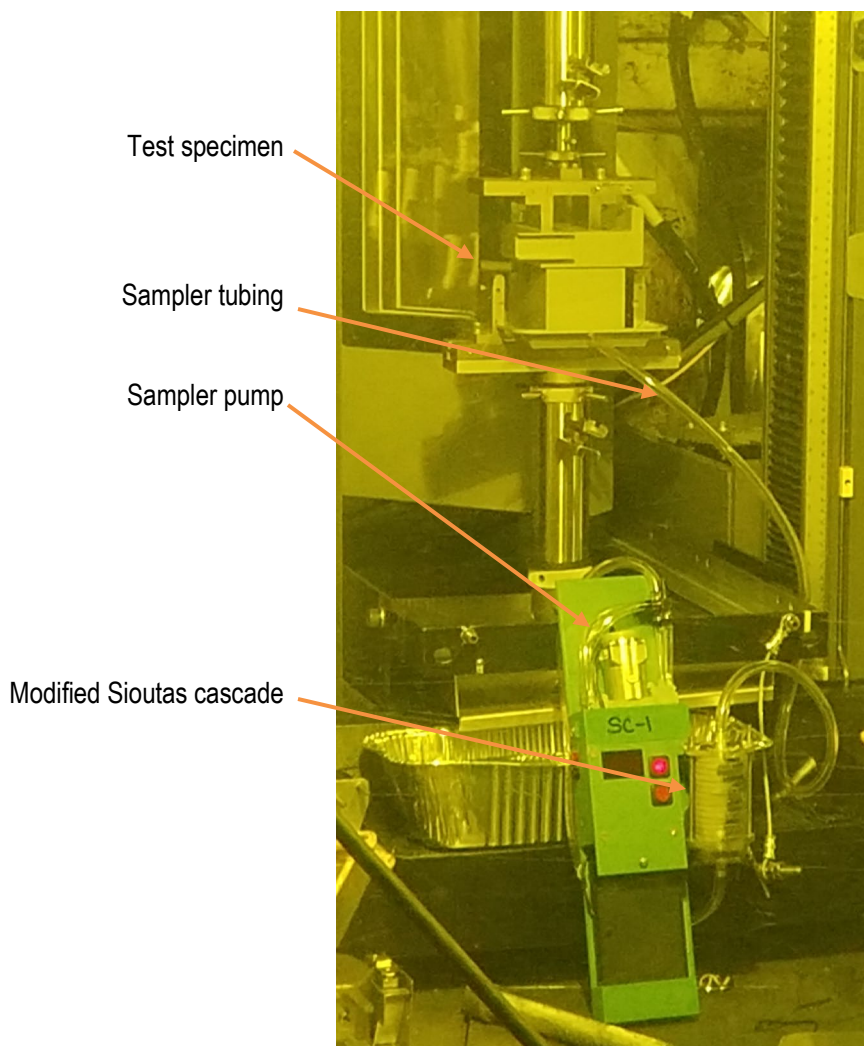


Figure I-5. In-cell 4PB aerosol sampling setup.



for chemical analysis and uranium mass measurements. Likewise, the tubing is rinsed with nitric acid, and the resulting liquid is sent for chemical analysis and uranium mass measurements. The tubing integral to the miniature pump is not included, as it is not feasible to remove the tubing through in-cell manipulation. The sampling card is considered disposable, so a new one is provided for each test.

The cascade is moved to a glovebox and disassembled. Each collection substrate is extracted from the cascade and weighed. Each orifice plate is wiped down, and the material is sent for chemical processing. Smears are taken from the glovebox gloves as a potential source for contamination tracking.

Ideally, each collection substrate is then imaged using the IFEL SEM; however, there are concerns that some collected aerosols could be lost during vacuum pumping in the SEM. To date, no specimens have been imaged in the SEM, but a dual-sampling approach is being developed to allow at least one collected specimen to be imaged (see Section I-7.2). After imaging, each collection substrate is immersed in nitric acid and transferred for chemical analysis and uranium mass measurements.

### I-3.3 Sampling card design and calibration

For the purposes of collecting used nuclear fuel respirable aerosols expelled during a four-point bending fracture, a commercially available Sioutas impactor was modified and integrated to the sampling system as described in the following subsections.

#### I-3.3.1 Commercially available Sioutas cascade impactor

Initial investigations were focused on implementation of a Sioutas cascade impactor sold by SKC Inc. (Sioutas Cascade Impactor Catalog number 225-370) as modified by ORNL. The purchased impactor is constructed from anodized aluminum, has four collection stages with cut points specified at a flow rate of 9 liters per minute (LPM) as 2.5, 1.0, 0.50, and 0.25  $\mu\text{m}$  AED (as defined using polydisperse ammonium sulfate aerosols, density  $\sim 1.77 \text{ gm/cm}^3$ ). This information is summarized in Table I-1, and the equivalent cut point diameters for  $\text{UO}_2$  at 9 LPM are also listed. The commercially available Sioutas cascade impactor is shown in Figure I-6.

**Table I-1. Manufacturer-specified parameters of the Sioutas cascade impactor at 9 LPM.**

Stage	Cascade impactor manufacturer cut-point rating (AED) in $\mu\text{m}$	Equivalent $\text{UO}_2$ geometric diameter* ( $\mu\text{m}$ )	Orifice width (cm)	Orifice length (cm)	Jet velocity (cm/s)
A	2.5	0.75	0.090	1.9	877.2
B	1.0	0.30	0.050	2.1	1,428.6
C	0.5	0.15	0.036	1.9	2,631.6
D	0.25	0.08	0.014	2.5	4,286.0

\* AED = geometric diameter  $\times$  (density)<sup>1/2</sup>

To verify performance of the cascade impactor before using it for tests with SNF, several tests were performed using dusts composed of known materials and diameters. The as-received cascade orifices were measured using a Leica S9i microscope, and the average was taken from five readings. Table I-2 lists the measured orifice dimensions of the purchased stages with the recalculated cut points.

**Table I-2. Measured dimensions of the Sioutas cascade impactor orifices using an optical microscope and subsequent new cut-point values calculated using Eq. (I-6).**

Stage	As-received cut point ( $\mu\text{m}$ )	Equivalent $\text{UO}_2$ geometric diameter ( $\mu\text{m}$ )	As-received orifice width $\pm 0.0015$ (cm)	As-received orifice length $\pm 0.0015$ (cm)	Average jet velocity at 9 LPM (cm/s)
PA	3.631	1.097	0.102	2.007	731.0
PB	1.815	0.548	0.051	2.007	1465.0
PC	1.419	0.429	0.039	2.024	1866.0
PD	0.948	0.286	0.026	2.029	2789.0

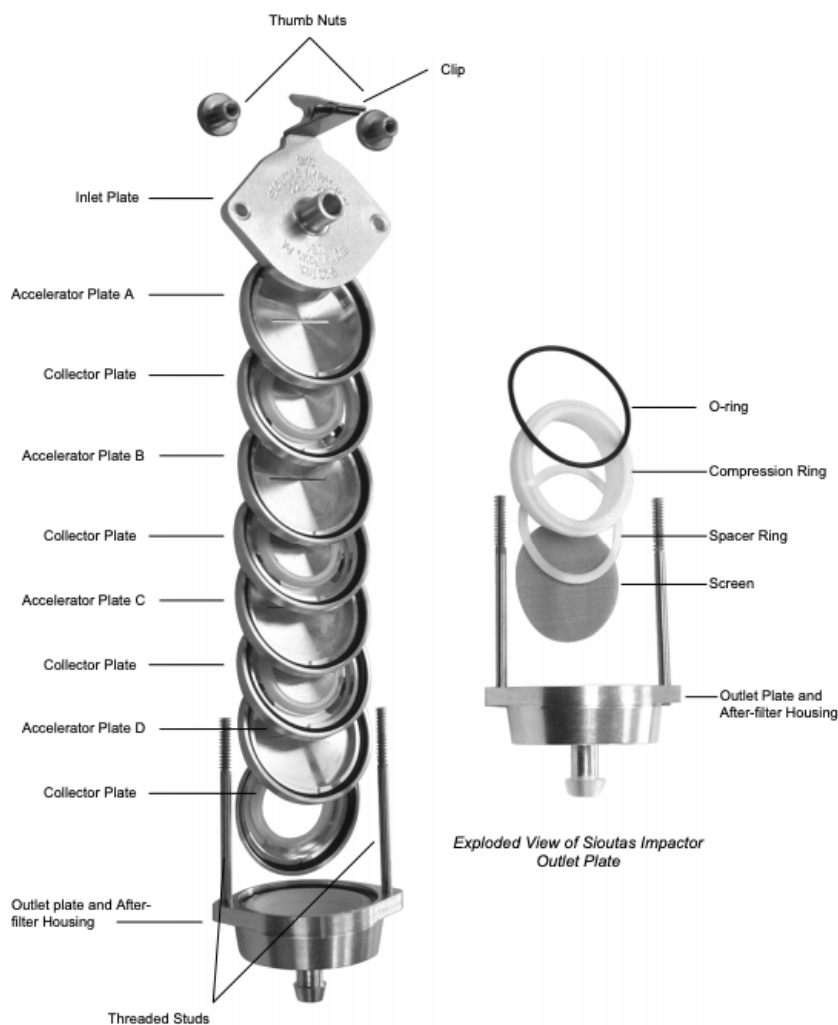


**Figure I-6. Impactor, exploded view (adapted from Sioutas impactor brochure).**

The National Center for Biotechnology Information (NCBI) gives the respirable aerosol limit as 10  $\mu\text{m}$  AED. This is equal to a 3.02  $\mu\text{m}$  (geometric) spherical particle of  $\text{UO}_2$ .

The objective of this experimental work is to capture particles up to 10  $\mu\text{m}$  AED to determine the respirable fraction. However, the off-the-shelf impactor does not provide a wide enough range of AED.

According to Eq. (I-6), the impactor cut point can be adjusted by varying pump speeds or the cascade orifice dimensions. Both measures were adopted, and three additional stages were designed and added to the stack.

### I-3.3.2 Added sampler stages and collection substrate selection

To widen the cut point capacity of the cascade, three stages were added. The first stage is envisioned as a prefilter to collect the larger airborne particles that make it into the cascade. The orifice dimensions needed to achieve the desired cut points (15, 10, and 8  $\mu\text{m}$ ) at 7 LPM were specified by holding the length constant and optimizing the orifice width as calculated using Eq. (I-6). The manufactured stages are measured using a Leica S9i microscope, and the results are averaged from five readings. Table I-3 lists the as-built dimensions of the machined stages used for Test 1 as an example, along with the calculated cut-point values at 7 LPM.

**Table I-3. Post-machined dimensions of the Test 1 custom cascade stages and subsequent cut-point values.**

Stage	As-built cut point diameters ( $\mu\text{m}$ )	Equivalent UO <sub>2</sub> geometric diameter ( $\mu\text{m}$ )	As-received orifice width $\pm 0.0015$ (cm)	As-received orifice length $\pm 0.0015$ (cm)	Average Jet velocity (cm/s)
MA	15.64	4.72	0.387	1.952	158.0
MB	11.53	3.48	0.288	1.919	218.0
MC	7.70	2.32	0.192	1.938	329.0

The final cascade configuration shown in Figure I-7 includes three machined stages, MA, MB, and MC, and four purchased stages, PA, PB, PC, and PD, stacked on extended lead screws in the cascade holder. The manufacturer recommends using a 25 mm polytetrafluoroethylene (PTFE) filter with 0.5  $\mu\text{m}$  perforations; unfortunately, this material would disintegrate in the high radioactive environment anticipated in this experiment. Silver filters and carbon tabs were investigated as alternatives that would be amenable to SEM imaging and chemical digestion. However, the silver filters were rejected because



**Figure I-7. The orifice plates and stages of the modified Sioutas cascade impactor.**

the collected aerosol material can be easily dislodged, and it is anticipated that the cascades will be bumped around quite a bit in the hot cell. The carbon tabs are preferred because they can be used for SEM imaging, and they have a sticky surface that will prevent adsorbed particles from reentering the air flow in the cascade. A silver-based SEM substrate with a tacky surface was eventually selected, as it provides good contrast to the dark gray  $\text{UO}_2$  material to be collected.

### I-3.3.3 Flow rate selection and evaluated nominal cascade cut points

A flow rate of 7 LPM was chosen to achieve the desired cut-point distribution using the additional stages with the purchased stages. Table I-4 lists the nominal cut-point values for the modified cascade impactor at a flow rate of 7 LPM as established in Section I-6.2. We expect to verify the cut points with scanning electron microscope examination of the particle sizes deposited on each stage for at least one test using a dual sampling process as described in Section I-7.2.

**Table I-4. Modified impactor nominal AED and physical  $\text{UO}_2$  cut-points evaluated at the selected 7 LPM flow rate.**

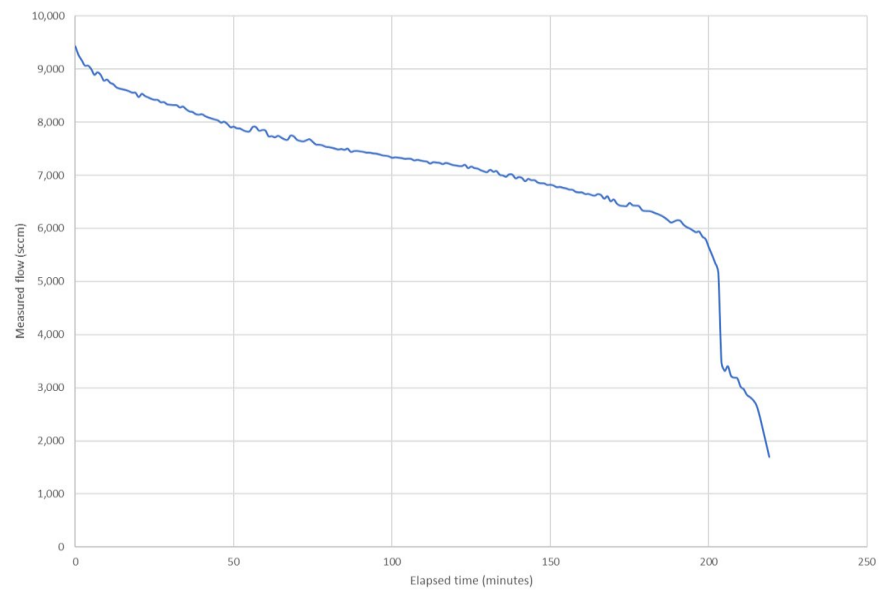
Parameter	Stage MA	Stage MB	Stage MC	Stage PA	Stage PB	Stage PC	Stage PD
Physical mean ( $\mu\text{m}$ )	4.2	2.3	1.8	1.4	0.8	0.5	0.4
Physical median ( $\mu\text{m}$ )	3.7	2.0	1.8	1.3	0.8	0.5	0.4
Physical STD ( $\mu\text{m}$ )	2.2	0.8	0.3	0.2	0.1	0.1	0.1
AED mean ( $\mu\text{m}$ )	14.0	7.5	5.9	4.5	2.7	1.7	1.2
AED median ( $\mu\text{m}$ )	12.1	6.7	5.9	4.4	2.7	1.7	1.2
AED STD ( $\mu\text{m}$ )	7.1	2.8	1.0	0.7	0.5	0.2	0.1

### I-3.3.4 Pump performance when battery powered

Prior to use, the flow rate capacity of the miniature pumps used with the sampler were tested by ORNL Metrology. For test 1, the pumps were powered by a battery pack, and all other tests used a DC power supply. Because the batteries were not expected to provide constant voltage to the pumps, it was important to understand the flow rate as a function of elapsed time. The pumps are only needed to operate for about 15 minutes during aerosol collection. The drop-off in flow rate over time when powered by battery was measured and is plotted in Figure I-8. In all cases, the measured pump flow rate with fresh batteries was higher than the design-rated flow for the sampler, as listed in Table I-5. An in-line potentiometer was used to control the voltage and to dial in the desired flow rate for the test.

**Table I-5. Measured pump flow rates for the Parker Dual Head pump (rated at 9.5 LPM).**

Pump ID	Measured flow rate with fresh batteries (sccm)
PC-1	9,903
PC-2	9,948
PC-3	10,100
PC-4	9,986
PC-5	10,102
PC-6	10,122
PC-7	9,782
PC-8	9,944
PC-9	9,824
Average	9,997
Standard deviation	139

**Figure I-8. Example of the change in dual-head pump output as a function of elapsed time.**

This page is intentionally left blank.

## I-4 Results of SNF Tests

### I-4.1 AERO-1

In February 2021, a test of a ZIRLO-clad specimen, 3D8E14-2810-2963, was completed using the modified Sioutas cascade (7 stages). The specimen had an estimated local burnup of 63 GWd/MTU and an average waterside cladding oxide thickness of 41  $\mu\text{m}$ . The test was conducted using the protocol described in Section I-5. Figure I-9 and Figure I-10 provide post-test images of the broken rod segment.

#### I-4.1.1 General Observations

Figure I-11 shows the beige SEM tab substrates that were isolated and mounted on SEM stubs. Unfortunately, SEM characterization was not performed on this set of samples, and the samples were loaded out for inductively coupled plasma mass spectrometry (ICP-MS). The collected SNF samples are shown as faint gray lines across the beige-colored SEM tabs, which is similar to those seen in the collections under the validation runs (Figure I-31). The SEM tabs were tapped before mounting to release any material that was not adhered. The measured mass of these specimens (material collected only) ranges from 0 to 0.006 g.

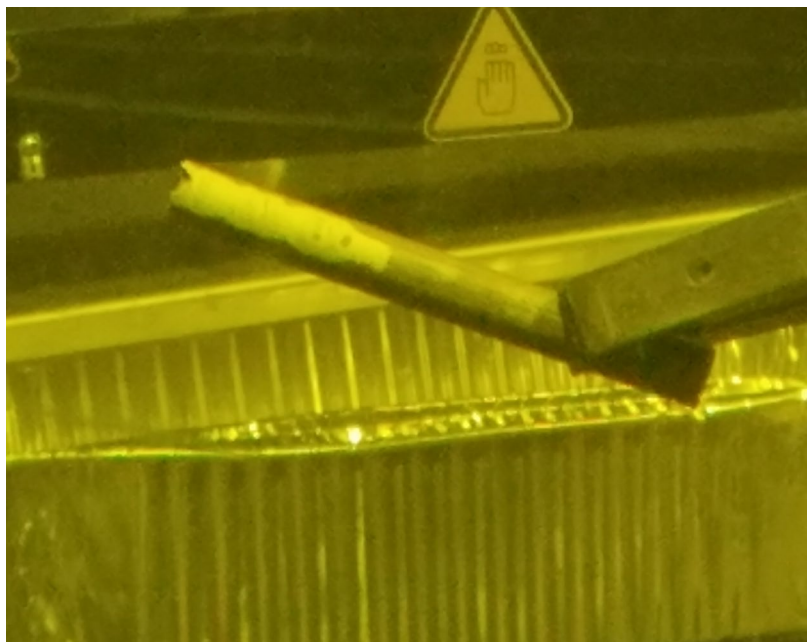


**Figure I-9. Post-test fractured aerosol test specimen 3D8E14-2810-2963. Note the cladding oxide spalling in the maximum bending stress location that resulted from the 4PB test.**





**Figure I-10. 3D8E14-2810-2963 outer surfaces following the aerosol collection 4PB test. The fracture occurred in the body of a pellet, producing coarse debris consistent with past 4PB test results seen at ORNL.**



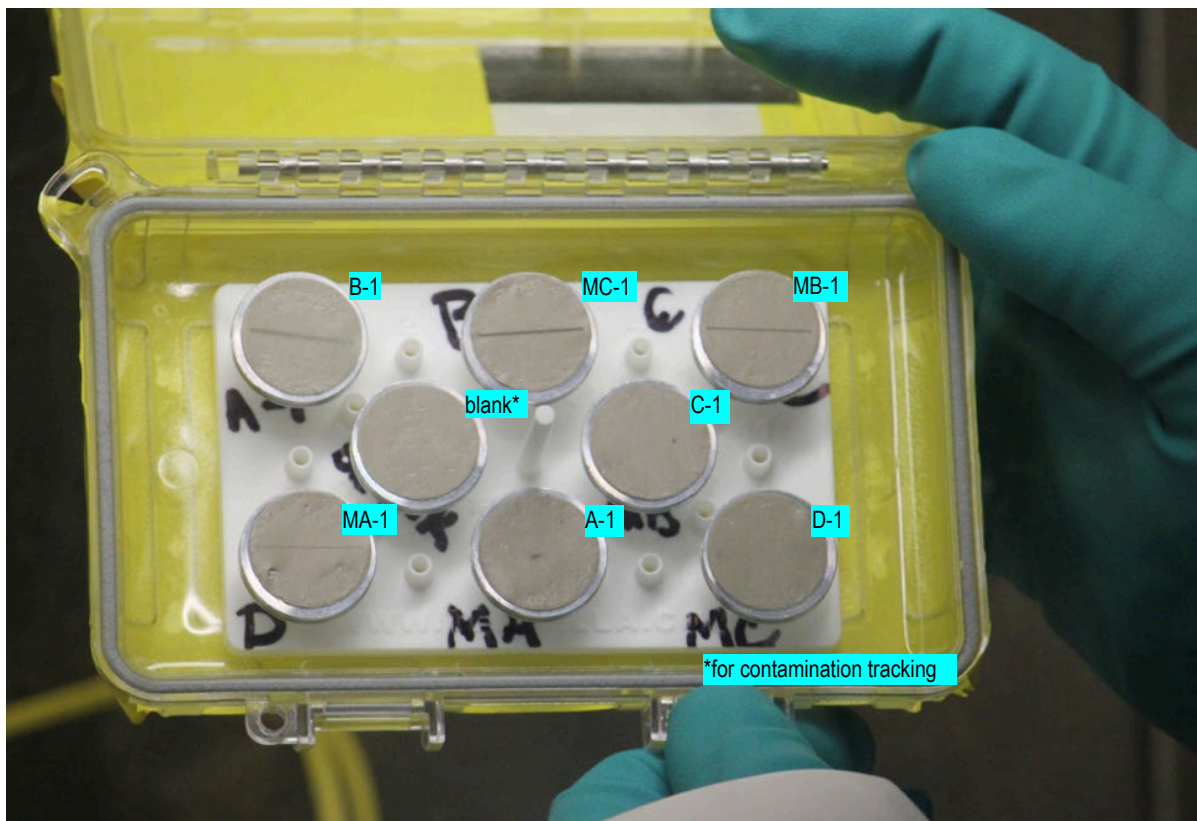


**Figure I-11. SEM tabs with cascade stage markings on the background showing the aerosol collected from 3D8E14-2810-2963. Thin lines on the tabs show the collected aerosol particles from SNF.**

A radiological survey (summarized in Table I-6) was conducted during the loadout after the experiment. This provided the first quantitative estimate of the collection in the cascades.

**Table I-6. Dose rates from the ghost wipe smears of the impactor stages, 3D8E14-2810-2963.**

Collection stage	Dose rate on contact (mrad/h)	Static counts from the silver tabs taken through the glove box gloves	
		Alpha counts from plastic retaining ring (dpm/100 cm <sup>2</sup> )	Beta/gamma counts from plastic retaining ring (dpm/100 cm <sup>2</sup> )
MA-1	630	77,520	2,200,000
MB-1	45	38,760	2,200,000
MC-1	45	77,520	-
PA-1	5	19,379	-
PB-1	72	7,752	-
PC-1	5	9,303	-
PD-1	9	466	-

Contrary to the visible collection of particles shown in Figure I-11, the information listed in Table I-6 shows that stage MA-1 had the highest alpha dose rate. This is also consistent with the dose rates obtained from the ghost wipe smears of the impactor stages.

Unfortunately, after the test was completed, it was found that the IFEL SEM facility enclosure had gaps that needed to be closed before an aerosol-type material was brought into the room, so SEM imaging of these test specimens was not possible. The specimens were sent directly to chemical processing.

### **I-4.1.2 Analysis of the Collected Material**

ICP-MS was used to characterize the material collected from the enclosure, tubing, and cascade stages. The analysis resulted in the detection of 29 isotopes, including isotopes of actinides U, Pu, Np, Th, Am and Cm; lanthanides La, Ce, Pr, Nd, Sm, Eu and Gd; epsilon phases Mo, Ru and Rh; and other important SNF elements such as Y, Sr, Cs, Ba and Zr. Blanks allowed counting for contaminants in the experiment, and they have been reported in the data.

#### ***I-4.1.2.1 Initial ICP-MS Analysis (FY21)***

Samples were received at the Radioactive Materials Analytical Laboratory in the form of SEM silver-substrate sticky tabs and ghost wipes containing aerosol and residual fuel particles. These samples were digested using 4N-8N nitric acid solutions (Optima Grade®, Fisher) in pre-cleaned or Savillex™ PFA bottles with closures and 50 mL Falcon™ tubes, respectively. The SEM tabs were also rinsed with metal-grade isopropyl alcohol to facilitate the release of adhesive and to allow access to the surface for material digestion. The SEM tab solutions were heated to 90°C with their lids on to accelerate the digestion. Once the digestion process was complete, the tabs were removed from the solution, and all solutions were analyzed by ICP-MS. The SEM tabs were monitored post-digestion for residual activity, which was detected. The tabs were then staged for ashing by muffle-furnace techniques.

The analyses of uranium, transuranic isotopes, and select fission products were performed using ICP-MS (Thermo Scientific™ iCAP™ RQ). The instrument utilizes Qtegra™ Intelligent Scientific Data Solution™ software. The mass spectrometer is positioned inside a stand-alone fume hood for radiological control and employs a standard sample introduction system using an autosampler and single-pass Peltier-cooled cyclonic spray chamber. Analyte response was made against linear regression external calibration standards from High Purity Standards (Charleston, SC) or Inorganic Ventures (Christiansburg, VA). Plutonium standard curves were made using CRM137 (New Brunswick Laboratory). Isotopes for analysis were chosen based on isobaric interferences from both natural and fission product abundances.

Neodymium and plutonium isotopic analysis for atom% determinations were made using HP-IC-ICPMS (high-pressure ion chromatography ICP-MS) using Thermo Scientific™ iCAP™ Q coupled with Dionex™ CS5000 gradient pump and off-the-shelf chromatographic separation columns. A mixed-gradient elution profile using diglycolic acid (100 mM), oxalic acid (150 mM), and deionized water to make up the gradient concentrations was used to separate isobaric interferences from the target Nd and Pu isotopes.

Table I-7 provides a summary of the separations process used, and Figure I-12 provides a diagram of the process.

**Table I-7. Eluent profile for separation of Nd, Pu from isobaric interferences.**

Segment type	Segment duration (s)	Segment end time (s)	Deionized water (%)	2 M hydrochloric acid (%)	0.1 M diglycolic acid (%)	0.15 M oxalic acid (%)
Start	0	0	100	0	0	0
Ramp	300	300	40	0	0	60
Hold	240	540	40	0	0	60
Ramp	0	540	20	0	0	80
Ramp	540	1,080	51	0	26	23
Ramp	120	1,200	0	0	100	0
Hold	300	1,500	0	0	100	0
Ramp	0	1,500	0	100	0	0
Hold	120	1,620	0	100	0	0
Ramp	120	1,740	100	0	0	0
Hold	60	1,800	100	0	0	0

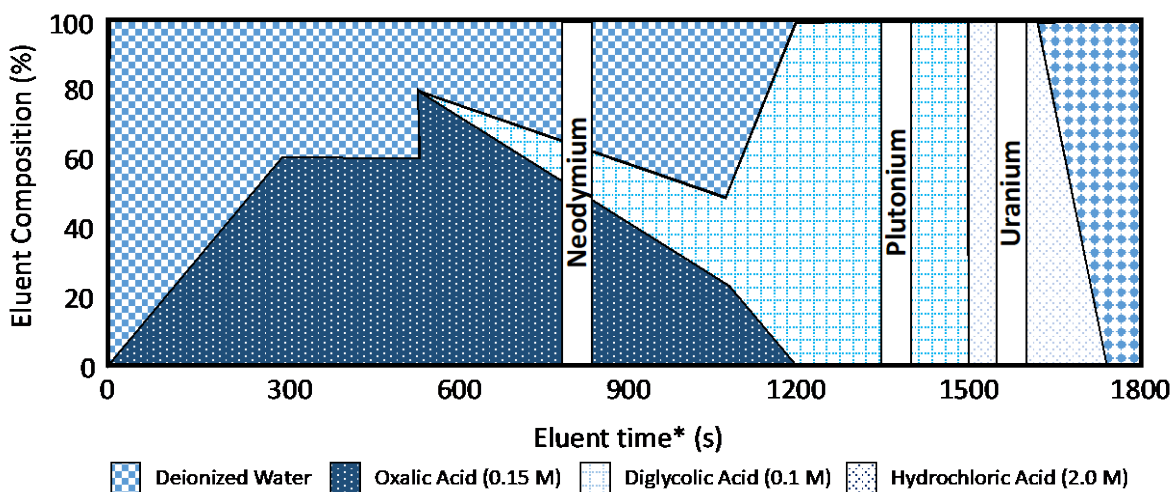
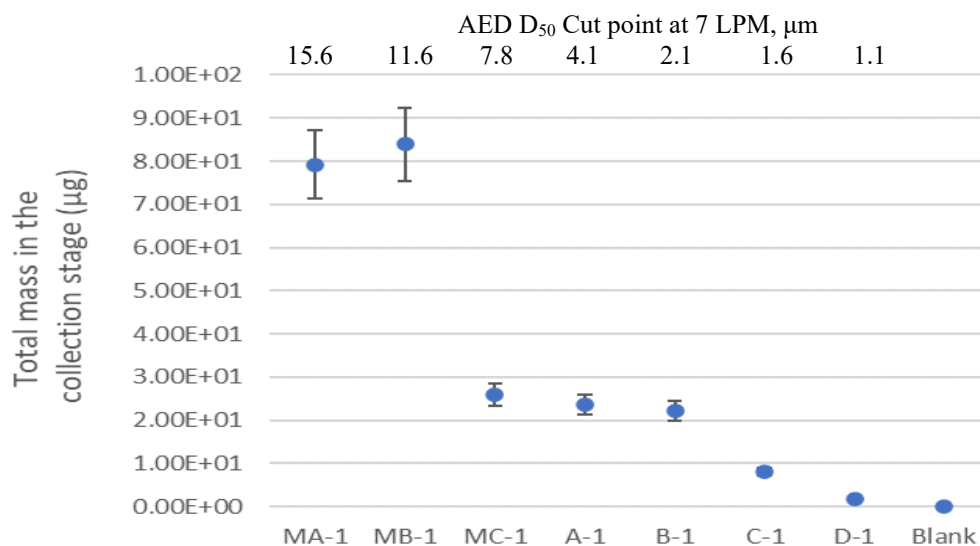
**Figure I-12. Graphical representation of chromatographic separation real-time analysis. Times are approximate because real-time shifts can result from chemical matrices.**

Table I-8 summarizes the total mass recorded for the dust collected from each surface in the flow path. The coarse SNF debris collected after the test was 0.5 g, which is the same as the recorded loss from the specimen post-test, within the capabilities of the scale used at  $\pm 0.1$  g. The total mass of SNF collected from the experiment is 4,615.85  $\mu\text{g}$ . Within the errors of the mass measurement technique, it was observed that the collection box yielded the maximum mass of dust-sized particulate, which was 15 times more than that collected in the cascade impactor. The lid also held a significant amount of SNF dust particulate, and the lowest mass of dust particulate was obtained from the tubing that connected the collection box and the cascade.

**Table I-8. Collected aerosolized isotopic mass by digestion using ICP-MS, 3D8E14-2810-2963.**

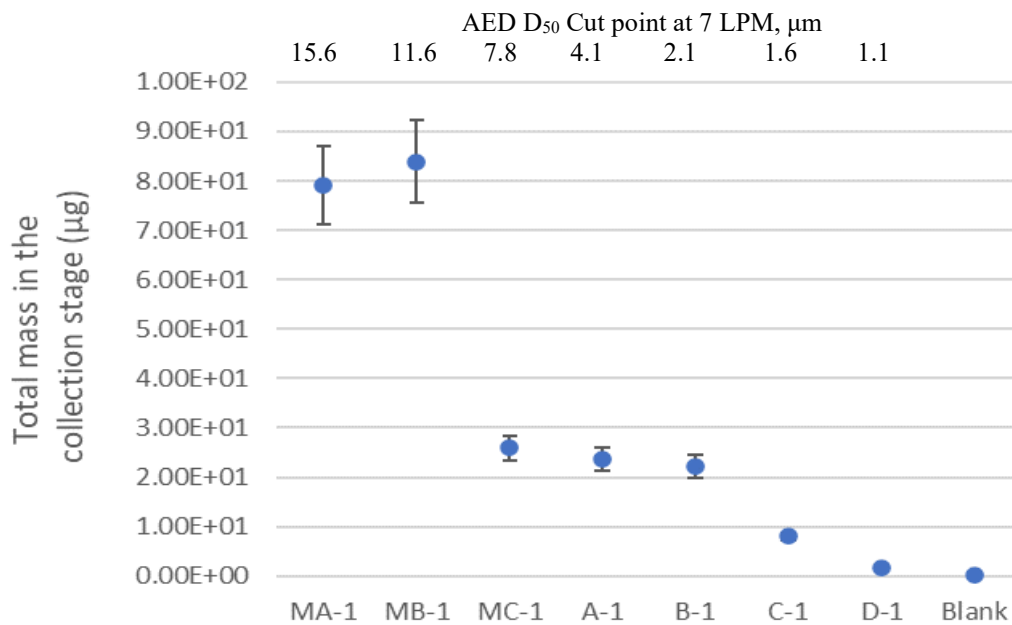
Stage	Total isotopic mass, $\mu\text{g}$	Uncertainty, $\mu\text{g}$ .	Relative error (%)
MA-1	84.53	7.92	9.4
MB-1	93.43	8.40	9.0
MC-1	28.02	2.59	9.2
A-1	26.57	2.36	8.9
B-1	24.31	2.22	9.1
C-1	9.10	0.80	8.8
D-1	2.12	0.17	8.3
Lid	85.54	6.60	7.7
Base	3988.74	332.58	8.3
Tubing	47.19	3.31	7.0
MA-1 orifice plate	150.9	14.4	9.5
MB-1 orifice plate	46.2	4.4	9.5
MC-1 orifice plate	17.8	1.7	9.6
A-1 orifice plate	4.8	0.4	8.3
B-1 orifice plate	3.4	0.3	8.8
C-1 orifice plate	1.8	0.1	5.6
D-1 orifice plate	1.4	0.1	7.1
Total mass collected as dust-type particulate	4615.85	388.35	8.4

Figure I-13 gives the total mass of particles collected in each stage of the impactor. MA-1 and MB-1 collected the largest mass of particles, ranging between 80 and 100  $\mu\text{g}$ . MC-1, A-1 and B-1 collected similar amounts, ranging between 20–35  $\mu\text{g}$ . C-1 and D-1 collected the least amount of aerosols at under 20  $\mu\text{g}$ . The impactor was designed to collect aerosols based on particle sizes, and in the absence of an SEM characterization, the trends in the total mass of particles collected can give an estimate of the total volume of SNF particles collected in each stage.

**Figure I-13. Total mass collected on the filters, 3D8E14-2810-2963.**

Previous experiments involving aerosol production and characterization using SIMFUEL have shown preferential particle size formations based on composition and multiphase particle formations [I-21]. Although characterizing these features would require an SEM/EDX analysis, the trends in individual isotopic data have been used to discuss the implications of such characteristics in real SNF. These hypotheses will be validated in future experiments involving a thorough SEM characterization of the collected particles. Figure I-14 provides the distribution of  $^{238}\text{U}$  in each of the stages, and it trends well with the total mass collected (Figure I-13). MA-1 and MB-1 have the highest collection compared to the other stages. However, the graph is not consistent with the visual information presented in Figure I-11; this discrepancy may be a result of a limited number of large SNF particles that contribute to the total mass compared to the thicker distribution of smaller particles observed in the subsequent stages.

Figure I-21, Figure I-22, and Figure I-23 show the distribution of lanthanides  $^{140}\text{Ce}$ ,  $^{139}\text{La}$ , and  $^{146}\text{Nd}$ . Lanthanides are generally observed to form solid solutions with the actinide oxides, as can be observed from the distribution of  $^{146}\text{Nd}$ , which follows that of  $^{238}\text{U}$ . However,  $^{139}\text{La}$  and  $^{140}\text{Ce}$  seem to have no similarity in distribution or resemblance to that of uranium, which suggests that their region of origin differs from that of Nd.



**Figure I-14.  $^{238}\text{U}$  distribution in the cascade stages, 3D8E14-2810-2963.**

Figure I-24 shows the distribution of  $^{137}\text{Cs}$  in the cascade. The release trend resembles that of  $^{238}\text{U}$ , with MA-1 and MB-1 having the highest release, followed by MC-1, A-1, B-1, C-1, and D-1. The graph is consistent with the high beta/gamma values recorded in Table I-6. Cesium is highly volatile and is found mainly in grain boundaries and gaps of the fuel pellet. Figure I-25 compares the distribution trends of actinides in each of the impactor stages. It is observed that they follow the same distribution and hence can be understood as agglomerations or solid solutions of actinide oxides being released from the fracture. SEM characterization is required to ascertain the exact release pattern. Figure I-26 shows the distribution trends in epsilon particles collected in each stage. The distribution of  $^{91}\text{Zr}$  is also provided as an indication of noble metal content from the cladding [I-22]. A similar trend can be seen in the lower AED stages, suggesting some smaller particles have attached themselves to larger particles.

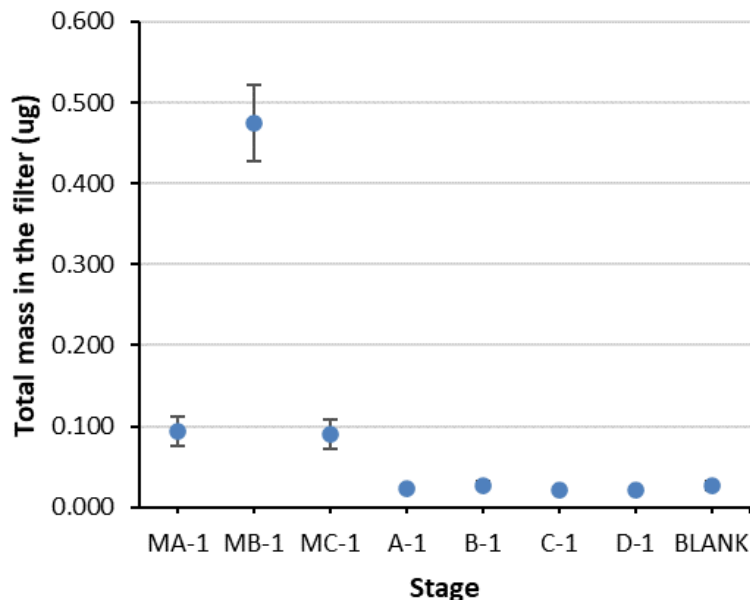
During chemical processing, the SEM tabs swelled and captured some particulate in the matrix. To fully characterize the mass of isotopes deposited, it may be necessary to ash the SEM tabs; the masses reported here may be inaccurate. Further analysis is in progress to digest these substrates. Future experiments will also involve SEM / energy-dispersive x-ray (EDX) characterization to gain a better understanding of particle size distribution and the nature of particles collected.

#### **I-4.1.2.2 Follow-On ICP-MS Analysis (FY22)**

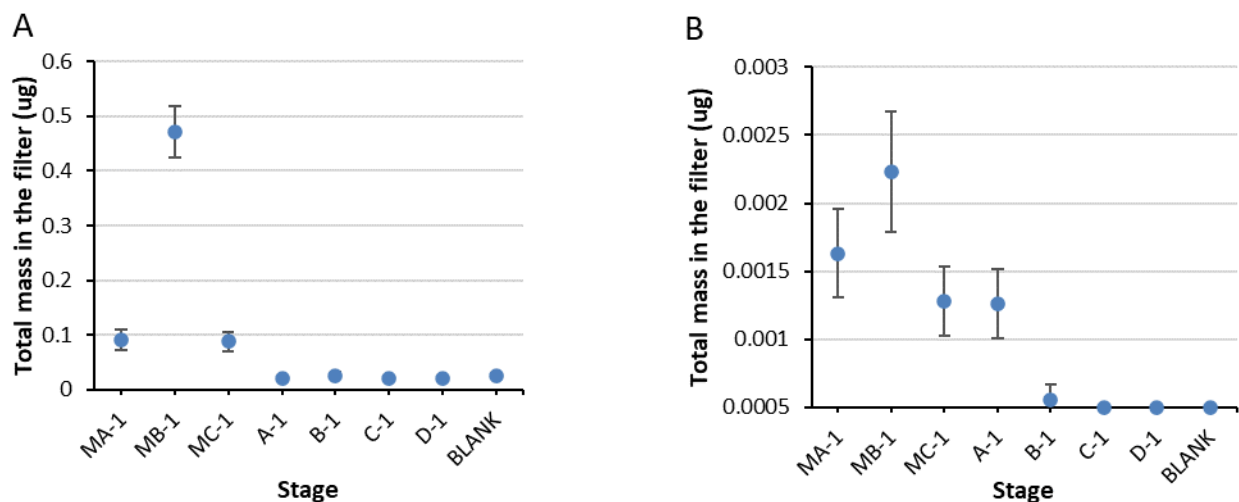
The SEM tabs were monitored post-digestion for residual activity, which was detected. The tabs were then muffled, keeping the temperature just under the silver melting point (825 °C). This caused the substrate to disintegrate, so a subsequent analysis was performed for uranium and any fission products that could be determined over background natural contaminations. A control silver adhesive tab was also melted under similar conditions for background.

Figure I-15 shows the total mass of SNF isotopes recovered from the ashing process. This only comprised of uranium ( $^{238}\text{U}$ ) and plutonium ( $^{239}\text{Pu}$  and  $^{240}\text{Pu}$ ) isotopes. The quantity of material that was sequestered in the silver tab was low in all cases ( $<0.5\ \mu\text{g}$ ), with stage MB-1 having  $5\times$  more retained material within the silver tab than other stages. Table I-9 shows the percentage of  $^{238}\text{U}$ ,  $^{239}\text{Pu}$ , and  $^{240}\text{Pu}$  recovered per stage from the ashing process as compared with the total mass recovered in the initial ICP-MS analysis and reports the final totals of the isotopes collected as aerosols for Test 1.

The sequestered material on the silver adhesive tabs is a consequence of a step in the experiment protocol in which the silver adhesive tab is folded into quarters for removal from the hot cell for ICP-MS. The protocol will be amended with the goal of avoiding this issue for future experiments.



**Figure I-15. Total mass of SNF material recovered from ashing the adhesive tabs used to collect aerosols in the modified Sioutas Cascade Impactor, 3D8E14-2810-2963.**



**Figure I-16. Additional material recovered by ashing: (A) total  $^{238}\text{U}$  from each stage, (B) total  $^{239}\text{Pu}$ , 3D8E14-2810-2963.**

**Table I-9. Total collected isotopic mass by ashing and digestion, 3D8E14-2810-2963.**

Stages	Total $^{238}\text{U}$ / $^{239/240}\text{Pu}$ mass recovered during ashing (ug)	Total isotopic mass measured by digestion during initial processing, ug (see Table I-8)	Total mass of isotopes collected (ashing + digestion), (ug)	Percentage of SNF mass (of $^{238}\text{U}$ , $^{239/240}\text{Pu}$ ) recovered from ashing with respect to the total mass collected from the tab during the initial ICP-MS analysis
MA-1	0.09	84.53	84.62	0.11%
MB-1	0.47	93.43	93.90	0.50%
MC-1	0.09	28.02	28.11	0.32%
A-1	0.02	26.57	26.59	0.08%
B-1	0.02	24.31	24.33	0.08%
C-1	0.02	9.10	9.12	0.22%
D-1	0.02	2.12	2.14	0.94%



## I-4.2 AERO-2

In September 2023, LT Zirc-4-clad specimen 3A1F05-2402-2555 was broken in 4PB, and aerosol collection was completed using the modified Sioutas cascade (7 stages). The specimen has an estimated local burnup of 55 GWd/MTU and a thick waterside cladding oxide thickness of 117  $\mu\text{m}$  (local average) with widespread spalling, as shown in Figure I-17. The specimen weighed 98.4 g pre-test.

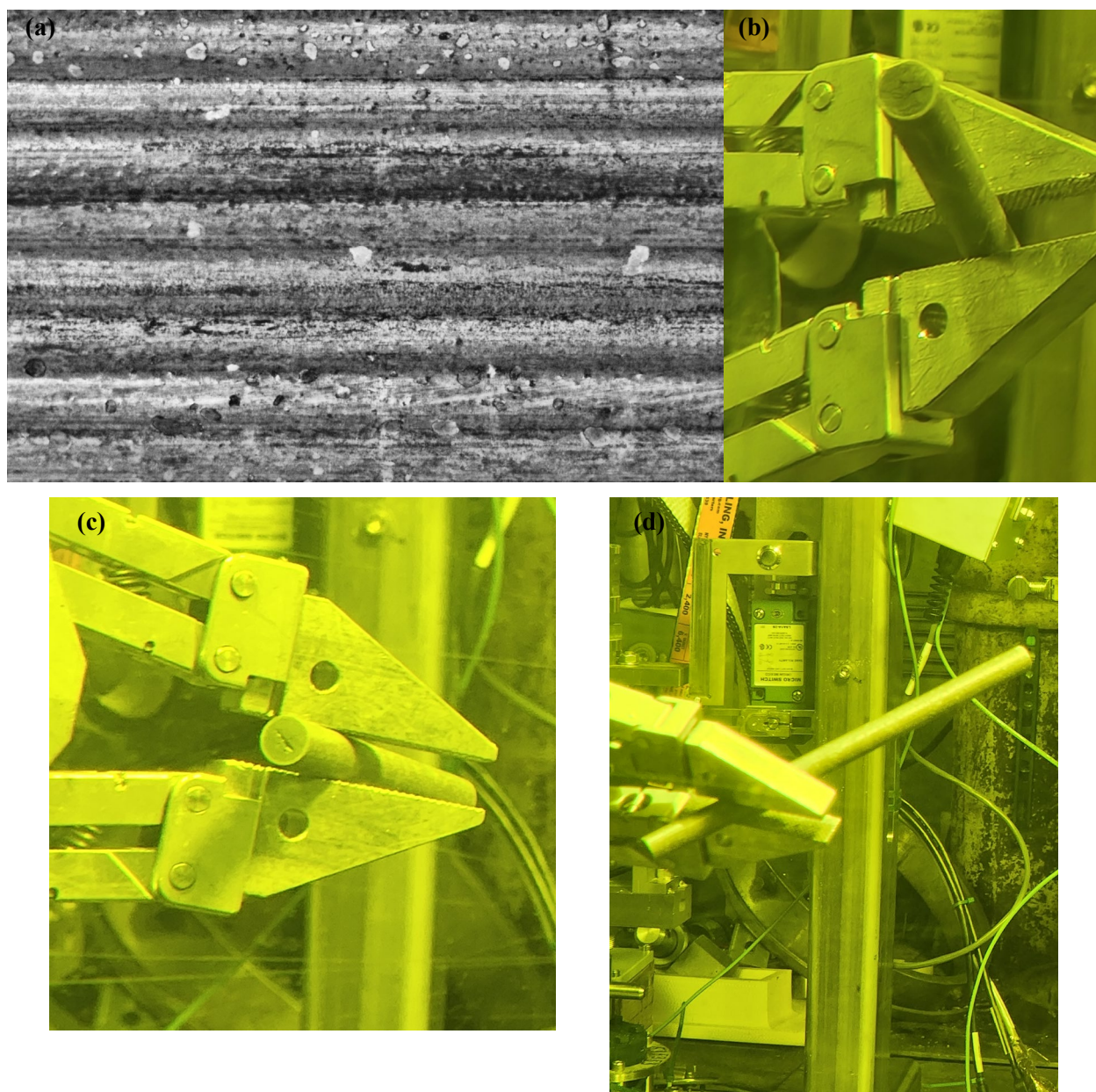


**Figure I-17. Pre-test appearance of 3A1F05-2402-2555, showing (a) the 360° waterside surface of the rod, (b) and (c) the exposed pellet surfaces at the ends of the test segment, and (d) a general view of the rod prior to testing.**



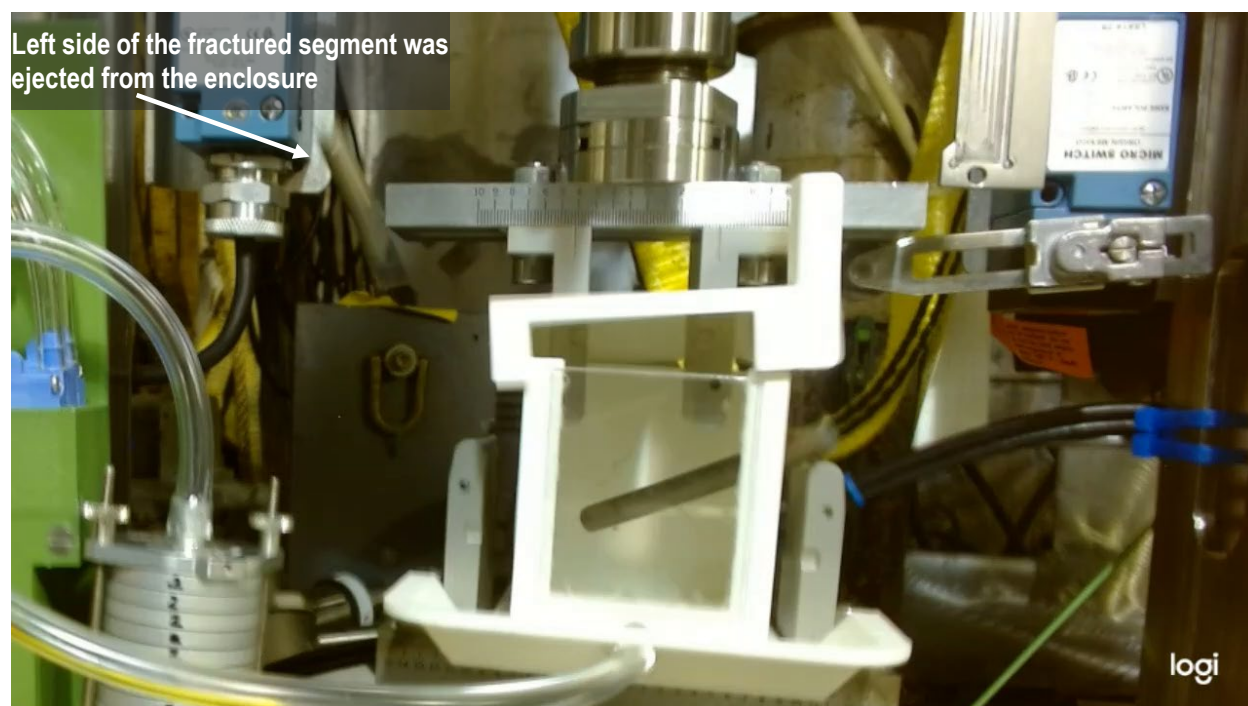
Test 2 was conducted using the protocol described in Section I-5. For test 2, an anti-static coating was added on the enclosure interior to reduce the potential for electrostatic collection of aerosols.

**Table I-10. Test 2, Orifice measurements and evaluated cut points for the cascade impactor used.**

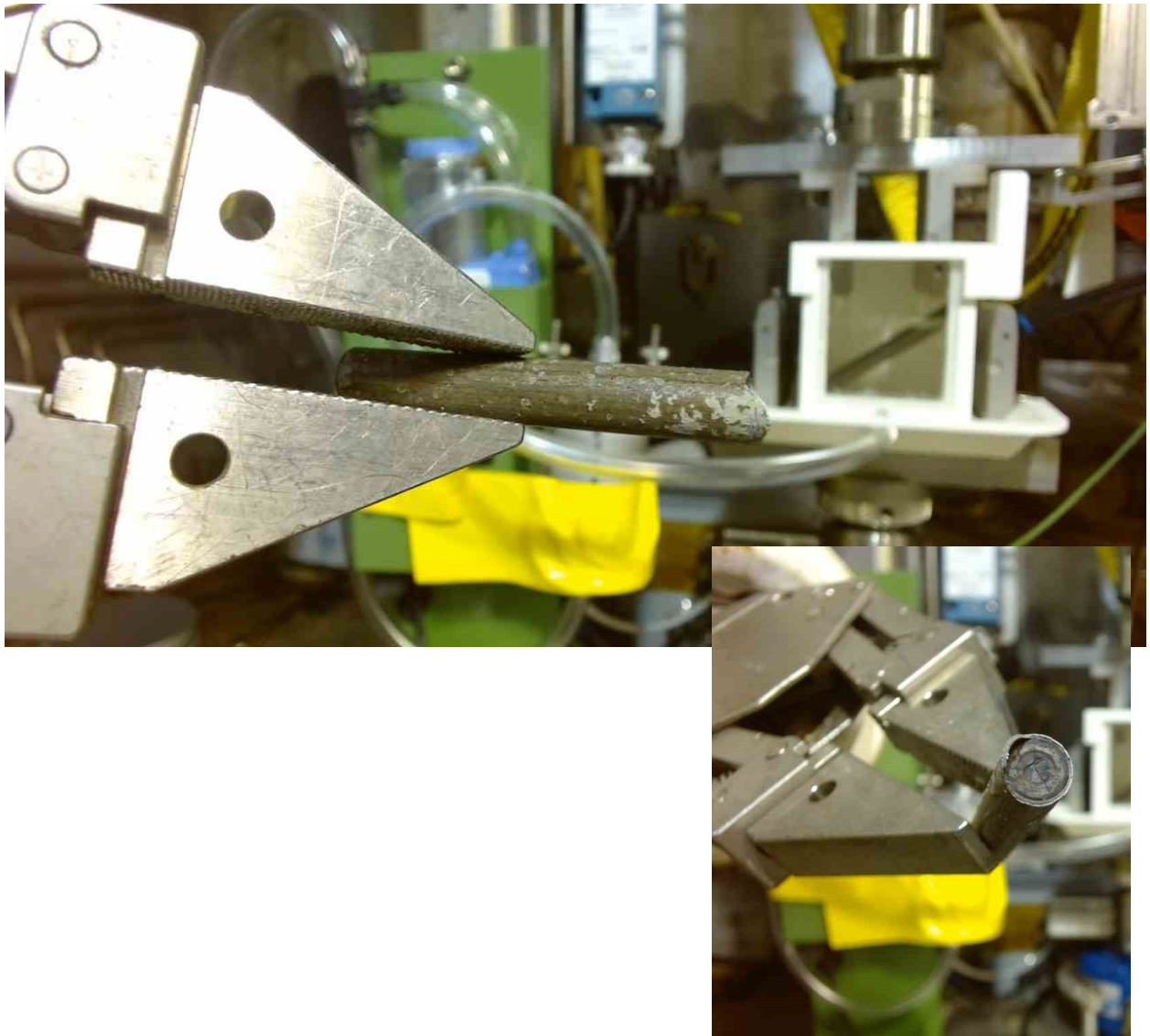
Stage	Measured average orifice length (mm)	Measured average orifice width (mm)	Evaluated d <sub>50</sub> cut point (μm)
MA-2	1.99	0.39	16.27
MB-2	1.95	0.29	11.62
MC-2	1.96	0.20	7.92
PA-2	2.03	0.09	3.71
PB-2	2.03	0.06	1.94
PC-2	2.03	0.04	1.49
PD-2	2.03	0.03	0.66

Figure I-18 provides an image of the segment just after fracture, and Figure I-19 provides post-test images of the broken rod segment. It appears that the segment fractured at the left loading point instead of at the center of the section. Follow-up imaging will be used to determine the location and mode of fracture. The post-test images clearly show that the fracture occurred at a pellet-pellet interface as opposed to in the body of a pellet. The right segment fragment impacted the enclosure lid during the fracture event, and it was lifted briefly from the enclosure base but reseated after the impact. The left fragment was ejected with considerable energy and was retrieved approximately 1 ft from the test frame.

The post-test segment fragments were weighed, along with any gross fragments found in the enclosure. The dust-type material collected in the enclosure, the tubing, and the cascade impactor will be analyzed in FY24. Future tests will include a weighted lid.



**Figure I-18. Image captured during the test showing the trajectory of the segment just after fracture. The test segment fractured at the upper left loading point and part of the specimen was ejected from the enclosure. The enclosure lid was forced upward but resettled after the initial impact.**



**Figure I-19. AERO-2 Segment 3A1F05-2204-2555, post-test.**

## I-5 Airborne Release Fraction and Respirable Fraction

The amount of material at risk for release in the SNF varies based on its elevation during operation because the condition of the pellet varies based on its elevation. It would be expected that elevations within the pellet stack that include more cracks will provide more available surface area for particulate release. For the 6 in. rod length tested, the isotopic source term contained in the rod length was calculated for a generic pellet using the Oak Ridge Isotope Generation (ORIGEN) Assembly Isotopics (ORIGAMI) code under the SCALE suite. The SCALE predictions are based operation of a generic Westinghouse 17×17 assembly with 4%  $^{235}\text{U}$  enrichment to 60 GWd/MTU burnup for 1,150 days and cooled for 10 years, scaled up to the 84.58 g of pellet material in the 6 in. length of rod tested and calibrated to the gamma scans [I-23] for the elevation of the test specimen. The mass of the cladding was neglected in evaluating the releasable and respirable fractions, except for  $^{91}\text{Zr}$ , as it likely came from the fuel rod cladding.

### I-5.1 AERO-1

Figure I-20 shows a histogram of the respirable fraction obtained from the total isotopic mass collected in the Test 1 cascade as a fraction of the available isotopic mass at risk in the fuel. As seen in Figure I-20, the collected isotopes can be binned to identify similar release trends or to examine whether they might be released as agglomerations, solid solutions, or trapped incorporations. Although this gives some idea of the relative releasability of the various isotopes (e.g.,  $^{140}\text{Ce}$  seems to be more readily released, while  $^{91}\text{Zr}$  tends to be retained with the rod), it does not provide evidence of whether the isotopes are released as individual particles or agglomerates. Future experiments will include an SEM characterization of the collected aerosol particles and an EDS analysis to obtain a chemical footprint of the particle distributions to determine if they agglomerate. A dual sampling design modification to accommodate more extensive examinations is discussed in Section I-7.2.

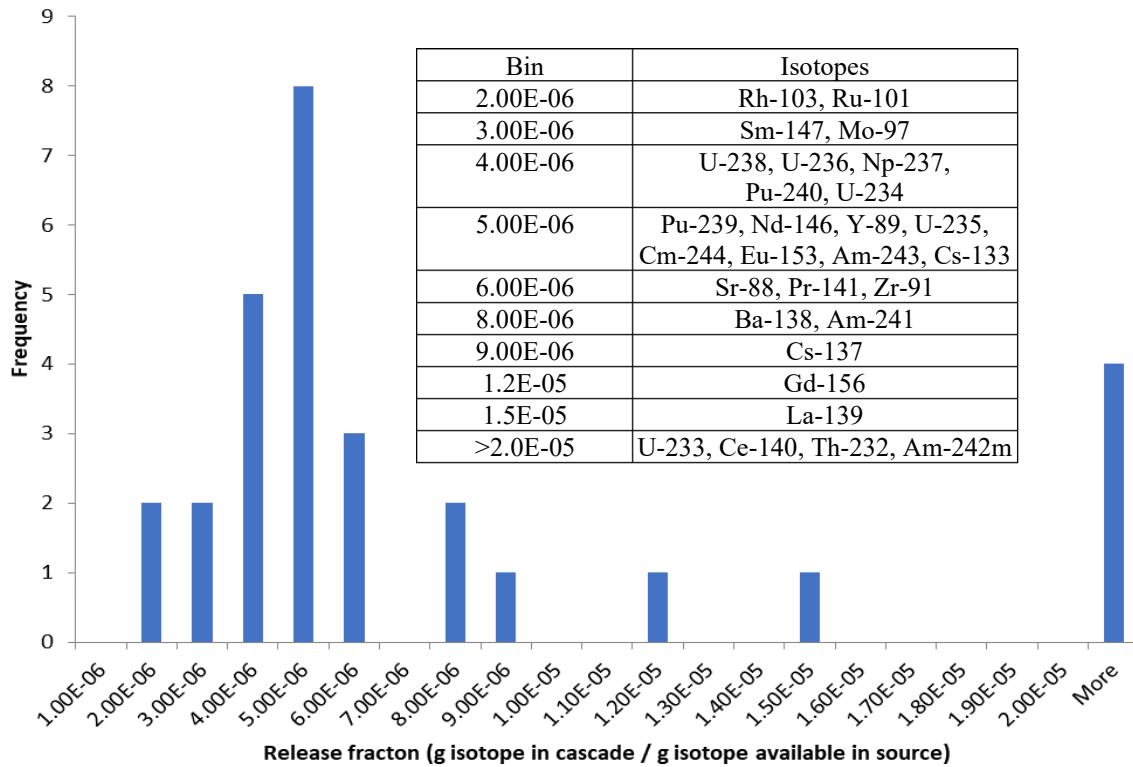
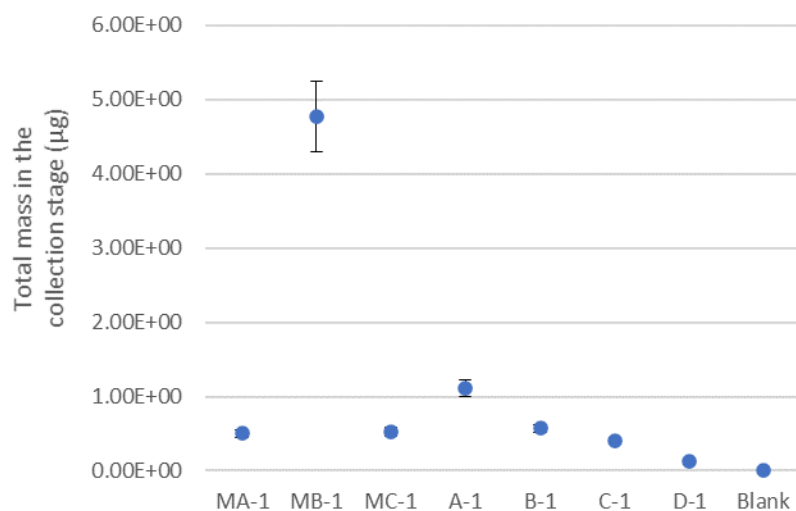
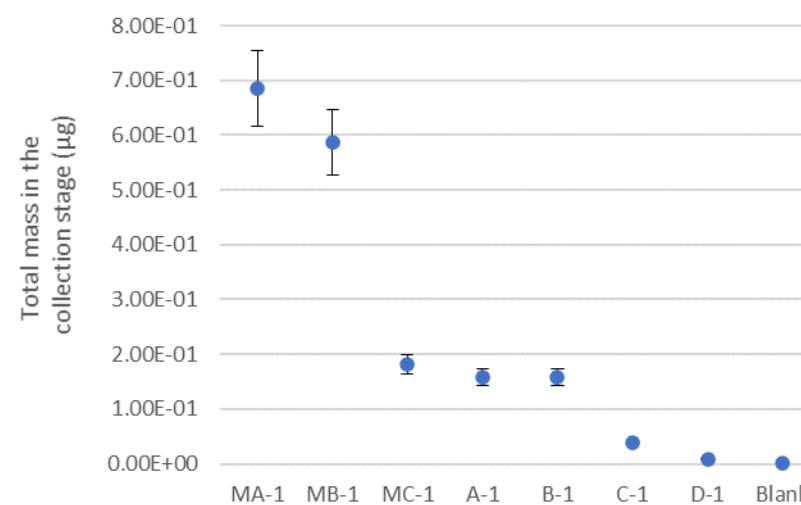
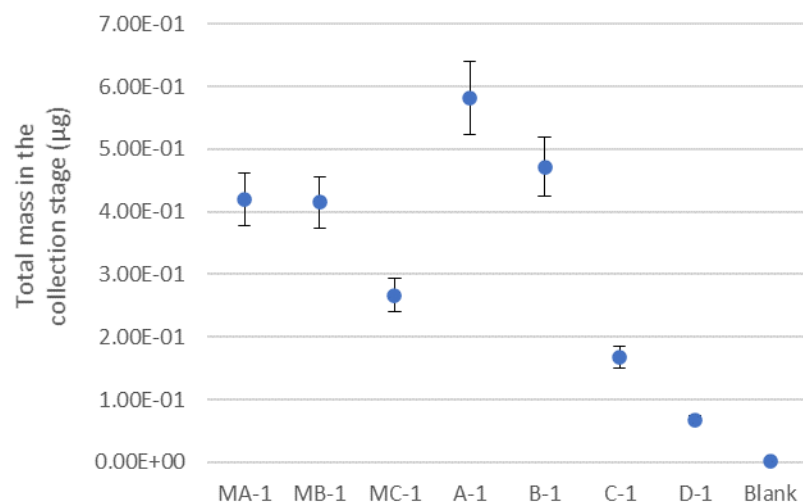


Figure I-20. AERO-1, histogram of total measured mass of isotope / predicted total mass of isotope in a 6 in. test segment.

Figure I-21.  $^{140}\text{Ce}$  distribution in the cascade stages.Figure I-23.  $^{146}\text{Nd}$  particle distribution in the cascade stages.Figure I-22.  $^{139}\text{La}$  distribution in the cascade stages.

AERO-1  
 AED  $D_{50}$  cut point at  
7 LPM,  $\mu\text{m}$   
 MA-1, 15.6  
 MB-1, 11.6  
 MC-1, 7.8  
 A-1, 4.1  
 B-1, 2.1  
 C-1, 1.6  
 D-1, 1.1

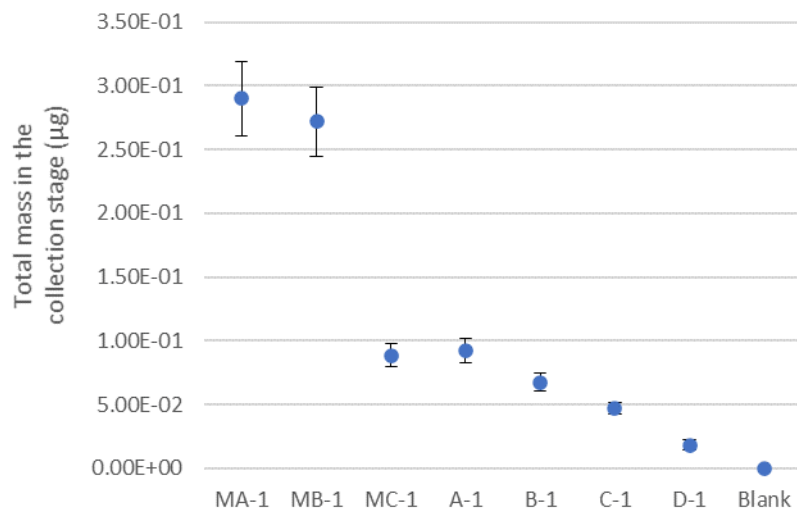


Figure I-24.  $^{137}\text{Cs}$  particle distribution in the cascade stages.

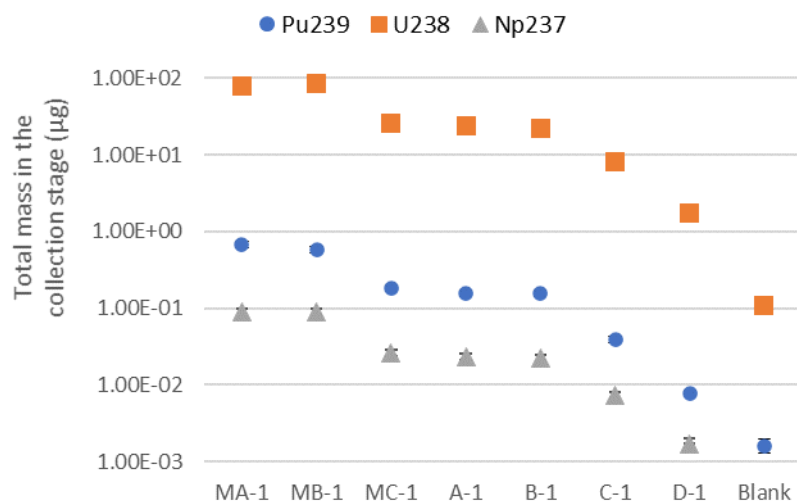


Figure I-25. Actinide particle distribution in the cascade stages.

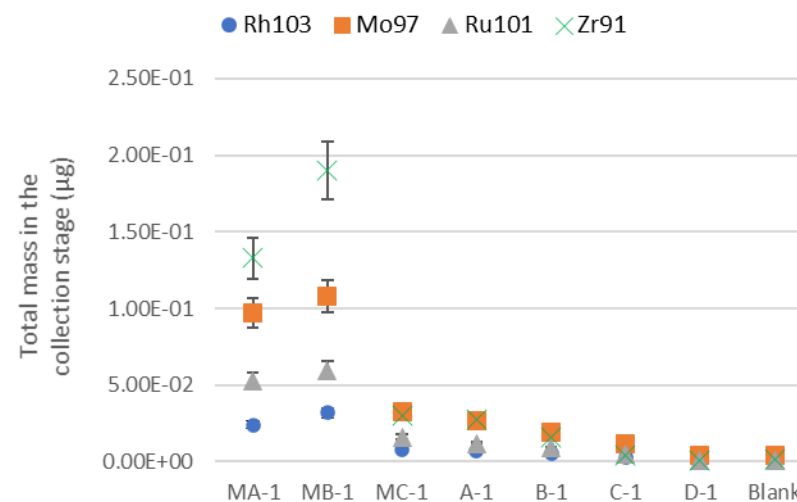


Figure I-26. Epsilon particle distribution in the cascade stages, presented along with  $^{91}\text{Zr}$  for comparison.

AERO-1  
AED  $D_{50}$  cut point at  
7 LPM,  $\mu\text{m}$   
MA-1, 15.6  
MB-1, 11.6  
MC-1, 7.8  
A-1, 4.1  
B-1, 2.1  
C-1, 1.6  
D-1, 1.1

In addition to the total respirable fraction, the respirable fraction by range of AED was calculated by comparing the mass collected by individual cascade stages to the total aerosol dust mass collected. This is expressed as follows :

$$\text{Respirable Fraction}_{(x-y)}(i) = \frac{\text{Mass of particulate collected in the } i^{\text{th}} \text{ stage}}{\text{Total mass of dust} - \text{type particulate released}} , \quad (\text{I-14})$$

where  $i = 1$  to  $7$ ,  $x$  is the lower AED for the stage, and  $y$  is the upper AED for the stage. Consequently, the sum of the stagewise respirable fractions add up to the total respirable fraction.

For this experiment, the mass of the UNF in the tested rod segment is considered to be the available material. Neglecting the mass of the cladding, the mass of fuel pellet material available within the 6-inch long fuel rod segment was calculated as  $\sim 84.58$  g. Based on this approach, excluding the cladding materials, and excluding gaseous fission products, the amount of isotopic material at risk for release as aerosolized particles is near 80 g. The total airborne release fraction is calculated as  $4,615.85 \pm 388.35 \mu\text{g} / 80 \text{ g} = 5.8\text{E-}05 \pm 4.96\text{E-}06$ . Conservatively assuming that all particles collected in the cascade are respirable, the respirable fraction is calculated as the fraction of airborne particles in the respirable range:  $494 \pm 46 \mu\text{g} / 4,615.85 \mu\text{g} = 0.107 \pm 0.010$ .

The size-dependent respirable fractions are presented in Table I-11 and range from 0.00076 to 0.05100. This provides a method to associate specific AEDs with a rate of releasability.  $^{238}\text{U}$  is by far the most prevalent isotope detected in the aerosol particulate, which is consistent with the fact that most of the source material is  $^{238}\text{U}$ . Because larger AED respirable particulate was collected at a much higher fraction, and larger particulates settle more quickly, it can be concluded that settling time must be considered when calculating the dose estimates for a postulated accident event.

Furthermore, the data tend to support the theory that particular isotopes tend to be released within a specific range of particulate sizes, and they also may be more prone to aerosolization and release. Although most isotopes have the same concentrations in the aerosols as in the source fuel, several seem to be at a higher concentration, thus indicating that they are more likely to aerosolize, including  $^{138}\text{La}$ , isotopes of americium, isotopes of cesium, and  $^{138}\text{Ba}$ .

Given the measured/predicted isotopic content of the 6-inch long specimen and the quantity of each isotope measured in each stage of the cascade, the respirable fraction of the individual isotopes can also be calculated as follows and are provided in Table I-12:

$$\text{Respirable Fraction}_{(\text{isotope})} = \frac{\text{Mass of isotope collected in the impactor}}{\text{Total mass of dust} - \text{type particulate released}} . \quad (\text{I-15})$$

The respirable fraction of the individual isotopes measured range from  $5.30\text{E-}02$  for  $^{238}\text{U}$  to  $6.12\text{E-}07$  for  $^{233}\text{U}$ . The respirable fraction tends to trend well with the source concentration, as shown in Figure I-27, except for  $^{139}\text{La}$ ,  $^{140}\text{Ce}$ , and  $^{242\text{m}}\text{Am}$ . The histogram of the frequency of release fractions (isotope mass captured in the cascade impactor/isotope mass available for release from the source pellets) shown in Figure I-20 indicates that these same isotopes, along with  $^{233}\text{U}$  and  $^{232}\text{Th}$ , appear to have higher than typical release fractions.

**Table I-11. AERO-1, measured respirable fractions by AED.**

Stage	Size (AED)	Respirable fraction
MA -1	>15.6	$0.05100 \pm 0.00557$
MB -1	>11.5	$0.03024 \pm 0.00327$
MC -1	>7.7	$0.00992 \pm 0.00107$
PA -1	>4.1	$0.00680 \pm 0.00078$
PB -1	>2.0	$0.00600 \pm 0.00070$
PC -1	>1.5	$0.00236 \pm 0.00026$
PD -1	>1.0	$0.00076 \pm 0.00008$
Total		$0.107 \pm 0.010$

**Table I-12. AERO-1, measured respirable fractions by isotope.**

Isotope	Respirable fraction	Isotope	Respirable fraction
Am-241	1.54E-04	Pu-239	3.94E-04
Am-242	9.48E-05	Pu-240	2.01E-04
Am-243	3.18E-05	Rh-103	1.73E-05
Ba-138	2.68E-04	Ru-101	3.39E-05
Ce-140	1.74E-03	Sm-147	1.16E-05
Cm-244	9.14E-06	SR-88	4.66E-05
Cs-133	1.52E-04	Th-232	1.22E-06
Cs-137	1.90E-04	U-233	6.12E-07
Eu-153	1.65E-05	U-234	1.47E-05
Gd-156	4.98E-05	U-235	2.65E-04
La-139	5.18E-04	U-236	3.57E-04
Mo-97	6.50E-05	<b>U-238</b>	<b>5.30E-02</b>
Nd-146	1.01E-04	Y-89	5.29E-05
Np-237	5.59E-05	Zr-91	8.70E-05
Pr-141	1.68E-04		



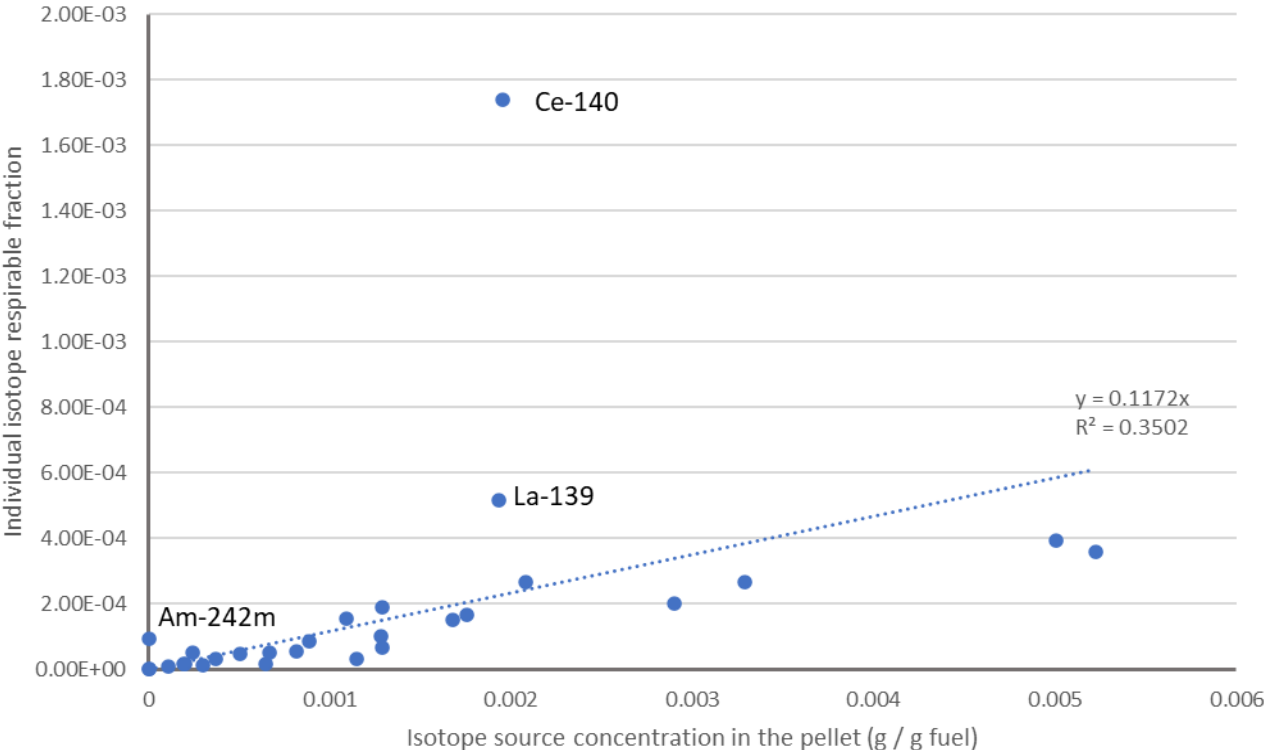


Figure I-27. AERO-1, individual isotope respirable fraction plotted with concentration of the isotope available in the source pellets.



## I-6 Cascade verification testing and sample processing testing

The goal of the aerosol collection work is to measure the respirable fraction of the gross particulate released. Towards that end, only the gross quantity of SNF captured by the whole cascade impactor is needed, and the size distribution of the respirable particulate on each collection stage is not specifically required. Given the collection range of the overall impactor (up to 15  $\mu\text{m}$  AED), there is a very high confidence that the respirable range of particulate is effectively and conservatively covered.

However, understanding the size distribution of the aerosols collected can lead to enhanced understanding of the release mechanisms. To provide additional assurance that each collection stage collects the range of particle sizes it was designed for, verification of the modified cascade impactor design was completed using physical testing and computational fluid dynamics (CFD) modeling, as described in the following sections.

### I-6.1 Verification using physical testing

Extensive testing of the modified cascade impactor was conducted to verify the calculated cut points of the individual stages. A powder dispenser was used to puff a known powder mixture into the collection system. After testing, the stages were disassembled, and the filters were analyzed. The visible collected particles were characterized using SEM. The image analysis steps adopted for characterizing and counting the particles are discussed in the next section.

All validation tests were conducted using purchased International Organization of Standardization (ISO) dust mixtures that consisted of a number of compounds of varying density and particle sizes. Table I-13 lists the ISO dust concentration used for the tests. Several types of dust were used in testing: ISO 12103-1 A1 Ultrafine, A4 Coarse test dust, and  $\text{CeO}_2$  powders of different particle sizes (3  $\mu\text{m}$ , 5  $\mu\text{m}$  & 14  $\mu\text{m}$ ). It was observed from SEM characterization that the  $\text{CeO}_2$  powders had a smaller size distribution than the rated particle sizes. Because the target aerosol collection size for the SNF rod tests is <10  $\mu\text{m}$  in diameter, the ultrafine test dust is more representative of the diameters to be collected during the test, so it was used for the final verification tests. The composition and size distribution specification for the ultrafine test dust is provided in Table I-13.

Several types of tests were performed, including:

- Pressure drop testing of individual stages and the assembled cascade
- Collection of various dust sources with the assembled modified cascade
- Collection of dust with varied stage order
- Collection of dust using various filter materials (paper, quartz, silver, carbon tabs [beige and black in coloration], no filter)
- Variation of the pump flow rate.

For brevity, only select results from the tests performed are reported here, but all tests are documented in the experiment log book.

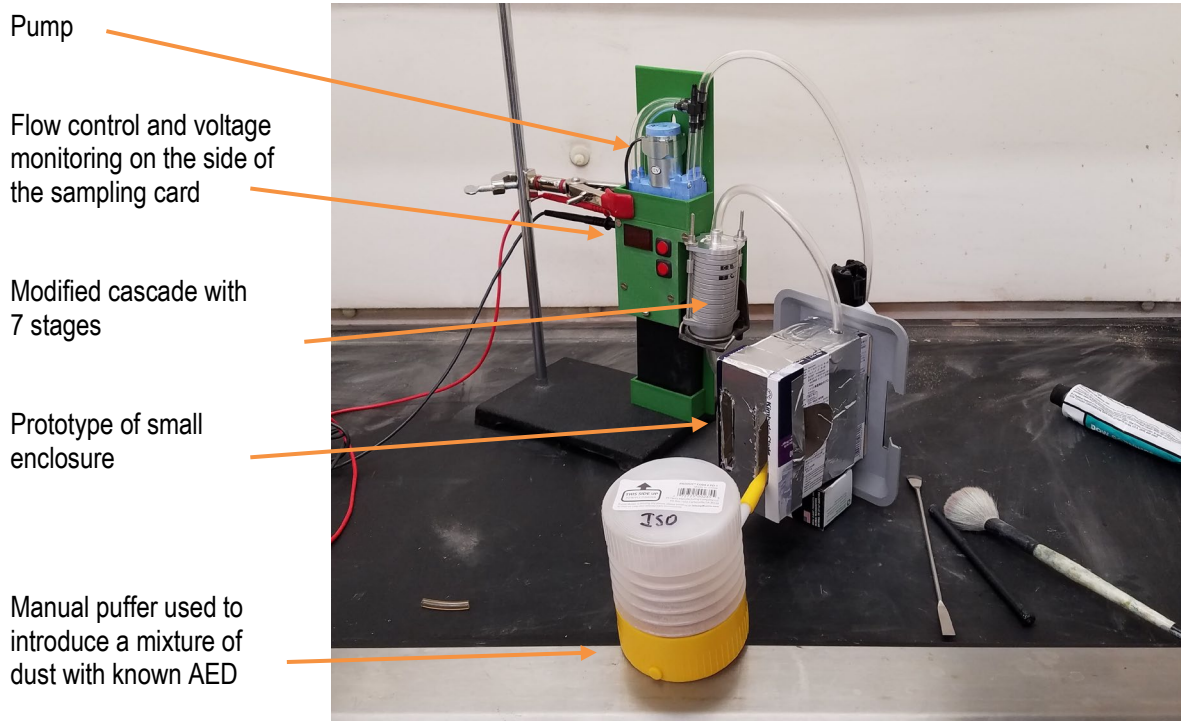


**Figure I-28. Experimental setup for dust-collection validation tests with the modified cascade and a prototype of the small enclosure.**

**Table I-13. Composition and particle size distribution of ultrafine ISO test dust.**

Component	Quantity
Silica (fine dust)	69 – 77%
Aluminum oxide	8 – 14%
Calcium oxide (mineral)	2.5 – 5.5%
Potassium oxide (mineral)	2 – 5%
Sodium oxide (mineral)	1 – 4%
Iron (III) oxide (hematite)	4 – 7%
Magnesium oxide	1 – 2%
Titanium dioxide	0 – 1%
<i><b>A1 ultrafine test dust particle size distribution by volume</b></i>	
Particle diameter (µm)	% less than
0.97	3.0 – 5.0
1.38	7.0 – 10.0
2.75	23.0 – 27.0
5.50	65.0 – 69.0
11.00	95.5 – 97.5
22.00	100.0

### I-6.1.1 Pressure drop tests

Experimental pressure drop measurements were collected using a setup similar to that used for the verification testing (shown in Figure I-28), except that a flow meter and a pressure meter were included, as shown in Figure I-29. The vacuum pump was first turned on and adjusted to achieve the desired steady state flow rate. Experimental measurements were taken at each stage, along with overall pressure drops for the 7-stage Sioutas cascade impactor at inlet flow rates of 6 and 7 LPM. The first tests were conducted using the full stack. Individual stage pressure drops were calculated by measuring the pressure drop across the stack without that stage and then subtracting the minus-one measurement from the full stack measurement. An alternative measurement technique of successively removing the stages (first 1, then 2, then 3, and so on) produced similar pressure drops for the individual stages. The results are provided in Table I-14 and are used in conjunction with the computational fluid dynamics (CFD) models to verify expected performance with the modified stages.

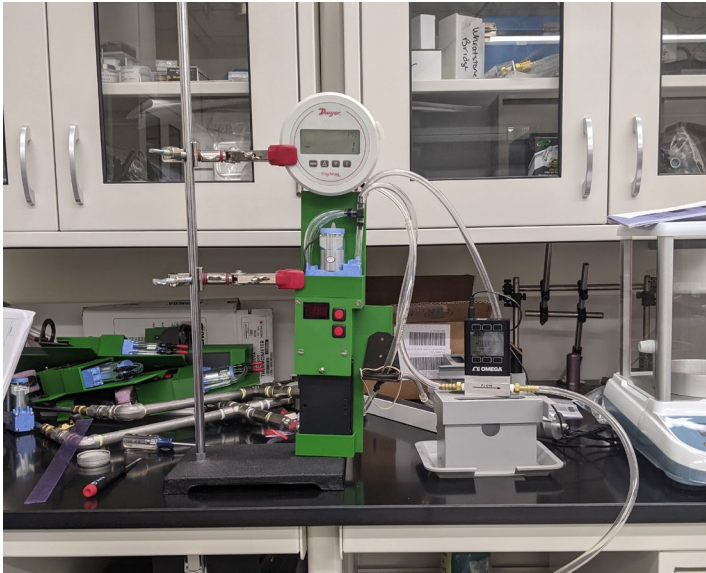


**Figure I-29. Experimental test setup of the 7-stage modified Sioutas cascade impactor with flowmeter and the pressure transducer.**

**Table I-14. Experimentally measured pressure drop values for the modified Sioutas cascade impactor at 6 and 7 LPM.**

Impaction stage	Measured $\Delta P$ at 7 LPM (Pa)	Measured $\Delta P$ at 6 LPM (Pa)
Stage MA	0	0
Stage MB	0	0
Stage MC	$30 \pm 30$	$18 \pm 30$
Stage PA	$62 \pm 30$	$25 \pm 30$
Stage PB	$128 \pm 30$	$99 \pm 30$
Stage PC	$220 \pm 30$	$178 \pm 30$
Stage PD	$675 \pm 30$	$481 \pm 30$
Overall	1,156	867

### I-6.1.2 Verification Testing Using ISO Dust Mixtures

Multiple tests were performed using ISO dust mixtures and ceria powders to examine the collection efficiency of the modified Sioutas cascade using the setup shown in Figure I-28. The surrogate dust deposits were weighed, imaged (see Figure I-30 for a photographic example), and analyzed. The performance of the modified cascade was within expectations.

The assembled order of the stages was changed to evaluate individual stage efficiency (no collection on stages with a higher cut point placed below a lower cut point stage). The filters were weighed pre- and post-collection to determine the amount of powder collected. In the test results shown in Figure I-31, the deposited material from filter MB was dislodged and lost as a result of the handling process. This highlighted the fact that sticky carbon tabs, as shown in Figure I-32, were more efficient in retaining particles deposited on the stage and preventing loss through handling. SEM samples were taken from each filter for evaluation. Each sample was collected from the center and sides of the filter to check for a change in distribution along the air flow path.

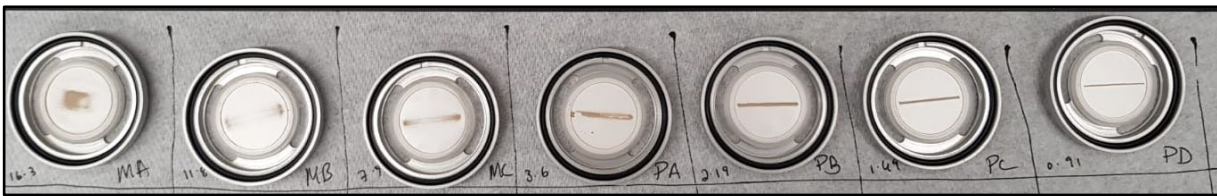


**Figure I-30. Silver filters imaged after validation experiments with ISO dust.**

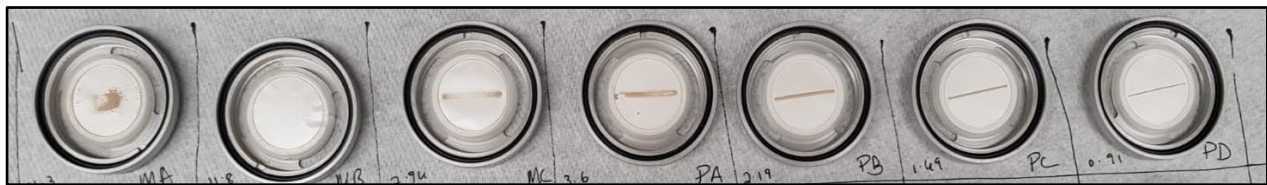


**Figure I-31. Silver filters imaged after weighing. The filter MB material deposit was lost during the weighing process.**

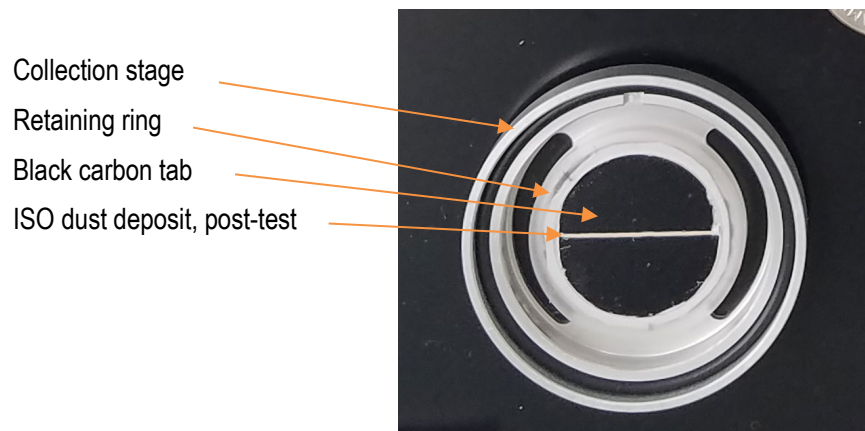


**Figure I-32. A black carbon tab used to collect ISO particle samples. In the hot cell, a beige-colored tab will be used to allow for visual identification of UO<sub>2</sub> deposits.**

To evaluate the individual stages, the stack was arranged out of order as MB, MC, MA, PA, PB, PC, and PD, and ISO dust was puffed into the collection box. Figure I-33 shows the filters with the collected ISO



dust particles from this run. It was observed that filter MA showed no collection compared to that of MB, MC, and the purchased stages. This produced the expected result: MB and MC collected all the larger particles from the air stream, but they left behind smaller particles. There were no larger particles remaining for deposit on MA, and, as a result, it was empty.

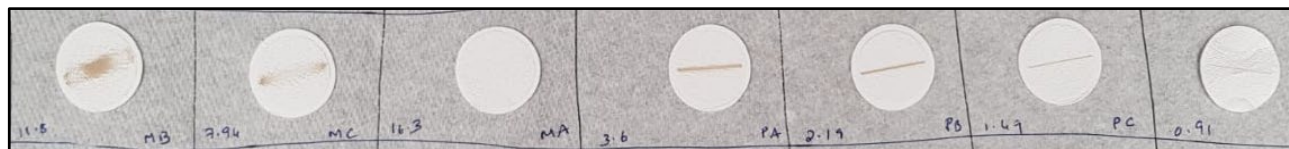


**Figure I-33. The out-of-order placement of MA below MB and MC produced no deposits on MA, as expected, because the larger particles were already removed in the stages above it (quartz filters).**

All tests with the ISO dust resulted in deposits on the orifice plate, in addition to the collection plate, as shown in Figure I-34. The amount varied, depending on the volume of dust introduced for the test. It is unlikely that a large amount of SNF dust will be deposited on the orifice plates, because the volume of SNF dust is expected to be small compared to that used in the ISO dust tests; nevertheless, SNF sampling should include the orifice plates.



**Figure I-34. Typical ISO dust deposit on the orifice plate's surface.**

### I-6.1.3 SEM image processing

Visually verifying the distribution of the particle sizes deposited on each stage requires an image of the deposits and a method for counting and measuring each particle. Although the primary data for the aerosol collection experiment will be generated using mass spectrometry, it is desirable to provide secondary data about the size distribution of the aerosols based on visual imaging. For particles the size of aerosols, imaging capable of resolving each particle requires SEM. Representative images of the deposited SNF material on each stage of the cascade can be acquired using the IFEL's SEM. With confidence in the capabilities of the cascade, imaging and image processing are not strictly required; however, the additional evidence provided by the images is considered extremely useful and relevant. Image processing tools are available, but the type of image acquired in this test (many small particles in a pile) is very difficult to process reliably. Also, only the visible particles can be characterized, and those below the top layer are ignored. Therefore, image processing cannot provide a complete tool to evaluate the resulting material collection on the various cascade stages, but it can provide verification that the visible particles fit the expected distribution. A literature review was completed, and existing tools in MATLAB [I-13 through I-18] and IMAGEJ Fiji [I-19] were selected for use.

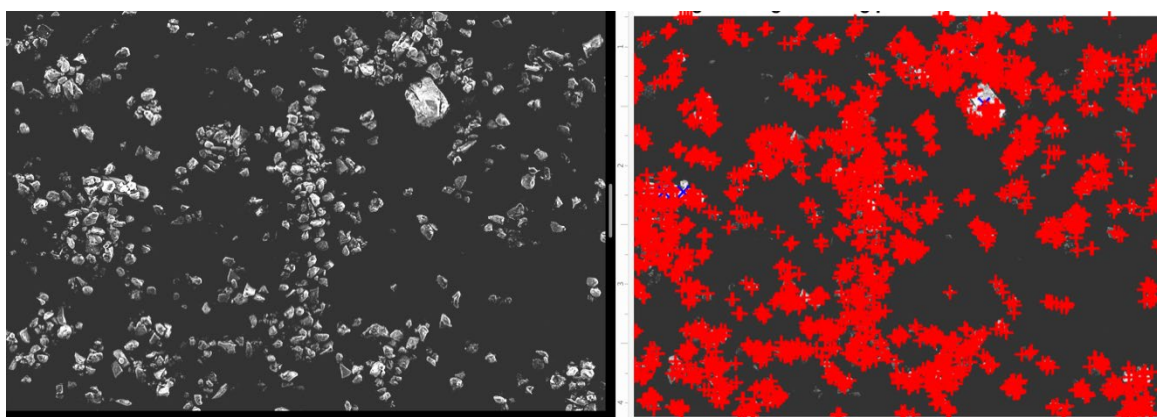
To verify the visual counting and measurement process, samples from the ISO dust test were evaluated. A MATLAB script 'Count\_Measure\_Blobs' was employed to count the collected aerosol particles from the SEM images. The script converts images to grayscale before setting a threshold based on the highest pixel count, and it also connects the pixels around a specific, central pixel to identify individual particle regions. The regions are then combined to generate a labeled binary image before being counted. The *regionprops* function is then used to obtain the mean pixel intensity, area, perimeter, centroid, and diameter of particles (blobs) in the region. Further information on the script and methods can be found on the Mathworks website's Image Analysis toolbox [I-13].

Table I-15 gives the percentage of particles collected across MA, MB, MC, PA and PB for the different particle sizes in ISO dust, as counted by the MATLAB script. The first three stages (the added stages) collected most of the large particles, but they also picked up smaller particles that appear to be adhered to the large particles. This is likely the result of agglomeration from humidity. It was also noted that the lower four stages (the as-received purchased cascade stages) did not pick up any of the large particles and thus follow the designed cut point trends at 7 LPM. Unfortunately, stages PC and PD were omitted from this analysis as the particles were highly agglomerated and the MATLAB script was picking up agglomerated particles as giant blobs as seen in Figure I-37 and Figure I-38.

The unusually high number of smaller particles (0–1.5  $\mu\text{m}$ ) and agglomerated particles picked up by the first three stages prompted a more detailed examination of the particle counting techniques used in this study. Several errors were observed when the procedure was used directly without pre-processing the SEM image. The errors were related to over estimation and misrepresentation of agglomerated and low-contrast particles as separate or combined blobs, as illustrated in Figure I-35, Figure I-36, and Figure I-37. Figure I-36 shows a high magnification image of the filter from stage MA, with ISO dust collection along with the labeled image from the MATLAB script. The error shown resulted from cracks and crevices in large particles, which led to a break in the pixel connectivity. This caused the script to identify multiple miniscule particles instead of one single large particle.

**Table I-15. Percentage of ISO dust particles collected across various size groups for the 7 stages at 7 LPM, counted with the MATLAB script without preprocessing.**

Distribution ( $\mu\text{m}$ )	MA %	MB %	MC %	PA %	PB %
0–0.5	15	0	19	0	67
0.5–1	29	38	12	8	13
1–1.5	13	33	30	0	25
1.5–2	22	22	13	22	22
2–2.5	13	26	23	28	10
2.5–3	18	22	10	38	12
3–3.5	26	21	12	38	3
3.5–4	29	18	26	24	3
4–4.5	44	15	22	19	0
4.5–5	33	33	26	7	0
5–5.5	26	9	65	0	0
5.5–6	50	22	28	0	0
6–6.5	31	6	56	6	0
6.5–7	54	0	46	0	0
7–7.5	30	10	60	0	0
7.5–8	67	0	33	0	0
8–8.5	75	0	25	0	0
>8.5	43	19	38	0	0



**Figure I-35. SEM image of MA filter with ISO dust and the particle count outcome from the MATLAB script showing overestimation of particles caused by poor thresholding.**

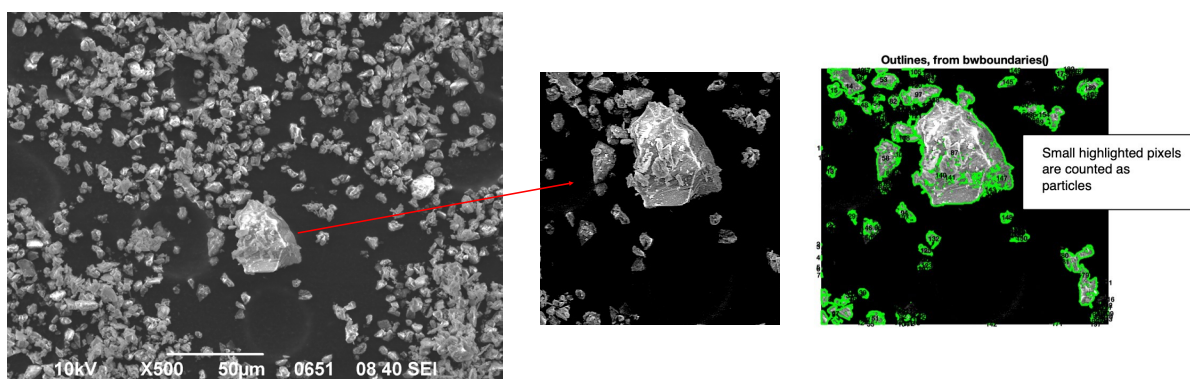


**Figure I-36. High magnification SEM image of MA filter with ISO dust and the particle count outcome from the MATLAB script showing separate particles being identified in a large particle with minor contrast variations within the region.**

Figure I-37 shows a high magnification image of filter MC with ISO dust collection, along with the binary image outcome from the MATLAB script image processing steps. It can be seen that agglomerated particles with low boundary resolution are counted as giant particles, thus leading to misrepresentation of the particle ranges collected.

Several approaches were tried to rectify these problems, including sophisticated thresholding techniques (Ostu [I-14]), segmenting the image into smaller images and recombining (adaptive thresholding and binarization [I-15]), finding edges before binarizing [I-16], using different structuring element functions for reconstruction (opening and closing) to distinguish particle edges before counting [I-17], and watershed segmentation [I-18]. Furthermore, the images were also preprocessed using ImageJ and Fiji software before counting.

For this application, the best approach was found to be using the Trainable Weka Segmentation [I-19], a machine learning tool in Fiji for preprocessing images before counting the particles using the MATLAB script with Ostu's thresholding approach.

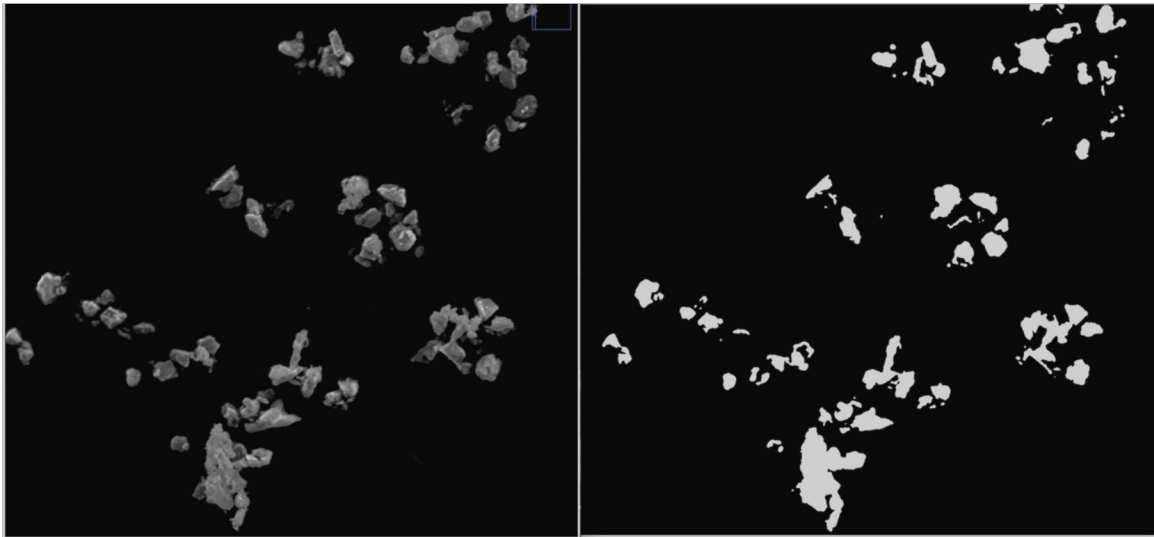


**Figure I-37. High magnification SEM image of MC filter with ISO dust and the binary image generated by the MATLAB script showing small particles with low pixel intensity variations merged into one large blob.**

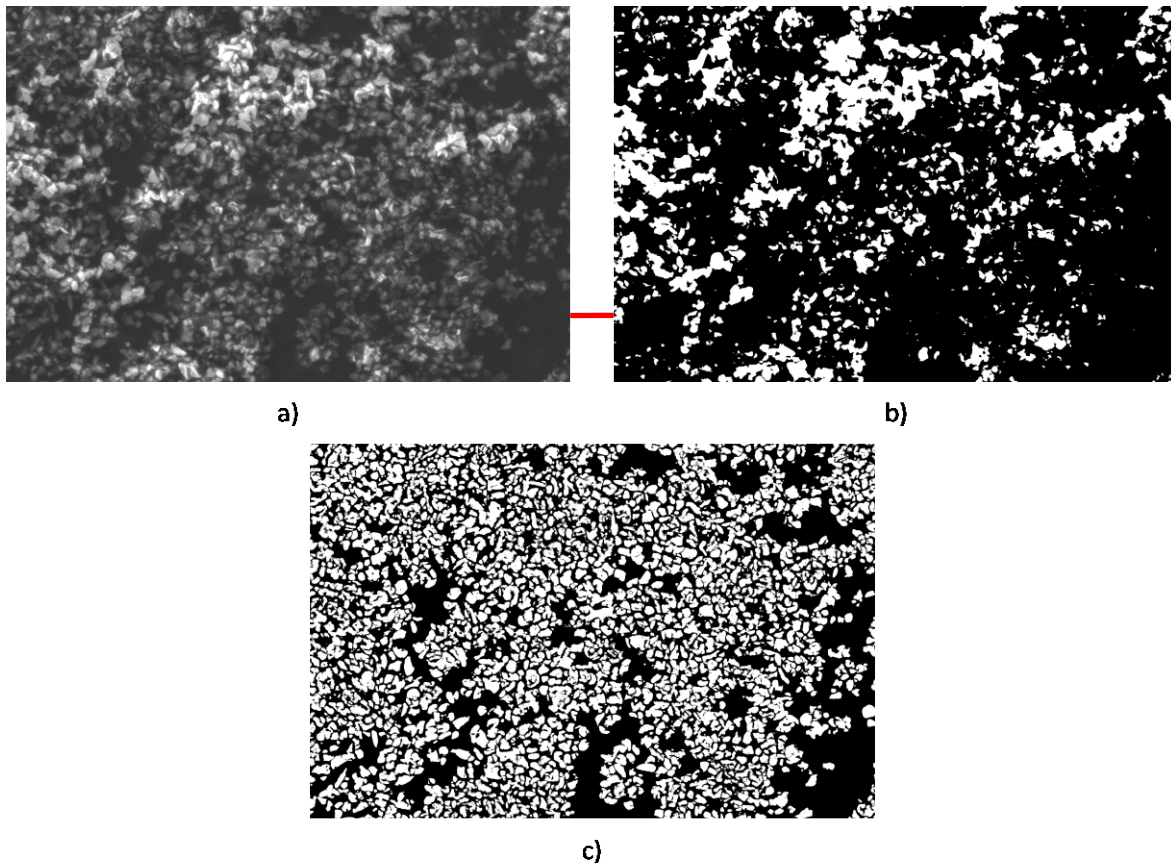


**Figure I-38. (a) SEM image of PC filter with ISO dust, (b) binary image output of (a) from the MATLAB script without preprocessing, and (c) trainable Weka segmented image after binarization showing a very effective approach for identifying and isolating particles.**



These image processing techniques were implemented, and the filters were reanalyzed to obtain the percentage of particles collected for the different particle sizes in ISO dust as counted by the MATLAB script. The data are presented in Table I-16. Using this processing technique, stages PB, PC, and PD collected most of the smaller particles between 0.1–1.5  $\mu\text{m}$ , and the machined stages collected very few particles in this size range. MA has a wide range of collection. Stage PA collection is low compared to the other stages.

Validation of the modified Sioutas cascade performance through image analysis will continue, with active investigation of improvements in the counting scripts and image preprocessing. Further validation of the machined stages and the cascade impactor was performed computationally by modeling the impactor and conducting fluid dynamics simulations to analyze the trends observed in the processed image data.

**Table I-16. Percentage of ISO dust particles collected across various size groups of ISO dust powders for the 7 stages at 7 LPM, as counted using the MATLAB script after preprocessing the SEM images.**

Distribution ( $\mu\text{m}$ )	% MA	% MB	% MC	% PA	% PB	% PC	% PD
0–0.5	1	6	7	3	24	28	32
0.5–1	11	19	16	5	0	21	28
1–1.5	14	11	11	4	49	4	8
1.5–2	6	14	10	6	50	10	4
2–2.5	13	26	11	7	37	0	7
2.5–3	4	33	17	8	29	8	0
3–3.5	7	60	13	20	0	0	0
3.5–4	19	38	19	13	13	0	0
4–4.5	29	33	24	10	5	0	0
4.5–5	20	50	20	0	10	0	0
5–5.5	7	21	36	7	29	0	0
5.5–6	33	44	22	0	0	0	0
6–6.5	25	25	25	15	0	0	0
6.5–7	25	25	25	7	0	0	0
>7	53	13	27	5	0	0	0

## I-6.2 Verification using computational fluid dynamics tools

The flow distribution and particle deposition on the individual stages of the cascade impactor were investigated using the commercial computational fluid dynamics (CFD) code, STAR-CCM+ (Version 2021.1 Build 16.02.008) from Siemens [I-20], an American Society of Mechanical Engineers (ASME) Nuclear Quality Assurance (NQA-1)–compliant CFD solver. STAR-CCM+ has been extensively benchmarked and applied to various areas, including multiphase flows, external aerodynamics, reacting flow networks, and treatment of complex geometric shapes. STAR-CCM+ uses a finite-volume formulation to solve a set of conservation equations for mass, momentum, and energy, along with models that provide closure to the Reynolds-Averaged Navier-Stokes (RANS) equations describing turbulent flow on a finely discretized computational grid. The CFD simulations discussed here are run on high-performance computing (HPC) resources hosted by ORNL’s Nuclear Energy and Fuel Cycle Division (NEFCD).

As a starting point, the commercially available as-manufactured Sioutas cascade (used in Test 1) was modeled and used to verify the simulation's basic functionality. This initial simulation used the manufacturer's recommended inlet flow rate of 9 LPM. The model was then extended to the modified 7-stage impactor. The 3D geometry of the 4-stage cascade impactor is shown in Figure I-39. Only the fluid domain shown in Figure I-39(b) is modeled; the solid-fluid interfaces are modeled as walls. The flow direction is from left to right, with the gravitational vector in the positive y-direction. In an actual test, a vacuum pump will be operated (shown in Figure I-4) with the suction side at the outlet and the induction side at the inlet of the cascade impactor.

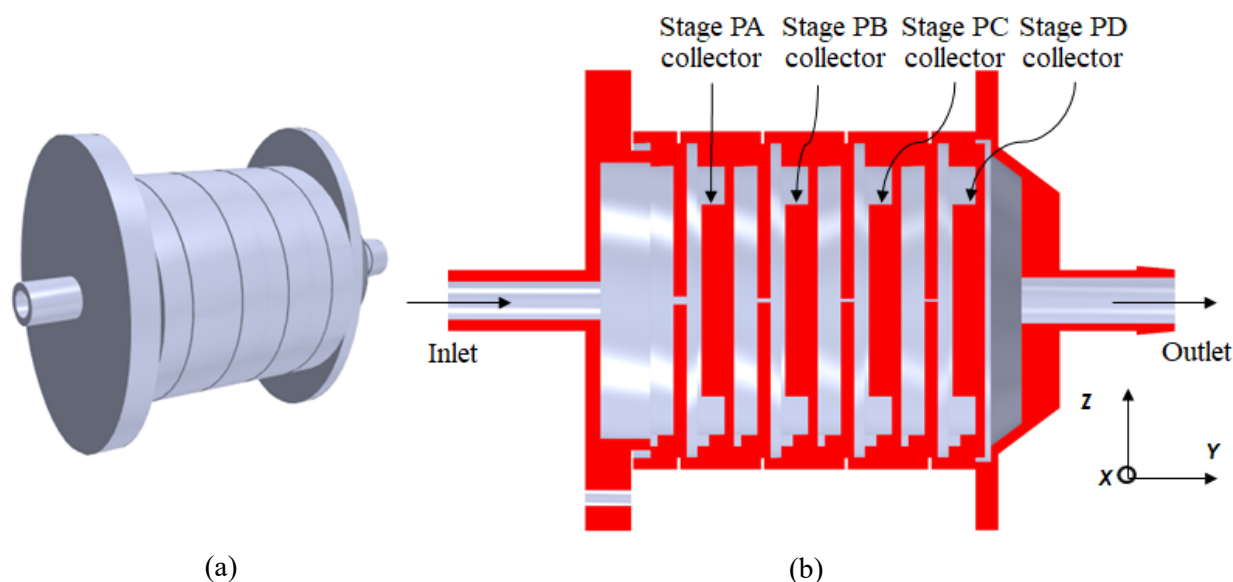


**Figure I-39. (a) Isometric view of the Cascade impactor showing the 4 purchased stages, including inlet and outlet plates; (b) a cross sectional view of the impactor with the solid domain shown in red and the fluid domain shown in gray.**

In the model, the long, flexible tubing in the experimental setup was replaced by a rigid pipe geometry which is adequately extended to ensure a fully developed flow at the inlet of the cascade impactor over the range of simulated Reynolds numbers. The dimensions of the orifices for the 4 stages used in the CFD model were based on microscopic measurements, as discussed in Section 0. An example of one such measurement (X-Z plane) of the orifice width for stage PD at various locations is shown in Figure I-40. The mean measured orifice widths for all 4 stages are listed in Table I-17. The separation distance,  $S$ , is defined as the distance between the orifice exit and the impaction plate. Although the specifications for the first three stages match well with the reference specification [I-5], there is a considerable difference in stage PD measurements for orifice width and length. The CFD model is based on the microscopic measurements, given that the stage pressure drop in particular is very sensitive to the orifice dimensions.

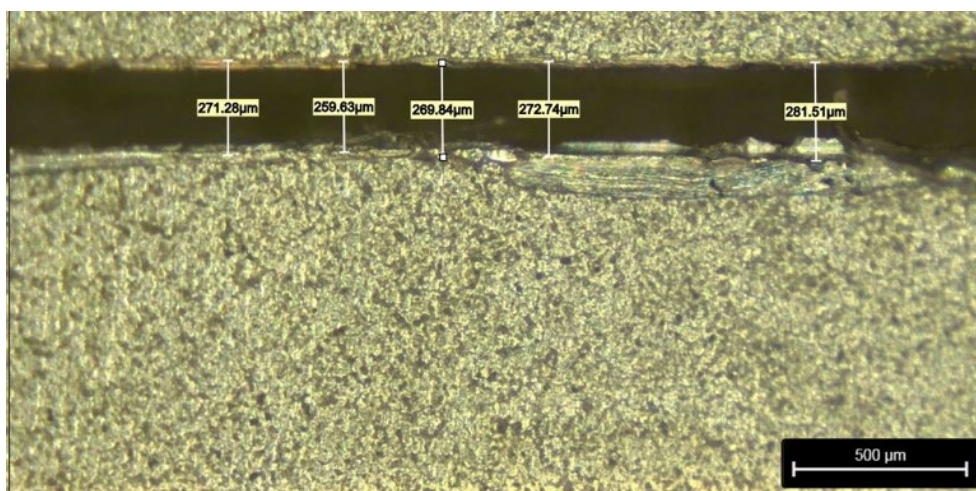


**Figure I-40. Microscope measurement of Test 1 Stage PD orifice width taken at various locations. The average Stage PD orifice width is  $0.265 \pm 0.015$  mm**

**Table I-17. Measurements for the Test 1 four purchased stages using a microscope (CFD) compared to the manufacturer's specifications.**

Impaction STAGE	Manufacturer specified orifice width [I-5], mm	Manufacturer specified orifice length [I-5], mm	Separation Distance to Orifice Width (S/W) [I-5]	Measured width, mm $\pm 0.015$ mm	Measured length, mm $\pm 0.015$ mm	Modeled S/W
Stage PA	0.90	19.0	2.10	1.022	20.070	1.85
Stage PB	0.50	21.0	3.78	0.510	20.070	3.69
Stage PC	0.36	19.0	5.25	0.397	20.245	4.76
Stage PD	0.14	25.0	13.50	0.265	20.295	7.13

Only half of the cascade sampler was modeled because the single-phase flow distribution is expected to be symmetric about the Y-Z ( $X=0$ ) plane, which divides the flow geometry into equal halves. The coupled solver was used to solve for the continuity and momentum equations without solving for the energy equation. Because these tests are conducted at room temperature at low Mach numbers, the energy equation was ignored. Air with constant material properties was used at atmospheric system pressure. The shear stress transport (SST)  $k-\omega$  model with an all  $y^+$  wall treatment was selected to model turbulence. Second-order numerics were used for spatial discretization for both the coupled and turbulence solvers. The flow in the domain switches between transitional turbulent to laminar flow. Tests with a transition turbulence model showed less than 2% change in the predicted stage and overall pressure drops, and produced a similar flow distribution, in comparison to the test without a transition model (base model). The flow remains turbulent for all inlet conditions. Therefore, it was decided that the base turbulence model was adequate.

The flow distribution tests were all performed for a steady-state condition. The velocity inlet boundary condition (BC) was used for the inlet boundary, and the outlet BC was used for the outlet boundary. The

no-slip BC was used for all walls, and the symmetry BC was used for the symmetry plane. A block-structured mesh was generated in STAR-CCM+ with a total mesh count of ~3.16 million. The block-structured (hex) mesh strategy was used to minimize computational cost and to adequately resolve the regions of interest. Four prism layers were used to capture the boundary layer, with the wall  $y^+$  less than one for the majority of the domain. The mesh settings listed in Table I-18 were used for the simulations.

**Table I-18. Mesh settings for the trimmer and surface remesher models.**

Meshing tool	Trimmer
Base size	5.0E-04 m
Surface growth rate	1.3
Number of prism layers	4.0
Prism layer thickness	4.5E-05 m
Stage-1 orifice	1.75E-04 m
Stage-2 orifice	1.5E-04 m
Stage-3 orifice	1.0E-04 m
Stage-4 orifice	5.0E-05 m
Total number of cells	3.17E+06

A mesh snapshot of the computational domain is shown in Figure I-41(a), and a close-up view of the refined mesh in the region of the orifices and the collectors is shown in Figure I-41(b). The mesh was refined in the orifice and collector regions because the solutions showed that the gradients of pressure and velocity are high in that region. Almost all of the pressure drop and flow acceleration occur as the flow enters the orifice. Similarly, the collector region is also important because it has a direct bearing on the

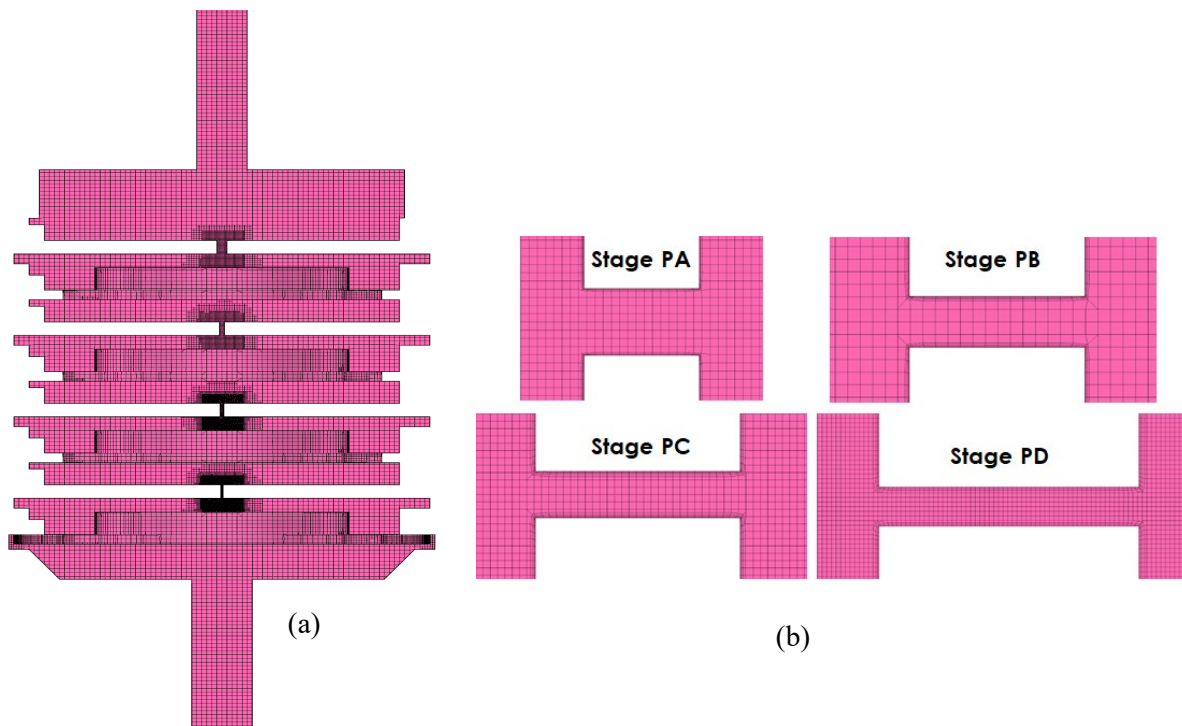


**Figure I-41. (a) Slice through the computational grid on the symmetry ( $x = 0$ ) plane; (b) close-up of the finely meshed orifice region for the 4 stages.**

particle collection dynamics. A mesh refinement study was conducted with the highest flow rate (9 LPM), by halving the base size in Table I-18. The mesh was shown to be converged, since the difference in predicted stage-wise and overall pressure drop between the two meshes was within 1%.

### I-6.2.1 Steady state simulations

All steady-state simulations were performed using 64 processors with a total runtime of approximately 1 day. The solution was deemed to be converged when residuals (continuity, momentum, and turbulence) dropped by approximately three orders of magnitude, starting from the initial conditions summarized in Table I-19.

**Table I-19. Initial conditions for the steady-state 4-stage cascade impactor simulation.**

Pressure	1 atm
Velocity	0 m/s
Turbulence velocity scale	1.0 m/s
Turbulence intensity	0.01
Turbulence viscosity ratio	10.0

Furthermore, negligible changes were obtained in the selected monitor points: velocity magnitude monitor points in the nozzles, pressure and turbulence intensity at the outlet boundary, and maximum  $y^+$  of all wall surfaces in the domain. Results of the 4-stage cascade impactor for an inlet flow rate of 9 LPM are shown in Figure I-42, Figure I-43, and Figure I-44.

The velocity contour plot in two Y-Z planes is provided in Figure I-42, and the corresponding streamline plot showing the flow distribution in the entire domain is provided in Figure I-43. Three observations can be made regarding flow results:

1. The flow accelerates as it enters the orifices and the majority of the pressure drop also occurs in this region.
2. The velocity magnitude in the remaining parts of the domain are negligible, and low-magnitude recirculation patterns can be seen in various parts of the domain, such as the inlet region before stage PA.
3. The flow through the orifice in stage PA has a sharp gradient in the X-direction (see Figure I-42(b)) because the flow exiting the inlet pipe section does not pass through a header. Furthermore, the flow exits the orifice with a similar velocity profile because of a short orifice flow development length. This has implications for the predicted particle depositions, as discussed in the next section.

Contours of (static) pressure are shown in Figure I-44 at two Y-Z planes. Significant pressure drop is shown to occur at the entrance of each of the orifices, with the maximum pressure drop observed for stage PD. A small rise in pressure is seen at the stagnation point. The predicted pressure drops from the simulation (CFD) across each of the 4-stages are compared to manufacturer-reported values [I-5] in Table I-20, where  $Re_w$  is the Reynolds number defined with respect to the orifice width and  $Re_{Dh}$  is the Reynolds number defined with respect to the hydraulic diameter of the orifice. The uncertainty of the predicted values is calculated using Eq. I-9.

The predicted average/area-averaged velocity and the manufacturer-listed values differ because the CFD model uses measured orifice dimensions, whereas the manufacturer's values are based on nominal orifice dimensions. The Reynolds number for the model, based on the orifice hydraulic diameter  $D_h$ , is also listed. It can be observed that the  $Re_{Dh}$  values spanning the laminar/transitional regime are fairly



consistent across the four orifices. The error between the manufacturer's specified pressure drops and the CFD-predicted pressure drops decrease from stage PA to stage PD. Given the sensitivity of the pressure drop to the orifice dimension, the differences could be due to manufacturing variability. Additionally, the manufacturer's measurements include measurement uncertainty [I-5]. In general, the model predicts a higher pressure drop for a given dynamic head when comparing the manufacturer's mean velocity ( $U_{avg}$ ) with the model-predicted mean velocity, where the mean is defined as

$$U_{avg} = \frac{\int \rho u(x, y, z) dA_c}{\rho dA_c}, \quad (I-9)$$

and  $\rho$  is the (constant) air density,  $A_c$  is the cross-sectional area of the orifice, and  $u$  is the local velocity magnitude. The pressure drop was also measured for the 7-stage cascade impactor at inlet flow rates of 6 and 7 LPM, as described in Section I-6.1.1, and the measured values are compared with those predicted by the model in Table I-20.

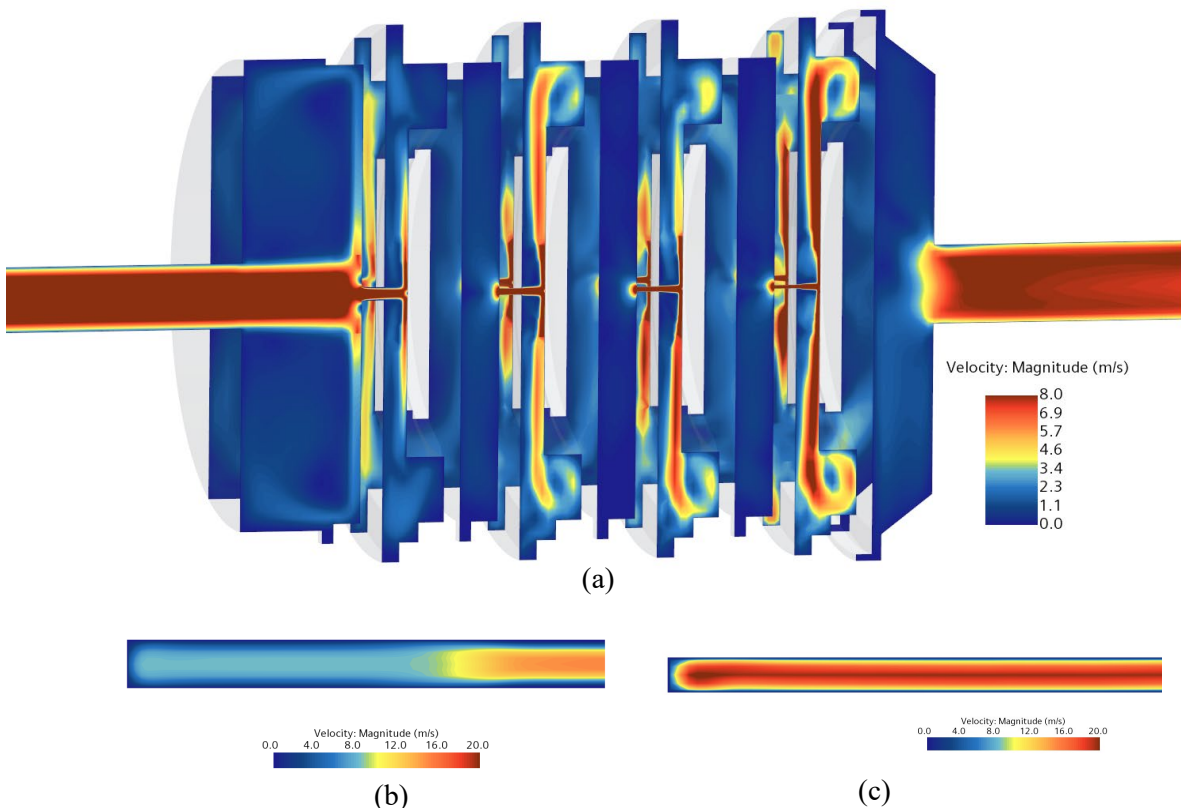


**Figure I-42. (a) Contours of velocity magnitude (9 LPM) on  $x = 0$  plane and  $x = -8$  mm plane, (b) velocity magnitude contour ( $y=0$ ) at a midplane on the orifice stage PA, (c) Velocity magnitude contour ( $y=0$ ) at a midplane on the orifice stage PB.**

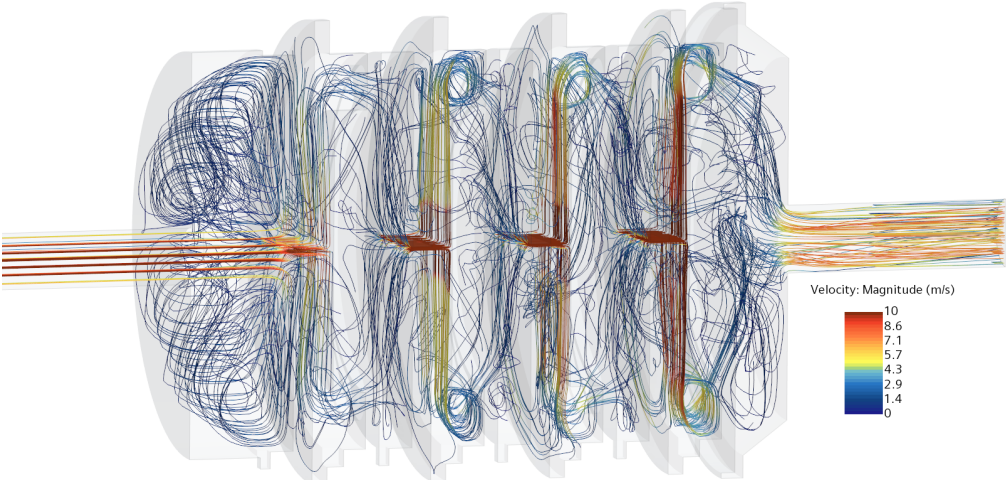


**Figure I-43. Streamline plot of the flow distribution through the 4-stage cascade impactor colored according to velocity magnitude (9 LPM).**

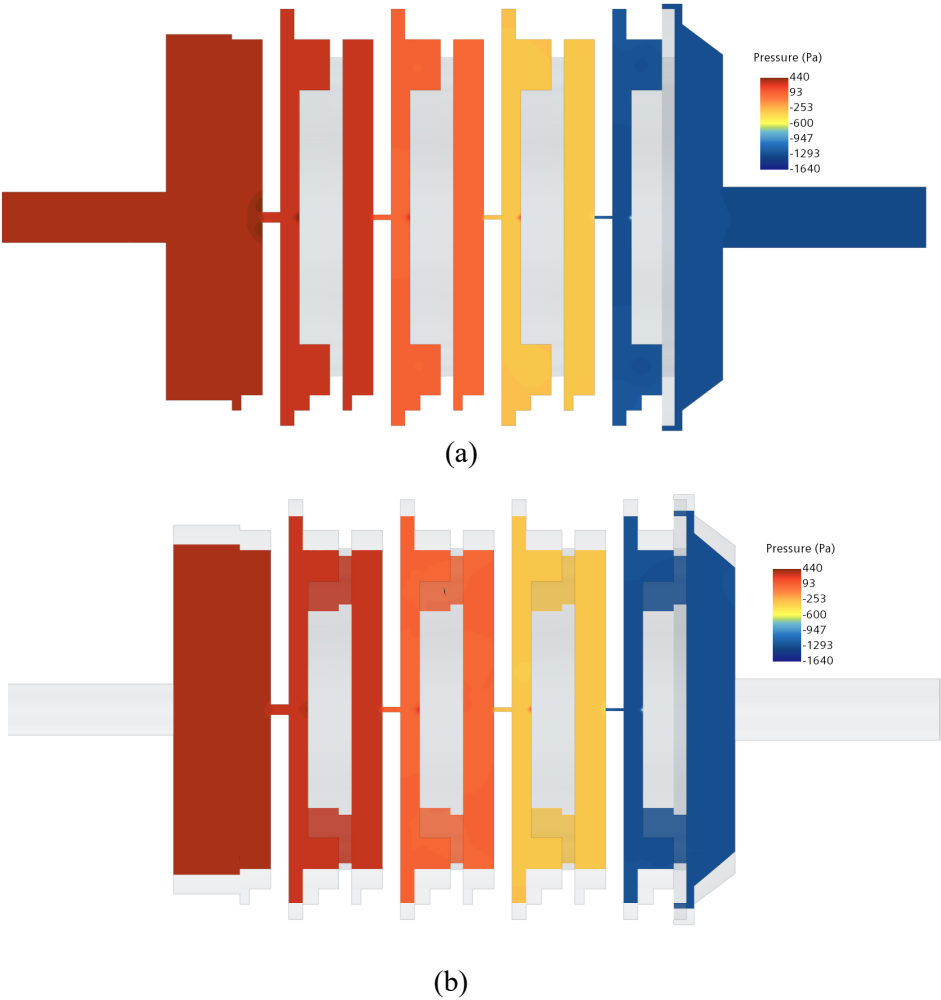


**Figure I-44. Pressure contours (9 LPM) on (a)  $x = 0$  plane and (b)  $x = -8$  mm plane.**

**Table I-20. Comparison of model predictions and manufacturer's specifications for the 4-stage cascade impactor at 9 LPM.**

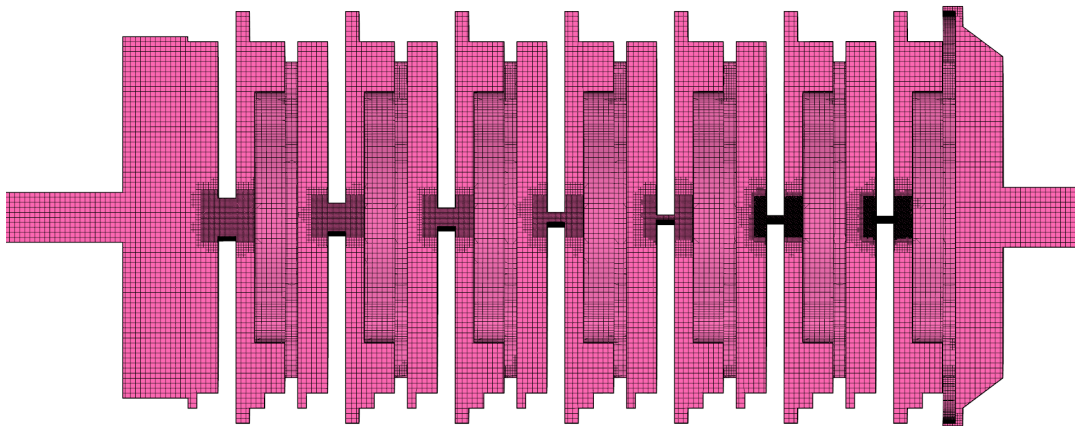
Impaction stage	Manufacturer's specification [I-5]			CFD-predicted			
	$U_{avg}$ , m/s	$Re_w$	$\Delta P$ , Pa	$U_{avg}$ , m/s	$Re_w$	$Re_{Dh}$	$\Delta P$ , Pa
Stage PA	8.77	473.7	75	7.47	487.0	956.0	$42 \pm 1$
Stage PB	14.29	428.6	149	14.67	477.5	960.5	$249 \pm 15$
Stage PC	26.32	473.7	373	18.70	473.9	929.7	$408 \pm 29$
Stage PD	42.86	360.0	971	27.92	472.3	932.4	$947 \pm 100$

The geometric parameters used to model the 7-stage cascade impactor, which includes three additional machined stages (MA, MB, MC), are listed in Table I-21.

**Table I-21. Geometric parameters modeled in the 7-stage cascade impactor.**

Impaction stage	Orifice width mm $\pm$ 0.015 mm	Orifice length, mm $\pm$ 0.015 mm	S/W
Stage MA	3.87	19.525	0.49
Stage MB	2.883	19.190	0.66
Stage MC	1.923	19.385	0.98
Stage PA	1.022	20.070	1.85
Stage PB	0.51	20.070	3.69
Stage PC	0.397	20.245	4.76
Stage PD	0.265	20.295	7.13

As in the 4-stage impactor model, symmetry was used, and only one-half of the geometry was modeled, because the flow distribution is expected to be symmetric about the Y-Z plane. The BCs and solver models chosen for this study were similar to those used in the 4-stage impactor simulation, with the coupled solver used for the continuity and momentum equations, and the SST k- $\omega$  model used for turbulence. A block structured mesh was generated in STAR-CCM+, with a total mesh count of  $\sim 3.87$  million. A mesh snapshot of the 7-stage impactor model is shown in Figure I-45.

**Figure I-45. Slice through the computational grid on the symmetry ( $x = 0$ ) plane for the 7-stage cascade impactor model.**



All simulations for the 7-stage cascade were performed using 64 processors, with a total runtime of approximately 1 day. Convergence criteria similar to those used for 4-stage impactor model were used for the current model. The results of the 7-stage cascade impactor for an inlet flow rate of 7 LPM are shown in Figure I-46 through Figure I-49. The velocity contour plot in two Y-Z planes are shown in Figure I-46, the velocity magnitude in the seven orifices about a X-Z mid-plane is shown in Figure I-47, and a streamline plot showing the flow distribution in the entire domain is shown in Figure I-48. Similar conclusions can be drawn for the 7-stage impactor and the 4-stage impactor. The core peaked velocity profile is more pronounced for the flow in the orifice of stage MA. Unlike with the 4-stage impactor study, the flow in stage PA in the 7-stage impactor study is similar to the flow distribution in the downstream orifices, because the flow entering the orifice of stage PA is well distributed, unlike in the 4-stage cascade. The pressure contour at two Y-Z planes is shown in Figure I-49. As in the 4-stage impactor study, significant pressure drops are observed in the orifice inlets. Relatively negligible pressure drops

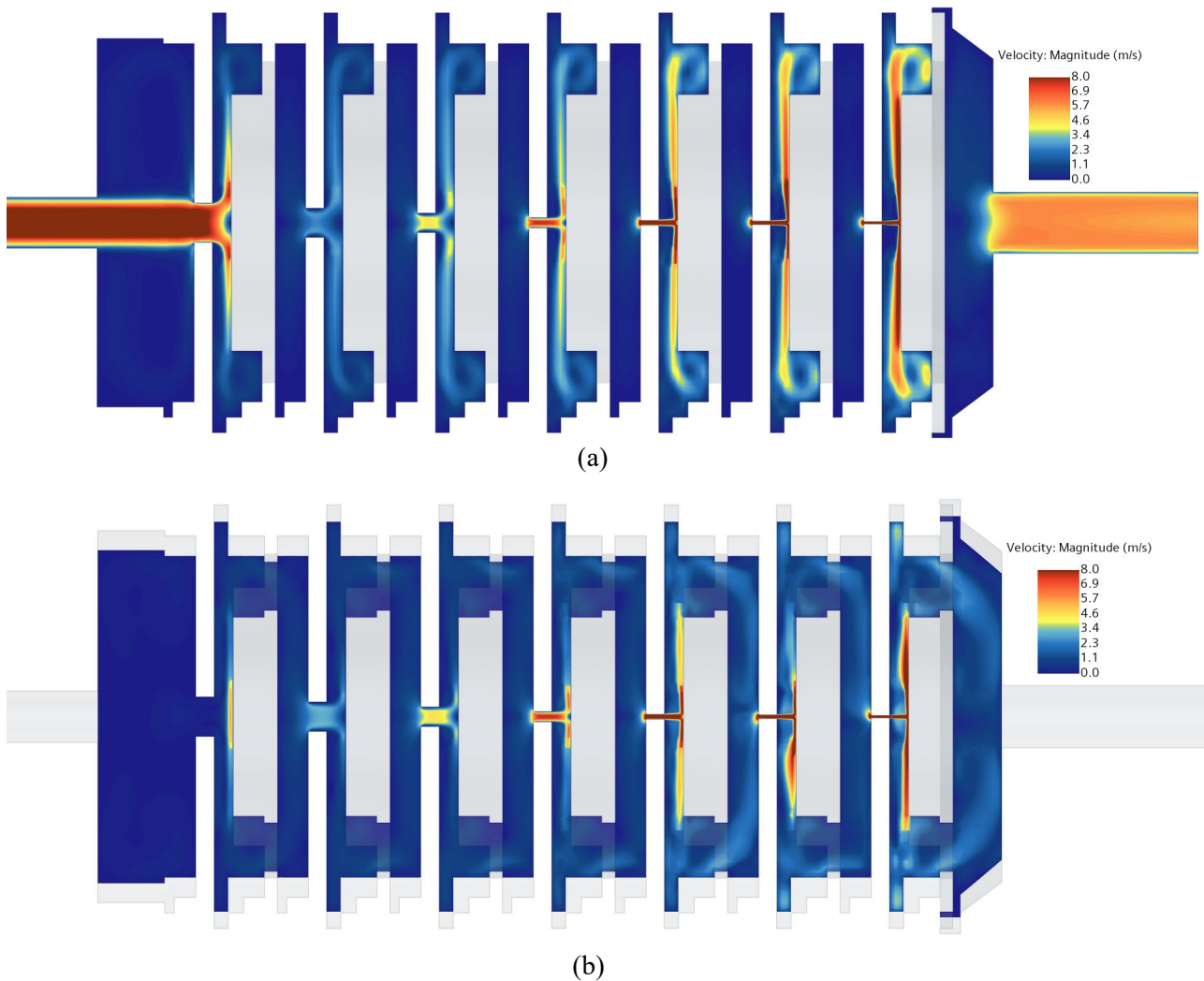


**Figure I-46. Contours of velocity magnitude (7 LPM) for the 7-stage cascade impactor on (a)  $x = 0$  plane and (b)  $x = -8$  mm plane.**

were observed at the orifice entrance for the three added stages, and the average flow velocities were lower in comparison to stages PA-PD.

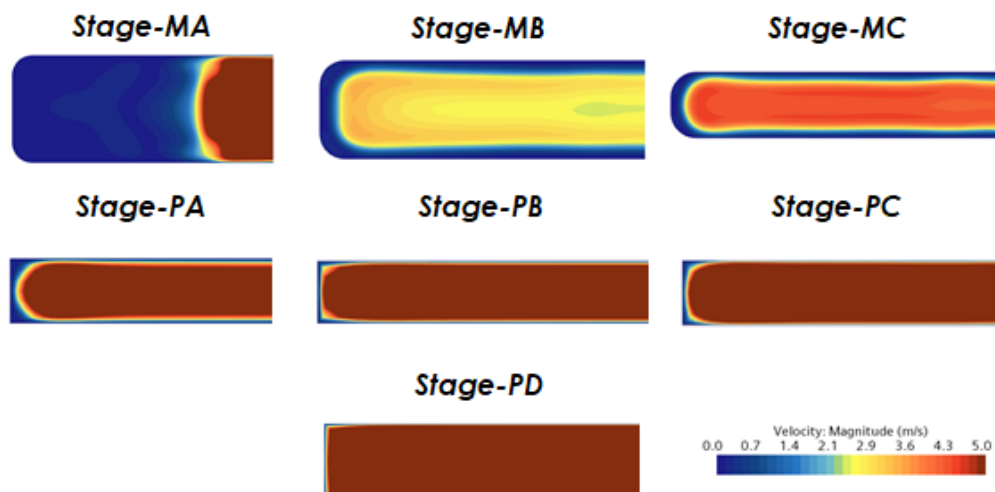


Figure I-47. Orifice velocity magnitude contour ( $y=0$ ) at the midplane (half of the orifices are shown) for the 7-stage cascade impactor at 7 LPM.

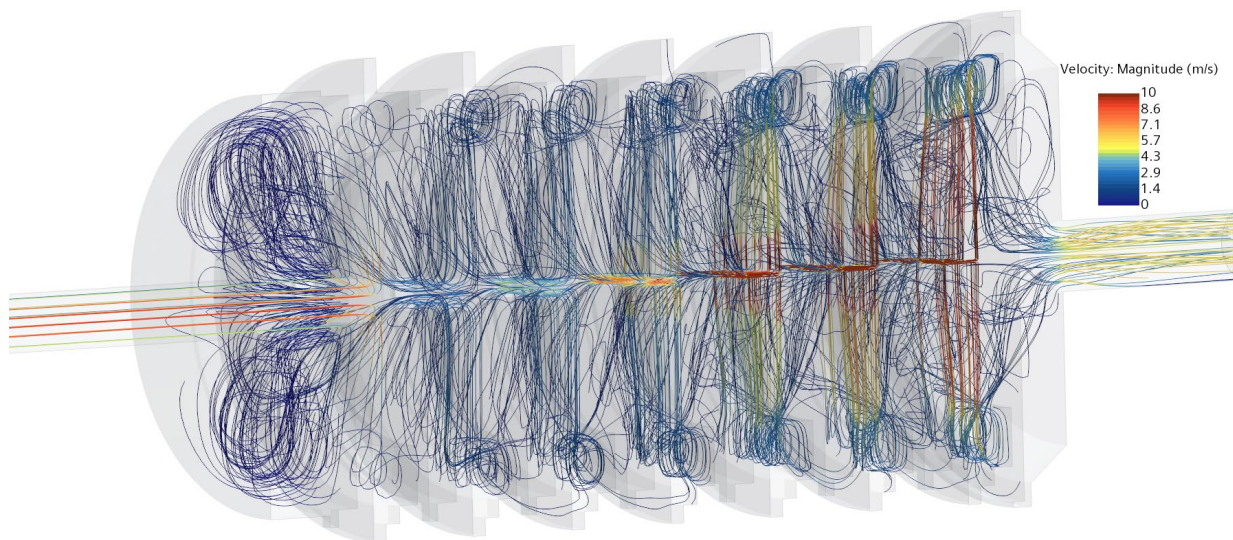
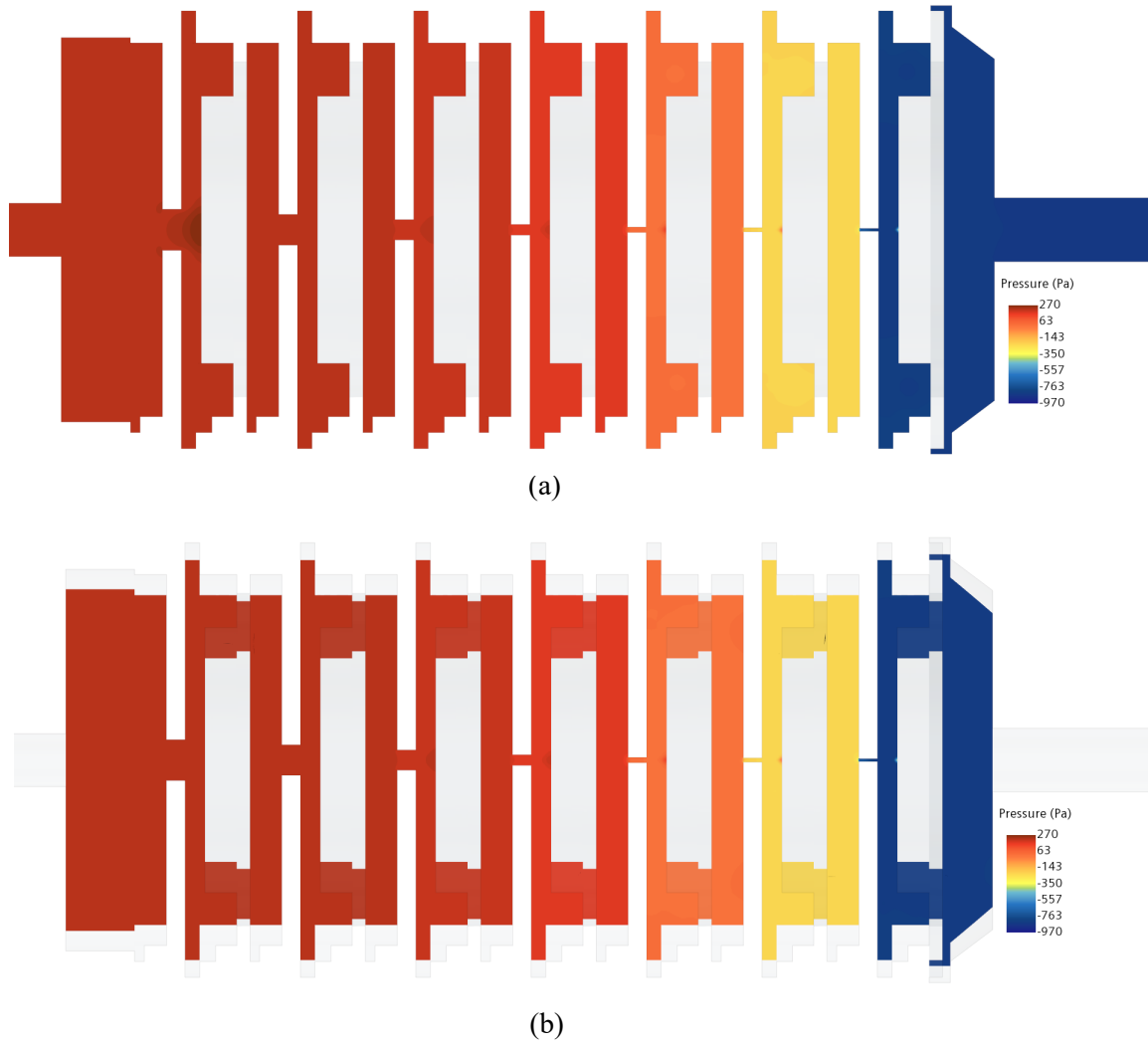


Figure I-48. Streamline plot of the flow distribution through the 7-stage cascade impactor, colored according to velocity magnitude (7 LPM).



**Figure I-49. Pressure contours (7 LPM) for the 7-stage cascade impactor on (a)  $x = 0$  plane and (b)  $x = -8$  mm plane.**

A comparison of predicted and measured stage and overall pressure drops is summarized in Table I-22 for a flow rate of 7 LPM and in Table I-23 for 6 LPM. The Reynolds numbers based on  $D_h$ , only show a modest increase from stage MA to stage PD, which is similar to the results using the 4-stage impactor, albeit for an inlet flow rate of 9 LPM. For both flow rates simulated, the relative error for stages PB–PD are less than 20%, which is considered acceptable given the measurement and model uncertainties. The model uncertainties are determined by calculating the discharge coefficient,  $C_d$ , for each orifice based on mean orifice dimensions:

$$C_d = \frac{\rho U_{avg}^2}{2\Delta P}, \quad (I-9)$$

where  $\rho$  is air density (1.18415 kg/m<sup>3</sup>) and  $\Delta P$  is the stage pressure drop. Assuming the discharge coefficients are the same for small deviations in orifice dimensions, the range of pressure drops is then calculated, accounting for the uncertainties in orifice length and orifice width. The model uncertainty is expected to be higher if all uncertainties are taken into account. Nonetheless, the overall pressure drop comparisons for both flow rates are excellent, and the model can be considered validated.

**Table I-22. Comparison of modeled vs. experimental pressure drop values and model flow parameters for the 7-stage cascade impactor for 7 LPM.**

Impaction stage	Simulation				Measured	
	$U_{avg}$ , m/s	$Re_w$	$Re_{Dh}$	$\Delta P$ , Pa	$\Delta P$ , Pa	Absolute relative error %
Stage MA	1.69	418.2	693.5	0	0	-
Stage MB	2.20	404.1	696.0	7	0	-
Stage MC	3.24	398.1	714.5	12	$30 \pm 30$	-
Stage PA	5.58	363.7	714.0	$34 \pm 1$	$62 \pm 30$	45
Stage PB	11.13	362.4	729.0	$150 \pm 9$	$128 \pm 30$	17
Stage PC	14.62	370.6	726.9	$258 \pm 20$	$220 \pm 30$	17
Stage PD	21.79	368.6	727.8	$603 \pm 68$	$675 \pm 30$	11
Overall	-	-	-	1116	1156	3.5

**Table I-23. Comparison of model vs. experimental pressure drop values and model flow parameters for the 7-stage cascade impactor for 6 LPM.**

Impaction stage	Simulation				Measured	
	$U_{avg}$ , m/s	$Re_w$	$Re_{Dh}$	$\Delta P$ , Pa	$\Delta P$ , Pa	Absolute relative error %
Stage MA	1.43	352.9	585.2	0	0	-
Stage MB	1.90	349.6	602.2	5	0	-
Stage MC	2.82	345.7	620.5	9	$18 \pm 30$	-
Stage PA	4.86	317.2	622.6	$26 \pm 1$	$25 \pm 30$	5
Stage PB	9.73	316.7	637.2	$117 \pm 7$	$99 \pm 30$	18
Stage PC	12.76	323.5	634.5	$201 \pm 15$	$178 \pm 30$	13
Stage PD	18.93	320.2	632.1	$470 \pm 50$	$481 \pm 30$	2
Overall	-	-	-	869	867	0.2

### I-6.2.2 Particle Deposition Simulations

The Lagrangian modeling approach was used to investigate particle deposition on the collection plates.. The purpose of this study was to broadly capture a distribution of aerosol-sized particles and determine the mean cut point for each stage in the cascade. In the current study, solid  $\text{UO}_2$  particles with a density of 10.97 g/cc are used. Note that all particle diameters cited within the CFD simulations are physical diameters, not to be confused with the AED specified in the cascade cut points. In the Lagrangian framework, particles are treated as parcels of mass, and applicable conservation laws are used. Lagrangian models are recommended for particle-laden flows in which the volume fraction of particles is low (less than 10%) compared with the finite-volume cell. In the Lagrangian approach in STAR-CCM+ [I-20], the equation of conservation of (linear) momentum for a material particle of mass  $m_p$  is given by

$$m_p \frac{dv_p}{dt} = \mathbf{F}_s + \mathbf{F}_b, \quad (\text{I-10})$$

where  $v_p$  denotes the instantaneous particle velocity,  $F_s$  is the result of the surface forces, and  $F_b$  is the result of the body forces. In the Lagrangian framework, the state is evolved on a particle-by-particle basis, whereas the Eulerian fields are frozen. The particle position and particle velocity are obtained by numerically integrating the position/displacement equation with time:

$$m_p \frac{dr_p}{dt} = v_p, \quad (\text{I-11})$$

where  $r_p(t)$  is the instantaneous position vector at time,  $t$ . In the statistical Lagrangian approach, parcels of particles are tracked. For large particle loadings, the parcel approach can be used to save computational cost, so it is the method of choice here. A single integration of the state is applied to all particles in the parcel, and the interaction term with the Eulerian phase is calculated by multiplying by the number of particles in the parcel. For statistically converged results, it is recommended to have sufficient number of computational parcels. The surface forces can be broken down as follows:

$$\mathbf{F}_s = \mathbf{F}_d + \mathbf{F}_p + \mathbf{F}_{vm}, \quad (\text{I-12})$$

where  $F_d$  is the drag force,  $F_p$  is the pressure gradient force, and  $F_{vm}$  is the virtual mass force. The result of the surface forces is the momentum that is transferred from the continuous phase to the particle. The body force term can be similarly decomposed as follows:

$$\mathbf{F}_b = \mathbf{F}_g + \mathbf{F}_u + \mathbf{F}_{MRF} + \mathbf{F}_{Co}, \quad (\text{I-13})$$

where  $F_g$  is the gravity force,  $F_u$  is the user-defined body force term,  $F_{MRF}$  is applicable for moving reference frames, and  $F_{Co}$  is the Coulomb force. In the current study,  $F_g$  is the only applicable body force. There are various submodels for particle interaction forces, and these are described in detail in the Star-CCM+ user manual [I-20]. In the current study, the following surface force models were selected: the virtual mass force, the pressure gradient force, the Schiller-Naumann drag force model, and the Sommerfeld shear lift force model [I-20].

To complete the Lagrangian model setup, particle injectors and particle-wall interactions must be defined. For the current study, the part injector is used with the injector properties described in Table I-24. The part injector uses the injection faces from the meshed part; that is, the inlet face. The number of injection points in the inlet face is controlled by the point inclusion probability. The total number of injection faces for the current setup was approximately 300. The number of particles per parcel (parcel streams) was

taken to be 100. The particles were injected with the same velocity as the fluid—zero slip velocity—which is a reasonable assumption that the particle movements are only driven by the pump flow. The particle flow rate was controlled by the number of injection points and parcel streams ( $300 \times 100$  per timestep). Therefore, while the specified particle flow rate was arbitrary, the total number of injections was set to inject approximately 0.5 million particles ( $\sim 5e3$  parcels) in the computational domain. The time during which the injections occurred was controlled. The total number of injected particles in the system was selected arbitrarily, with consideration for the computational time required to ensure that the majority of the particles were collected in the collectors. A few particles escaped from the computational domain.

**Table I-24. Part injector parameters.**

Parameters	Values
Physical particle diameter distribution	Log-normal distribution with a range of $[0.1, 10] \mu\text{m}$ and a mean of $3 \mu\text{m}$ ( $10 \mu\text{m}$ AED)
Point inclusion probability	0.1
Parcel streams	100
Velocity	Same as fluid velocity

Four options are available in STAR-CCM+ to model particle-wall interactions: rebound, sticky, escape, and composite. In the rebound mode, particles rebound off the wall's surface and are solved using user-specified normal and tangential restitution coefficients. The sticky surface BC is the exact opposite, with particles sufficiently close to the wall sticking to the surface. The escape mode, which is not applicable for the current study, allows for the particles to escape from the boundary. The composite mode allows for a user-defined probability of the rebound, sticky, and escape modes. In the current study, all collector surfaces were defined as sticky surfaces, whereas the other wall surfaces were defined as rebound surfaces. A parameter is available in STAR-CCM+ which defines the degree to which particles stick. For this study, the particles are considered to stick if the coefficient is  $\geq 0.8$ , with 1.0 defined as being completely stuck onto the surface. The locations of the part injector and the sticky boundary surfaces are highlighted in Figure I-50.

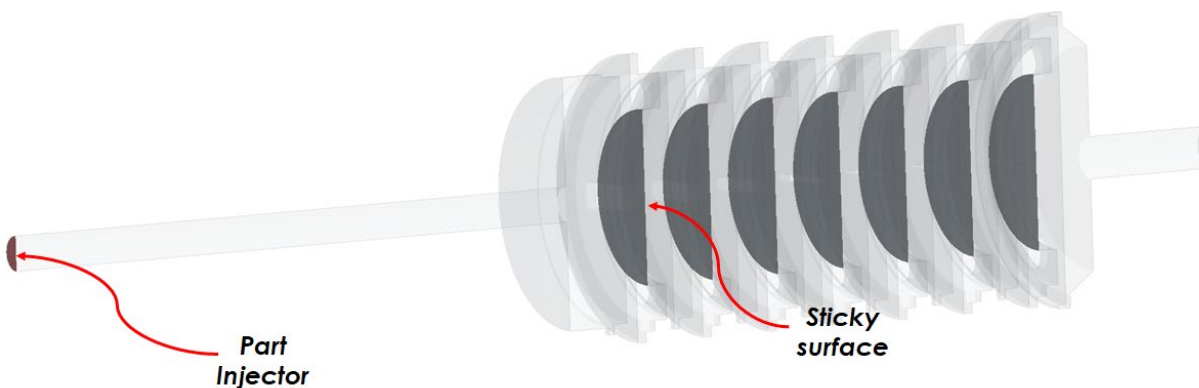


**Figure I-50. Isometric view of the 7-stage cascade impactor with the (inlet) injection surface and collector surfaces highlighted.**

The solution was obtained in two steps: first, the steady-state distribution for the 7-stage impactor for a flow rate of 7 LPM was obtained, and then a transient fluid solve was performed using the steady-state



distribution as the initial condition. Once the statistically converged results were obtained, the fluid solver was frozen, and the Lagrangian solver was turned on to solve for particle deposition. The transient fluid solve was conducted with a Courant number of 5. Although this might dampen physical fluctuations, a lower Courant number would be computationally expensive as a result of the much smaller time step required. For the current study, the timestep size is chosen to be  $1e-4$  s using a second-order implicit scheme. This approach was chosen to ensure a 1:1 timestep with the Lagrangian solver if a two-way coupling approach were required. A larger particle solver timestep resulted in poor convergence. For the Lagrangian particle solver, a second-order implicit unsteady tracking method was used with the maximum substeps capped at  $1e+4$  s. This ensured that the small number of parcels that had difficulty converging the particle solve were not tracked for a long time.

In the current study, all parcels converged for every time step. The particle solution was run for a physical timestep of 2 s. Although this might be insufficient to replicate the full implementation of the test method in the hot cell (estimated maximum event plus particle settling,  $\sim 300$  s), the purpose of this study was to broadly capture the distribution of particles and the mean cut point for each stage. The simulation time was  $\sim 2$  days running on 64 processors. Particle injection occurred within the first 100 timesteps ( $\Delta t = 1e-4$ ), after which the injector was shut down. The final physical particle size distribution in the domain is shown as a histogram in Figure I-51. The final particle distribution is expected to follow a log-normal distribution, as defined in the injector, with only a tiny fraction of all injected particles ( $\sim 0.58\%$ ) having exited from the flow domain during the course of the simulation.

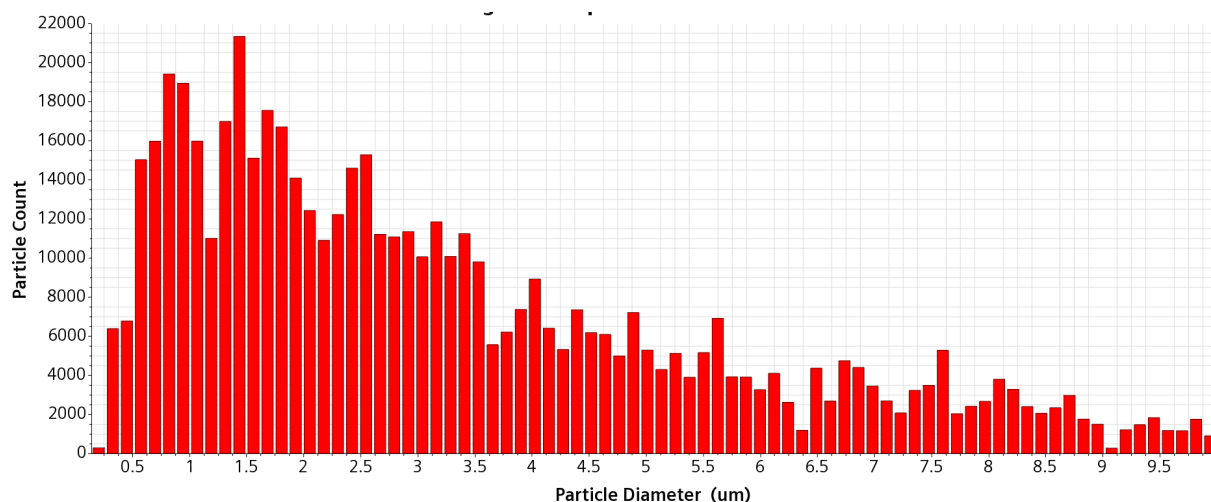


**Figure I-51. Physical particle size distribution histogram in the flow domain using the log normal distribution for the injector with size range  $\in [0.1, 10]$   $\mu\text{m}$  and mean of  $3 \mu\text{m}$ .**

A snapshot of the particle distribution at the end of the simulation is shown in **Figure I-52** and **Figure I-53**, with particles of different sizes scaled to a fixed pixel size. After 2.5 seconds,  $\sim 95\%$  of the total particles were collected in the seven stages, and particle distributions were analyzed. These distributions of particles within the impinging jet area created by the orifice above are very similar to the distributions observed in physical testing; however, physical testing did not observe the large number of particles distributed on the plate at other locations.

Three observations can be made regarding the particle distribution:

1. At a flow rate of 7 LPM, the flow speeds in orifices PB-PD were high enough to force particles to collect in and around the stagnation zone.

2. Stages MB and MC did not trap a lot of particles and further investigation is needed to fully evaluate their performance.
3. Stage MA collected a lot of particles. This is primarily driven by the core peaked flow. Because the core peaked flow forced a high velocity jet near the center, this stage trapped particles much smaller than its designed (mean) cut point, unlike stage PD. This can be observed in the stage histogram distributions shown in Figure I-54.

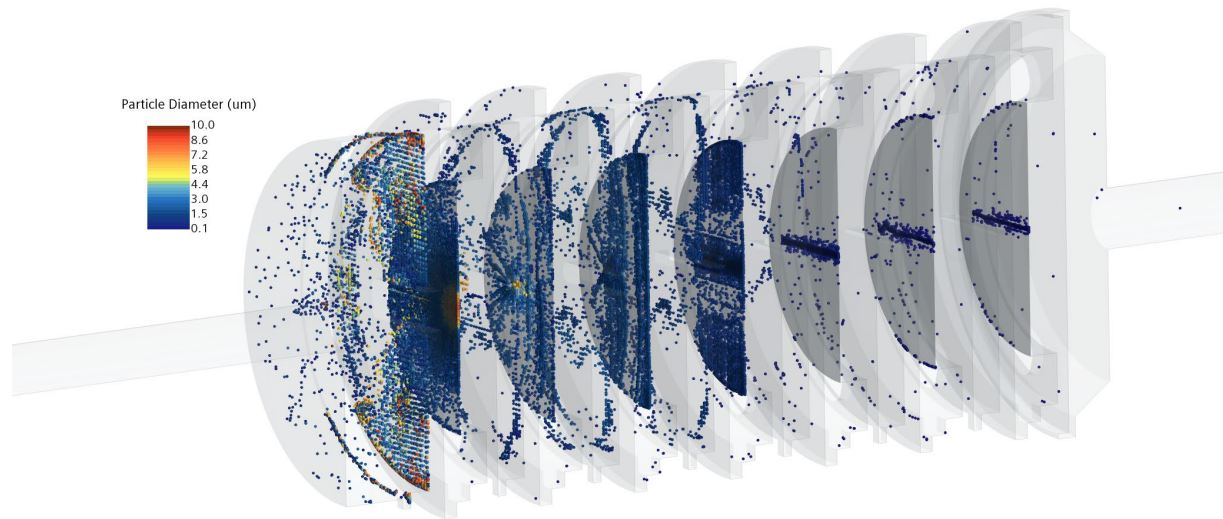


**Figure I-52. Isometric view of the 7-stage cascade impactor showing the particle distribution colored according to physical particle diameter ~2.5 s after injection (7 LPM).**

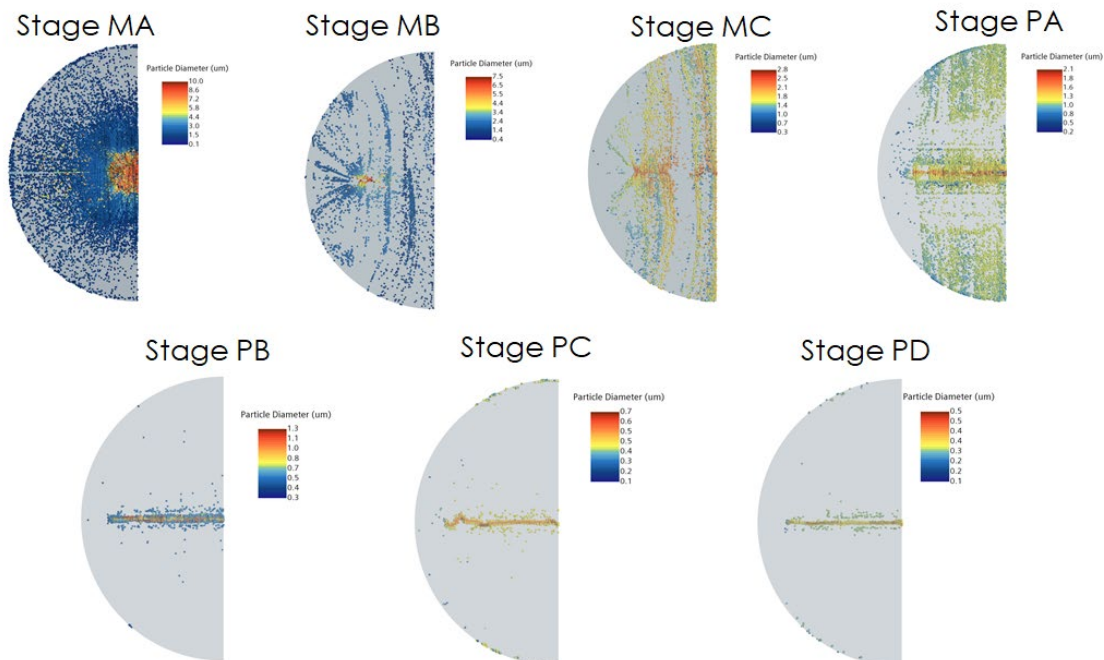


**Figure I-53. Particles collected on the 7 stages at ~ 2.5 s after injection of  $5.4 \times 10^5$  particles (7 LPM).**



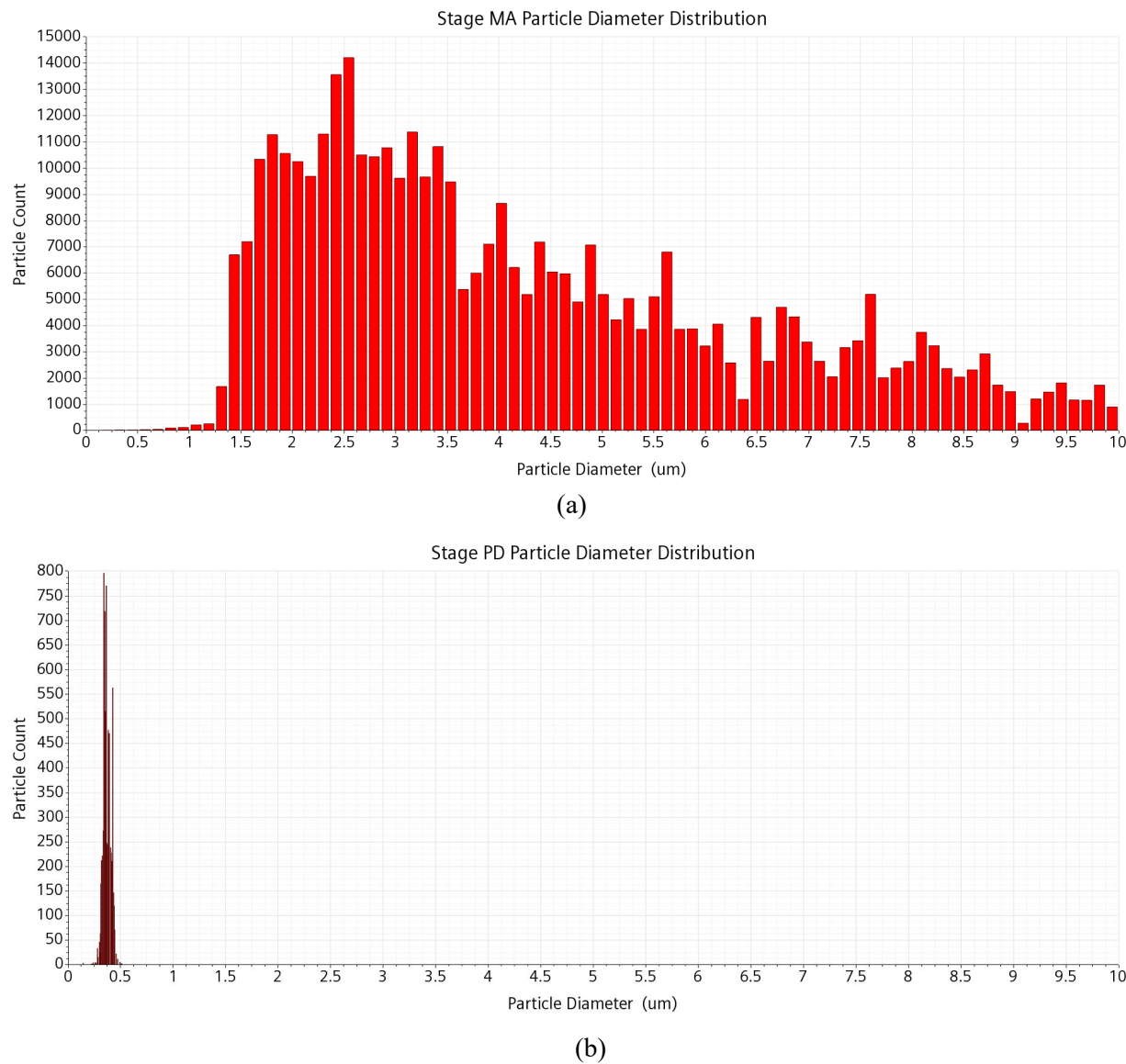


**Figure I-54. (a) Physical particle size distribution histogram of particles collected (7 LPM) in (a) stage MA and (b) stage PD.**

The percentages of particles collected across the seven stages for various ranges of physical particle diameters are shown in Table I-25. Whereas stages PA–PD show sharp cut points trapping particles between 0.1–1.5  $\mu\text{m}$ , stages MB–MC collect a relatively lower number of particles within the expected range, and stage MA shows a wider spread of particle sizes for reasons discussed above. The particle collection statistics are shown in

Table I-26, thus quantifying the stage cutoff diameters. The standard deviation is highest for stage MA because of a wider spread of particle sizes.

**Table I-25. Percentages of particles collected across various size groups for the 7 stages (7 LPM).**

Size distribution (μm)		Percentages						
Physical diameter, ρ=10.96 g/cc	AED	MA	MB	MC	PA	PB	PC	PD
0.1–0.25	0.33-0.83	11.8	0	0	0	0	35.3	52.9
0.25–0.5	0.83-1.66	0.2	0	0	0.1	0.3	27.2	72
0.5–0.75	1.66-2.48	0.2	0.1	0.1	0.5	69.2	29.9	0
0.75–1.0	2.48-3.31	0.6	0.3	0.1	4.9	94.1	0	0
1.0–1.5	3.31-4.97	15.2	0.9	3.2	68.4	12.3	0	0
1.5–2.0	4.97-6.62	67.3	2.2	10.1	20.4	0	0	0
2.0-2.5	6.62-8.28	93.6	2.2	4	0.1	0	0	0
2.5–3.0	8.28-9.93	97.9	1.7	0.4	0	0	0	0
>=3.0	>=9.93	99.7	0.3	0	0	0	0	0
Total number of particles collected	>=9.93	380,629	4,604	10,028	54,792	60,553	11,628	7,580

**Table I-26. Particle collection statistics for the 7-stages (7 LPM).**

Parameter	Stage MA	Stage MB	Stage MC	Stage PA	Stage PB	Stage PC	Stage PD
Physical mean (μm)	4.23	2.26	1.78	1.35	0.82	0.52	0.37
Physical median (μm)	3.65	2.03	1.79	1.34	0.82	0.52	0.36
Physical STD (μm)	2.15	0.84	0.31	0.22	0.14	0.05	0.04
<b>AED mean (μm)</b>	<b>14.01</b>	<b>7.49</b>	<b>5.90</b>	<b>4.47</b>	<b>2.72</b>	<b>1.72</b>	<b>1.23</b>
<b>AED median (μm)</b>	<b>12.09</b>	<b>6.72</b>	<b>5.93</b>	<b>4.44</b>	<b>2.72</b>	<b>1.72</b>	<b>1.19</b>
<b>AED STD (μm)</b>	<b>7.12</b>	<b>2.78</b>	<b>1.03</b>	<b>0.73</b>	<b>0.46</b>	<b>0.17</b>	<b>0.13</b>

Given the results of these simulations and the experimental observations, the added stages MA, MB, and MC are performing as expected but could be improved. As an alternative, a Marple cascade impactor has been procured, and testing of that design is underway, to be followed by corresponding simulations.

### I-6.2.3 Collection Enclosure Simulations

Simulations of the enclosure used during aerosol collections are also being completed to determine if a substantial number of aerosols could escape collection through the openings between the 4PB fixture and the test specimen. The initial model is shown in Figure I-56 for 7L/min, indicate that this is unlikely as the fluid streamlines do not show any circulation patterns in the box. Particle simulations are required to confirm this observation. This simulation will be continued in FY22. One area of improvement could be to eliminate any static charge attraction by constructing the enclosure from metal and grounding it.

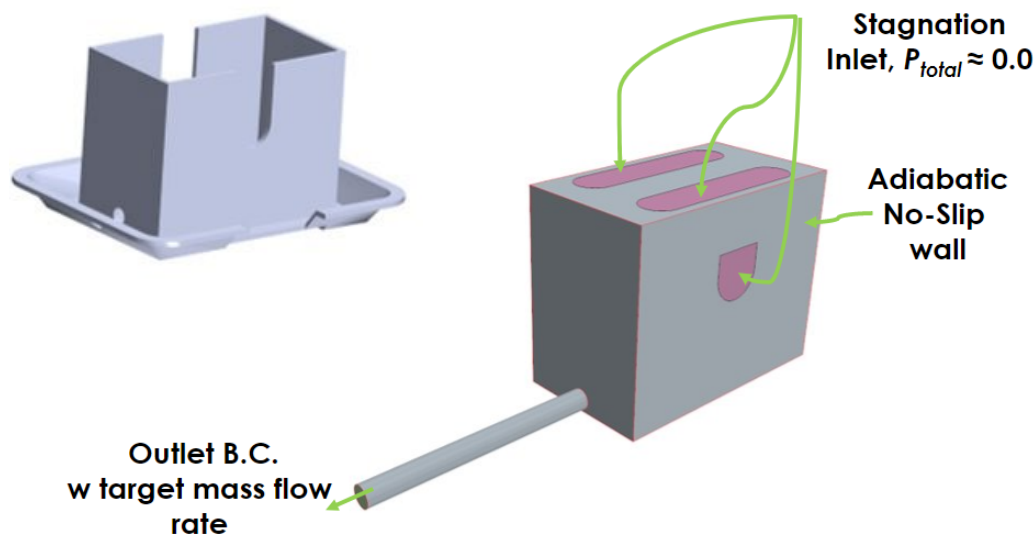


Figure I-56. CFD model of collection enclosure.

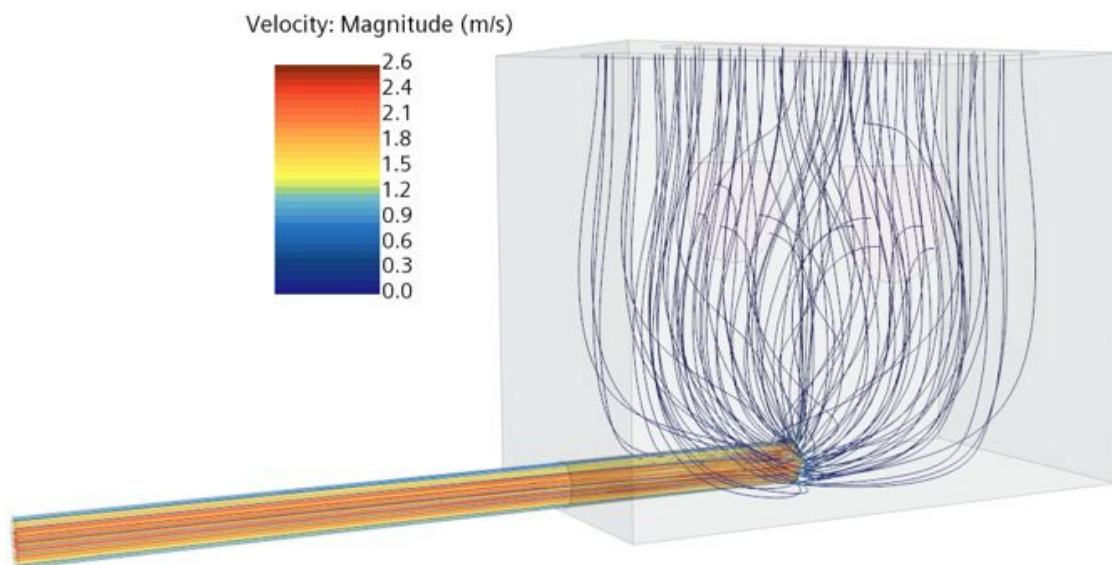


Figure I-55. Preliminary results from collection enclosure simulation indicating that there is no expected loss of particles through enclosure openings.

### I-6.3 Collection efficiency calculations

Both the ISO dust mixture particle collections and the CFD-predicted particle distributions were examined to calculate an expected efficiency for each stage of the as-designed cascade. The efficiency calculation provides an independent verification of the analytically-calculated cut-points when the test performed is representative of the field condition where the cascade impactor will be used. As discussed in Section I-1.4.2 and I-1.4.3, the ISO dust tests completed to date fall short in the size range and distribution of particles introduced to the sampler, and as expected, the efficiencies calculated for the ISO tests do not provide a good match for the analytical cut-points or the CFD-evaluated cut-points; these tests may be revisited in future. Ideally, SEM imaging of the collected aerosols from an actual test will be used to evaluate the size distribution of the deposited material.

#### I-6.3.1 ISO dust test evaluated stage collection efficiency

For the ISO mixture tests, the collection curves for the seven stages are shown in Figure I-57. The individual curves were generated using fixed bin sizes between 0 and 30  $\mu\text{m}$  AED. It was assumed that all particles downstream from the first stage were deposited on stage collection plates, with zero intra-stage wall losses. This was a good approximation, because most of the particle wall losses were observed to occur upstream from the first stage.

Using the ISO dust mixture tests and the data generated by SEM processing, the cut-points for the seven stages were derived from the distribution graphs and are presented in Table I-27, along with the analytical cut-points for the cascade used in the ISO dust tests. It is observed that PB, PC and PD collect most smaller particles between 0.1 – 1.5  $\mu\text{m}$  and the machined stages collect very few particles in this size range. It is also observed that MA has a wide range of collection.

**Table I-27 ISO dust AED cut-points – experimental vs. analytical, Eq. (I-6).**

Stage name	$d_{50}$ ISO dust tests ( $\mu\text{m}$ )	$d_{50}$ ( $\mu\text{m}$ ) analytical <sup>a</sup>
Stage MA	8.43	15.64
Stage MB	6.43	11.53
Stage MC	5.18	7.70
Stage PA	5.18	4.13
Stage PB	3.43	2.02
Stage PC	1.18	1.57
Stage PD	1.43	1.02

<sup>a</sup> Each as-built cascade orifice is slightly different in dimension within the manufacturing tolerances from others of the same nominal cut-point; therefore, each assembled cascade has slightly differing analytical cut-points.

As seen from Table I-27, the experimentally obtained particle cut-points using the ISO dust mixture are significantly lower than the analytical cut-point values that the stages were designed to collect for MA, MB, and MC, whereas stages PA, PB, PC and PD ISO dust measured cut-points are slightly higher than the analytical value. This can be understood as a result of one of two reasons:

1. The concentration of the ISO dust powder used in the experimental studies contained a lower mean diameter of particles than what is ideal with respect to the cut-points of the modified cascade, meaning that the dust did not include a very many particles with diameters in the range of MA, MB, and MC. This resulted in a low flux of larger sized particles for collection in MA, MB, MC, and it caused the distribution to be skewed towards a smaller cut point.

2. Image processing of the collected material (as discussed in Section I-6.1.3) is limited to only a few locations on the deposit and only those particles visible on the top surface of the pile of dust.

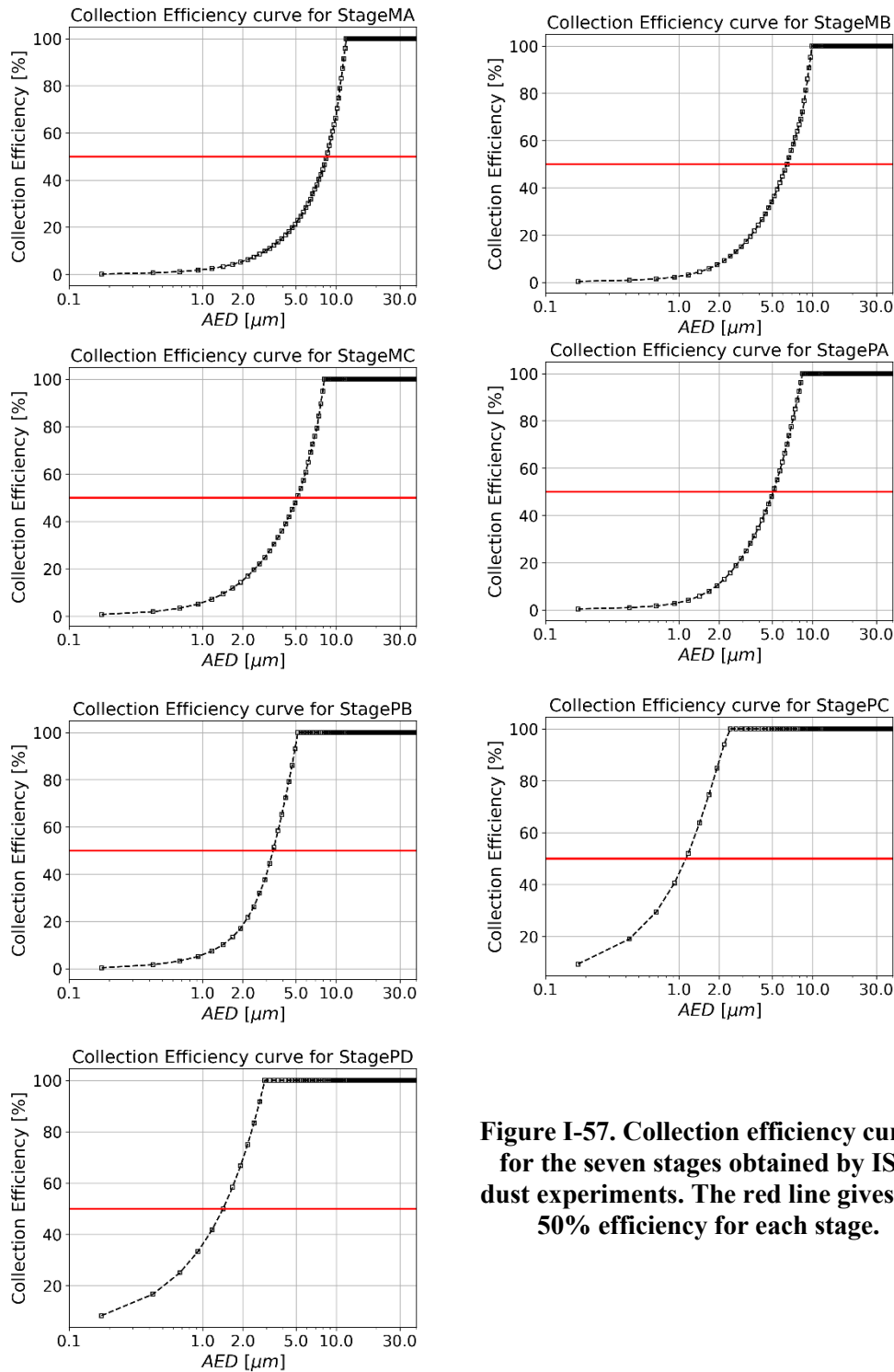


**Figure I-57. Collection efficiency curves for the seven stages obtained by ISO dust experiments. The red line gives the 50% efficiency for each stage.**

Because the cut-points measured with the ISO dust and image processing technique are so far from the intended stage cut-points, the test will be repeated in FY23 with a wider particle size distribution and including a larger number of image processing locations on the collection filter with more refined image

analysis models, with the goal of better understanding the minimum number of image processing locations required to generate the best possible characterization of the collected material.

### **I-6.3.2 CFD evaluated stage collection efficiency**

Collection efficiency curves were also generated from Lagrangian particle solver simulations using STAR-CCM+, as shown in Figure I-58. A comparison of the cut-points from the CFD results ( $d_{50}$  from collection curves) with the analytical correlation—calculated using Eq. (I-6)—yields an absolute mean error of ~19.7%, as shown in Figure I-59. The CFD-predicted cut-points compare well with the analytical predictions, with the exception of stage MA. Unlike other stages, MA's CFD-predicted cut-point showed considerable variation in particle sizes, and further investigation is needed to verify the collection efficiency of that particular stage of the impactor. It can be generally concluded that the added stages MA, MB, and MC by and large trap the larger sized particles, but they could be improved to obtain sharper cut-point distributions if desired. The cut-points predicted for the purchased stages are higher than those experimentally determined by the manufacturer [9] but are consistent with the as-fabricated orifice dimensions, as discussed in Section 0.

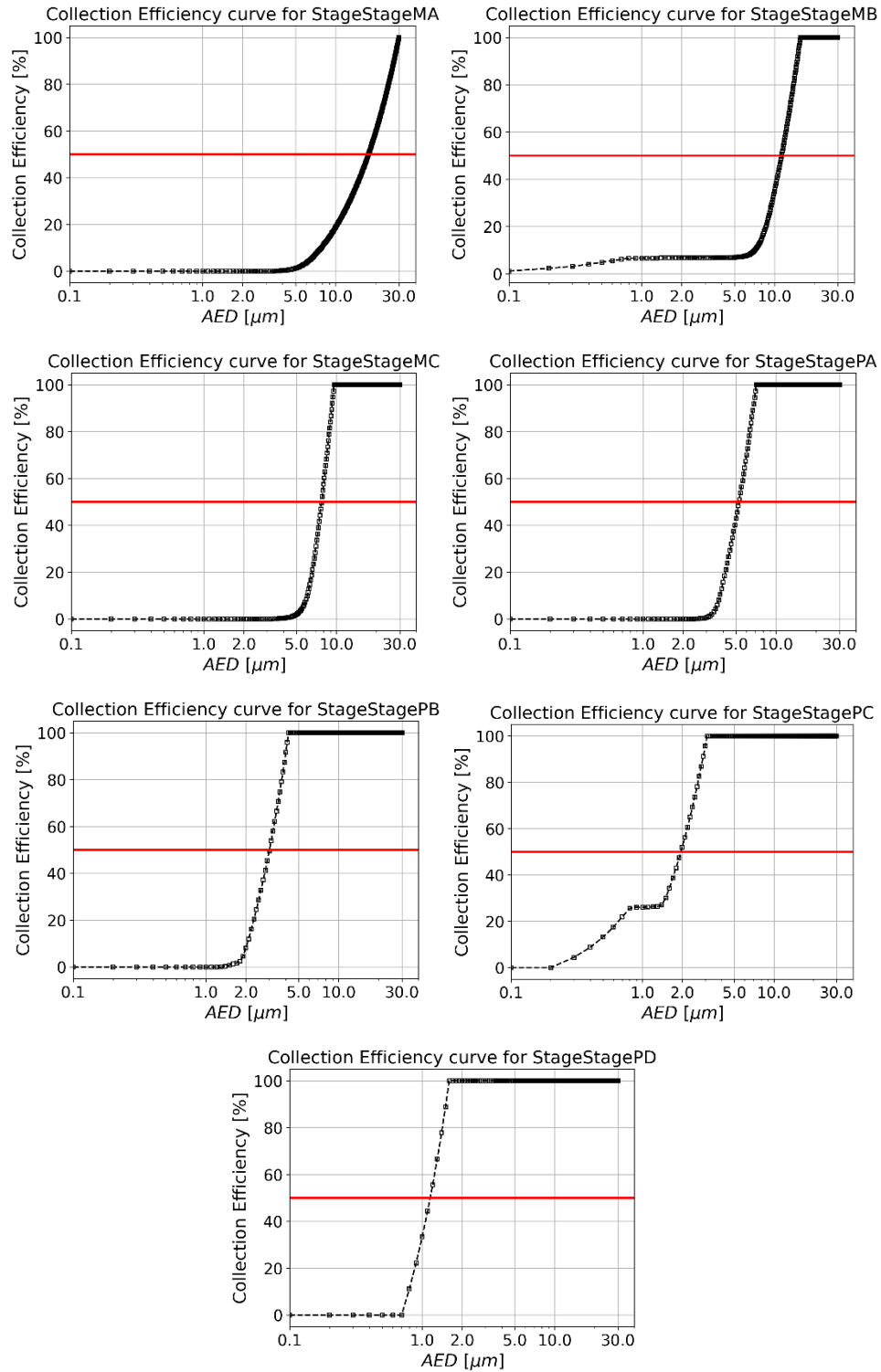


Figure I-58. CFD-predicted collection efficiency curves for the seven stages.

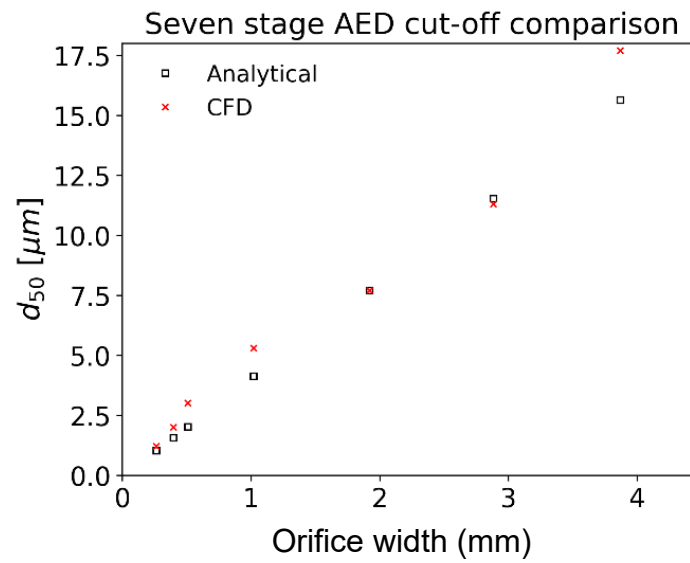


Figure I-59. Comparison of stage cut points (AED) obtained by CFD and the analytical correlation.



## I-7 Ongoing and Future Work

Table I-28 provides a summary of the planned tests for aerosol collection. To allow tests of pressurized segments, a pressurization fixture and protocol for the SNF segments has been designed and is now being tested out of cell. To collect the aerosols released during fatigue fractures, a collection enclosure is being designed for the CIRFT machine.

**Table I-28. List of specimens tested in 4PB where aerosols are planned to be collected.**

Specimen ID	Cladding alloy	Test temp. (°C)	Specimen heat treatment before test	In-reactor operating zone	Specimen average burnup (GWd/MTU)	Specimen average oxide thickness (μ)
30AD05-1003-1156	M5	RT	None	zone1	60	3
30AE14-1800-1953	M5	RT	FHT	zone1	60	9
3D8E14-2810-2963 <sup>a</sup>	ZIRLO	RT	None	zone1	63	41
3F9N05-2882-3035	ZIRLO	RT	FHT	zone1	58	46
3A1F05-2402-2555 <sup>b</sup>	LT Zirc-4	RT	None	zone1	55	117
F35P17-2402-2555	Zirc-4	RT	FHT	zone1	52	117

FHT = full-length fuel rod heat treatment

<sup>a</sup> Test complete

<sup>b</sup> Collection complete, analyses pending.

### I-7.1 Potential use of Marple cascade

In FY22, ORNL worked with a Marple cascade Figure I-60 for potential use in future experiments. For use with this experiment, the cascade inlet had to be modified to include a cap to direct the flow coming from the enclosure where the specimen is fractured, thus producing an asymmetric flow and particle distribution in the upper three stages of the cascade that was undesirable, as shown in Figure I-61. Therefore, work on the Marple cascade was discontinued.

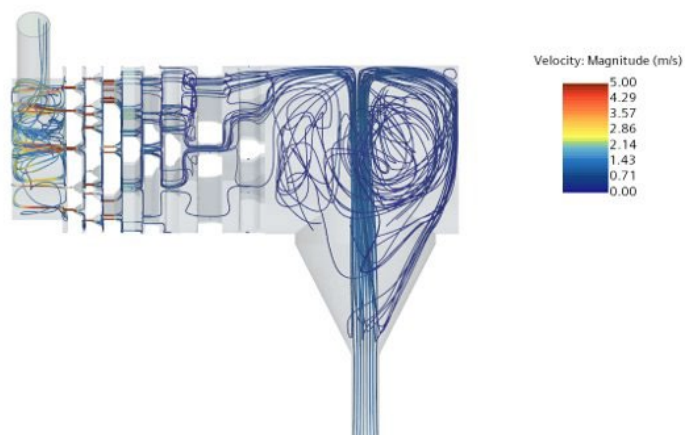


**Figure I-61. CFD simulation of a Marple cascade with an inlet cap producing an asymmetric flow distribution in the top 3 stages.**

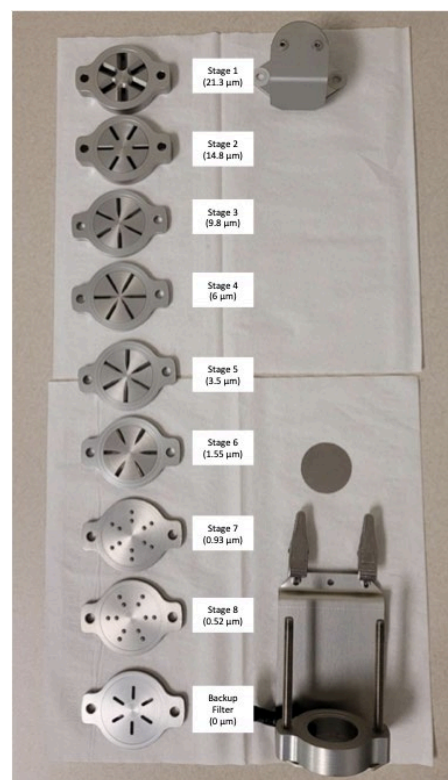


**Figure I-60. Disassembled Marple impactor with respective cut-off values for each stage.**

## I-7.2 Optional dual sampling

The SNF aerosol particles collected in the first experiment were sent directly for chemical processing without being characterized under an SEM to ensure radiological worker safety, because the room's enclosure had a gap at the ceiling. Additionally, the team had concerns that some portion of the collected material could be resuspended and lost during vacuum pump-down in the SEM. To mitigate these risks while still providing for SEM imaging of the specimens from at least one test, a dual sampling setup is being developed. As mentioned previously, it is very important to image the collected materials from at least one test to provide further verification of the stage cutoffs and to look for material agglomerates. As illustrated in Figure I-62, the dual sampling option allows for co-collection of samples from a test using two separate modified Sioustas cascade impactors with one set of stages analyzed using ICP-MS and the other set of stages allocated to SEM analysis. Ideally, each cascade would receive half of the aerosol inventory for collection.

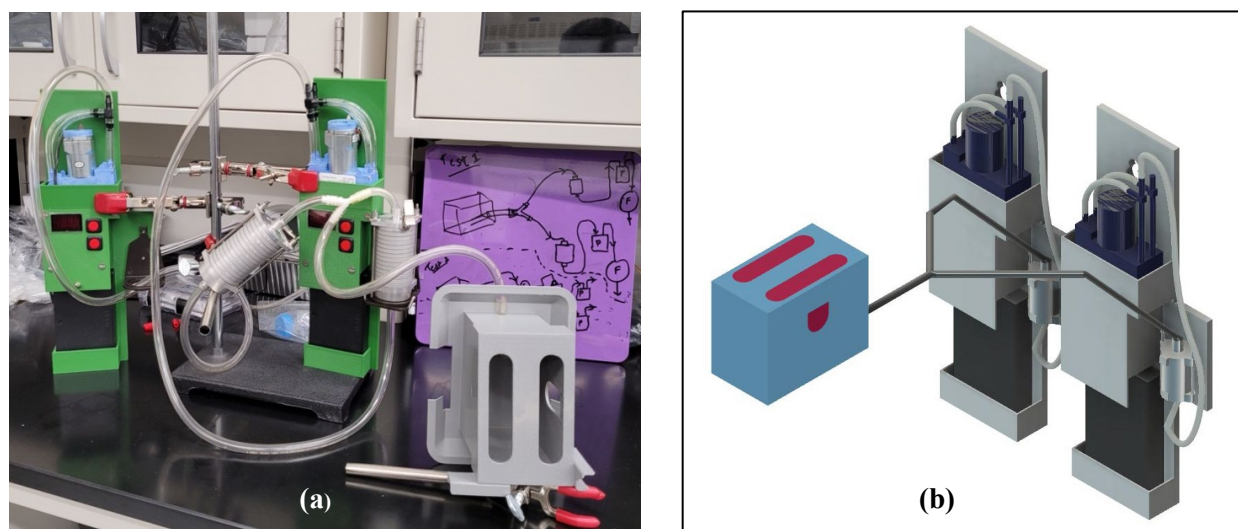


**Figure I-62. Combined collection set up (a), and schematic of the combined collection setup (b).**

To ensure that each cascade received the correct flow in this dual configuration, two tests were performed as illustrated in Figure I-63. The flow rates were measured at 5 s intervals, and the values thus obtained are listed in Table I-29.

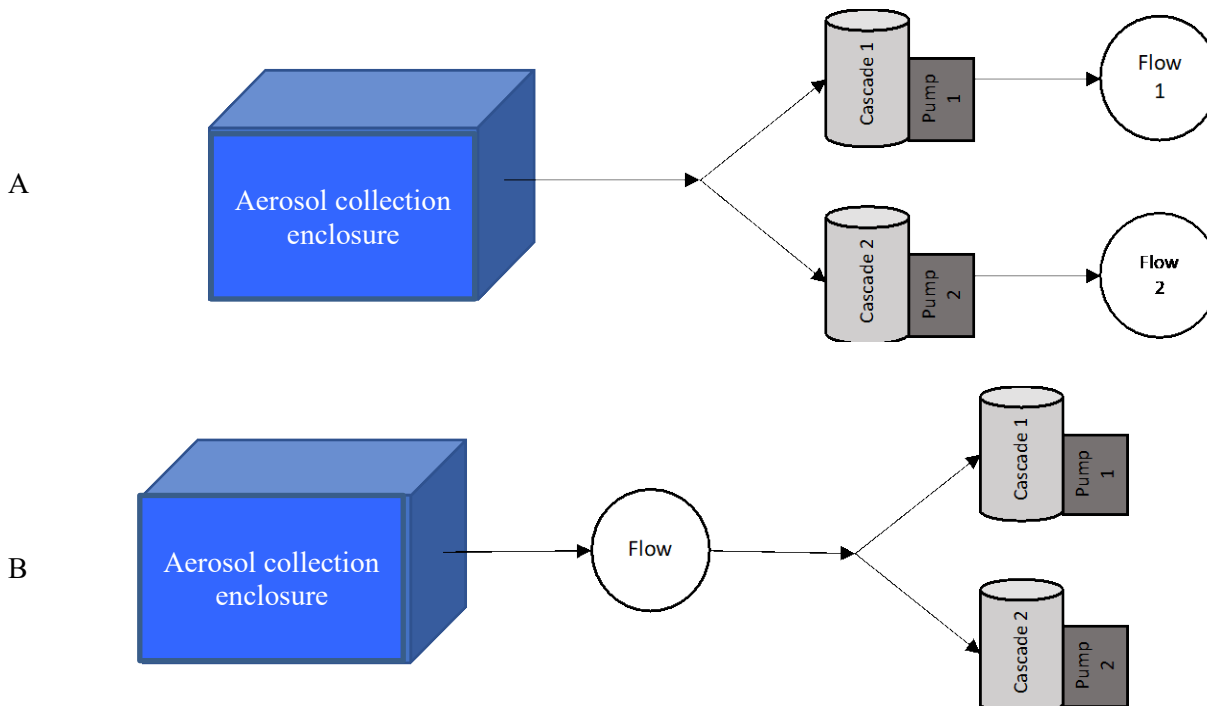


**Figure I-63. Individual flow rate measurements for the dual sampling setup: (A) pump exit, and (B) enclosure exit.**

**Table I-29. Respective flow rate values of cascades 1 and 2 under combined collection setup.**

Flow measurement configuration A				Flow measurement configuration B		
S. No.	Time (sec)	Flow (rate) 1 (LPM)	Flow (rate) 2 (LPM)	S. No.	Time (sec)	Flow rate (LPM)
1.	5	7.27	7.4	1.	5	12.20
2.	10	7.32	7.38	2.	10	12.16
3.	15	7.26	7.35	3.	15	12.00
4.	20	7.30	7.33	4.	20	12.00
5.	25	7.29	7.29	5.	25	11.94
Average		7.28	7.35	Average		12.06

Although the individual pumps are drawing close to 7 LPM, the combined flow rate is reduced to about 12 LPM. This is understood to be an issue with the discharging battery that runs the pumps. Hence, another modification was made to the aerosol collection design by adding an AC-to-DC adapter to ensure a stable power supply to the pumps. The flowrates were again measured in parallel (Figure I-63A) and were observed to be stable at 7 LPM for long periods. Enclosure exit flow rate measurements (Figure I-63B) have not yet been completed, but they are expected to be stable at 14 LPM.

CFD simulations using STAR-CCM+ were run to examine the expected particle distribution into the two samplers for dual sampling configuration. The CFD domain is shown below in Figure I-64.

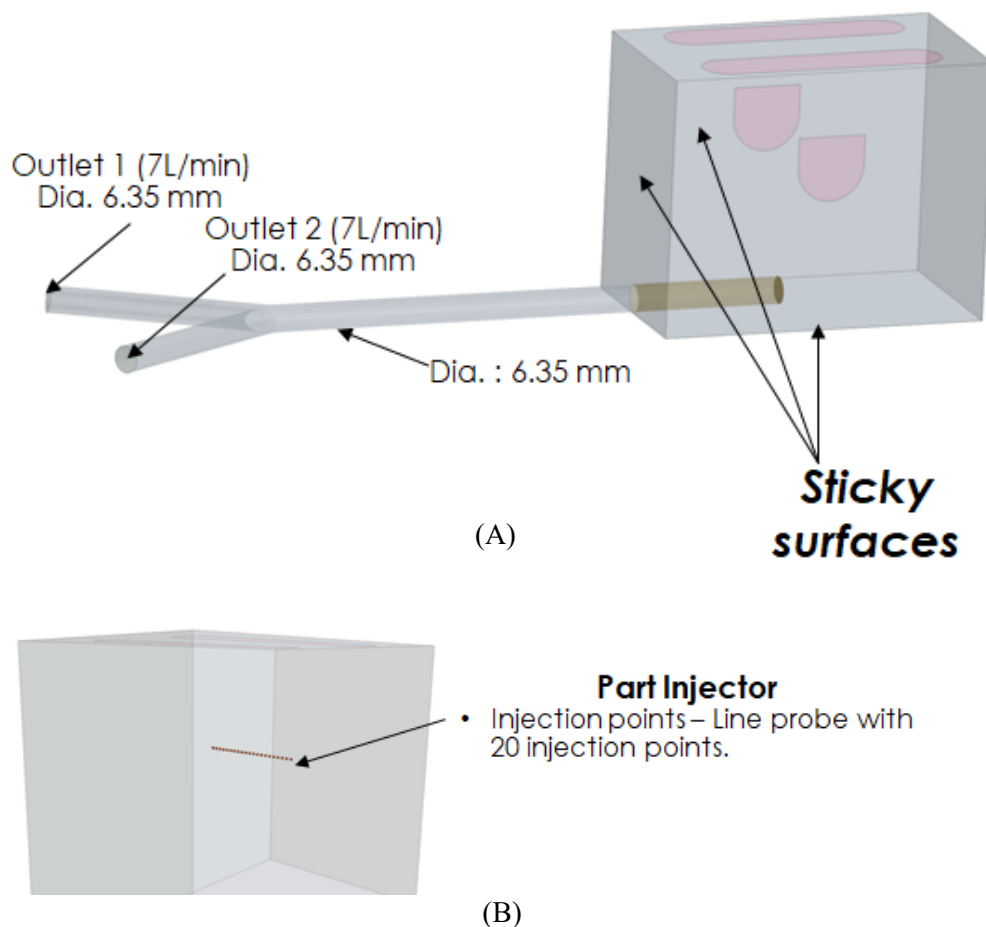


**Figure I-64. Details of the computational flow domain: (A) complete domain, including the stagnation pressure inlets (pink-colored surfaces), the box sticky surfaces, and the two outlets; and (B) part injector from where the particles are released at time  $t = 3$  seconds.**

The CFD flow domain shown above consists of stagnation pressure inlets, sticky surfaces upon which the particles are assumed to stick to the wall surface for all six wall surfaces of the box, and two outlets to the individual cascade samplers with pumps. The diameters of the main pipe and the two individual pipes, which are connected using a Y-connector, are all assumed to be 0.25 in. (6.75 mm). The flow through the two tubes is driven by two separate pumps (see Figure I-63). Similar to the cascade sampler simulations (Section I-6.2), the flow solver is first solved for 3 s with a timestep of 0.01 s, and then it is frozen for the remainder of the simulation. The flow-driven assumption was tested using the two-way coupled solver between the flow solver and Lagrangian-based particle solver, and negligible differences were obtained between the frozen flow solver approach and the two-way coupled approach. Using the background flow simulation, the particles were then released from the injector at  $t = 3$  s. The injection time is assumed to last for two seconds (i.e., from  $t = 3$  s to  $t = 5$  s) and the simulation was then run for an additional 5 s.

before stopping. The injector releases simulated solid  $\text{UO}_2$  particles ( $\rho = 10.97 \text{ g/cm}^3$ ) with a log normal (physical) size distribution in the range of  $[0.1, 50] \mu\text{m}$  with a mean  $= 15 \mu\text{m}$ . Additionally, the particle parcels released from the injector are assumed to have a velocity that is randomly sampled from a normal distribution in the range of  $[-10, 10] \text{ m/s}$  with a mean of  $0.0 \text{ m/s}$  and a standard deviation of  $5 \text{ m/s}$ . This assumption is grounded in the fact that the rod fracture is expected to release high velocity particles in all directions; in the absence of any particle velocity measurements, a normal distribution is thought to be a good approximation. The total injected particle (physical) size distribution is provided in Figure I-65.

The particle (physical) size distribution is tracked at the two outlets from injection until the simulation is stopped and the final particle distribution at outlet 1 and outlet 2 are shown in Figure I-66. Two important observations can be made regarding the distributions: (1) for both the samplers, the large diameter particles remain in the enclosure and do not pass through the tubing to the samplers as shown in Figure I-67, and (2) the particle distribution to the two outlets is asymmetric. One remedy that has been suggested to eliminate the asymmetry is to use larger tubing at the enclosure exit.

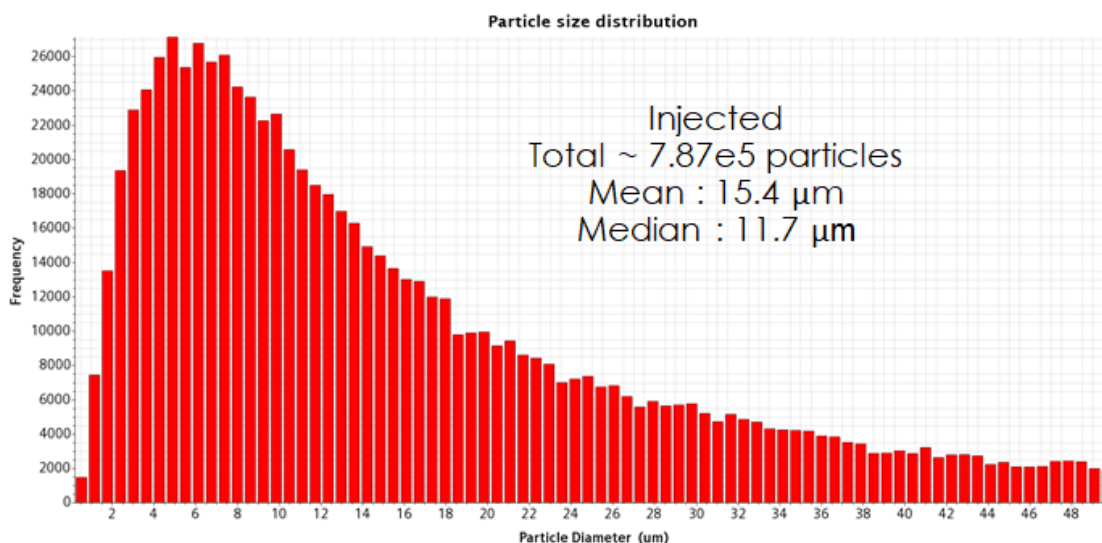


**Figure I-65. Particle size (Physical) distribution which is injected into the domain from  $t = 3\text{s}$  to  $t = 5\text{s}$ .**

Preliminary simulations are inconclusive as to the effectiveness of this approach, and more investigation is required to improve the y-connector design to ensure near symmetrical particle distributions to the two samplers/outlets.

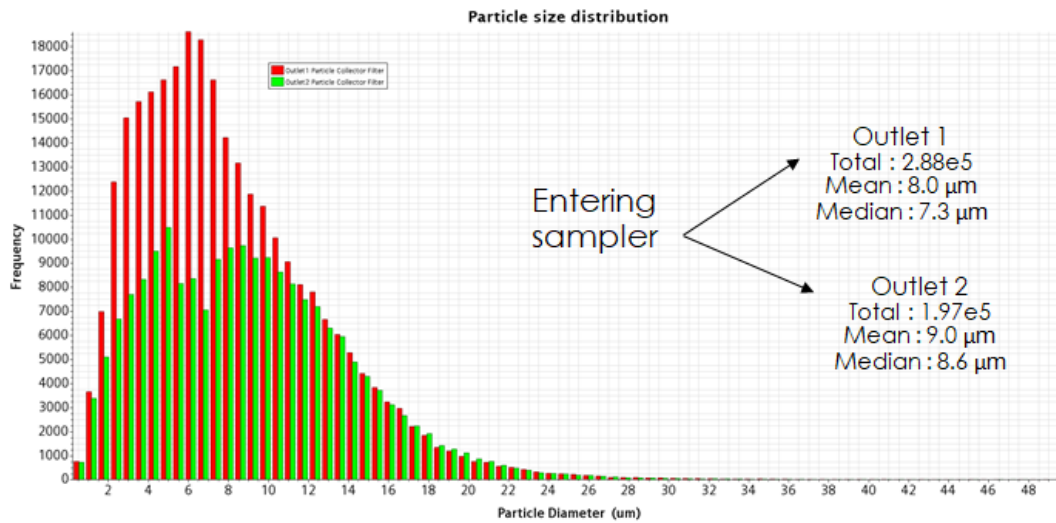


Figure I-66. Particle size (physical) distribution which is injected into the domain from  $t = 3$  s to  $t = 5$  s.

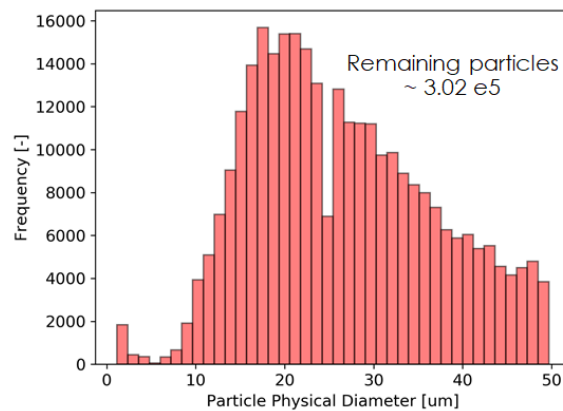


Figure I-67. Particle size (physical) distribution which does not pass through the samplers and is stuck in the box and the pipe walls from  $t = 3$  s to  $t = 10$  s.



## References

- [I-1] *High Burnup Dry Storage Cask Research and Development Project: Final Test Plan*, contract no. DG-NG-0000593, Electric Power Research Institute, Palo Alto, California (2014).
- [I-2] Saltzstein, S., et al., *Visualization of the High Burnup Spent Fuel Rod Phase I Test Plan*, SAND2018-8042-O (2018).
- [I-3] Scaglione, J. M., Montgomery, R. A., and Bevard, B. B., *Post-Irradiation Examination Plan for High Burnup Demonstration Project Sister Rods*, SFWD-SFWST-2017-000090 ORNL/SR-2016/708, Oak Ridge National Laboratory, 2016.
- [I-4] NUREG-2125, *Spent Fuel Transportation Risk Assessment, Final Report*, 2014, pp. E21-22.
- [I-5] Sioutas, C., *Development of New Generation Personal Monitors for Fine Particulate Matter (PM) and Its Metal Content*, NUATRC Research Report 2 (2004).
- [I-6] Marple, V. A., and Willeke, K., Impactor Design. *Atmos. Environ.* 10, 891–896 (1976).
- [I-7] SIEMENS, *STAR-CCM+ Simcenter Documentation 2021.1* (2021).
- [I-8] Hinds, W. C., *Aerosol Technology: Properties, Behavior, and Measurement of Airborne Particles*. Wiley (1982).
- [I-9] United States Patent US006786105B1, Personal Particle Monitor (2002).
- [I-10] Moore, M. E., and Tao, Y., *Aerosol Physics Considerations for Using Cerium Oxide CeO<sub>2</sub> as a Surrogate for Plutonium Oxide PuO<sub>2</sub> in Airborne Release Fraction Measurements for Storage Container Investigations*. Los Alamos National Laboratory (2017).
- [I-11] Hinds, W. *Aerosol Technology Properties, Behavior, and Measurement of Airborne Particles Second Edition*, Wiley (2012).
- [I-12] Aerosol Science and Technology – Parker C. Reist, McGraw-Hill, 1811,  
[https://books.google.com/books/about/Aerosol\\_Science\\_and\\_Technology.html?id=ZEcvAQAAIAAJ](https://books.google.com/books/about/Aerosol_Science_and_Technology.html?id=ZEcvAQAAIAAJ).
- [I-13] Mathworks MATLAB Image Processing Toolbox
- [I-14] Bansal, S. and Maini, R., A Comparative Analysis of Iterative and Ostu’s Thresholding Techniques. *Int. J. Comput. Appl.* 66, 975–8887 (2013).
- [I-15] Singh, T. R., Roy, S., Singh, O. I., Sinam, T. and Singh, K. M., “A New Local Adaptive Thresholding Technique in Binarization,” *IJSCI* (2012).
- [I-16] Find edges in intensity image - MATLAB edge.  
<https://www.mathworks.com/help/images/ref/edge.html>.
- [I-17] Morphological reconstruction - MATLAB imreconstruct.  
[https://www.mathworks.com/help/images/ref/imreconstruct.html?searchHighlight=imreconstruct&s\\_tid=srchtitle](https://www.mathworks.com/help/images/ref/imreconstruct.html?searchHighlight=imreconstruct&s_tid=srchtitle).
- [I-18] Marker-Controlled Watershed Segmentation - MATLAB & Simulink Example.  
<https://www.mathworks.com/help/images/marker-controlled-watershed-segmentation.html>.
- [I-19] Arganda-Carreras, I., et al., “Trainable Weka Segmentation: A Machine Learning Tool for Microscopy Pixel Classification.” *Bioinformatics* 33, 2424–2426 (2017).
- [I-20] SIEMENS, STAR-CCM+ Simcenter Documentation (2021).



- [I-21] Di Lemma, F. G., Colle, J. Y., Rasmussen, G., and Konings, R. J. M., “Fission Product Partitioning in Aerosol Release from Simulated Spent Nuclear Fuel.” *J. Nucl. Mater.* 465, 127–134 (2015).
- [I-22] Clark, R. A., et al., “Distribution of Metallic Fission-Product Particles in the Cladding Liner of Spent Nuclear Fuel.” *NPJ Mater. Degrad.* 4, 4 (2020).
- [I-23] Montgomery, R. A., et al., *Sister Rod Nondestructive Examination Final Report*, SFWD-SFWST-2017-000003 Rev. 1 (M2SF-17OR010201021) / ORNL/SPR-2017/484 Rev. 1 (ORNL/SPR-2018/801), Oak Ridge National Laboratory, 2019.